A STUDY ON STRAIGHTNESS CONTROL IN DEEP HOLE DRILLING OF INCONEL-718

AKSHAY CHAUDHARI

NATIONAL UNIVERSITY OF SINGAPORE

2016

A STUDY ON STRAIGHTNESS CONTROL IN DEEP HOLE DRILLING OF INCONEL-718

AKSHAY CHAUDHARI

(B.Tech. Mechanical Engineering)

A THESIS SUBMITTED
FOR THE DEGREE OF DOCTOR OF PHILOSOPHY
DEPARTMENT OF MECHANICAL ENGINEERING
NATIONAL UNIVERSITY OF SINGAPORE

2016

DECLARATION

I hereby declare that the thesis is my original work and it has been written by me in its entirety. I have duly acknowledged all the sources of information which have been used in the thesis.

This thesis has also not been submitted for any degree in any university previously

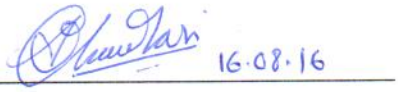

16.08.16

Akshay Chaudhari

ACKNOWLEDGEMENTS

This thesis work is a culmination of hard work and dedication; it would not have been possible without the support of wonderful people around me.

I am very grateful to my supervisors Asso. Prof. A. Senthil Kumar and Prof. M. Rahman for giving me the opportunity to pursue my passion in the field of manufacturing. Their guidance, encouragement, and constant support not only helped me academically but also in my personal life.

I would like to thank Dr. Woon Keng Soon from Singapore Institute of Manufacturing Technology (SIMTech) for his help and guidance in the research work. I am indebted to Mr. Tnay Guan Leong from SIMTech for his help in conducting the experiments. Without him, it would have been a difficult journey. I would like to extend my gratitude to all members of Advanced Manufacturing Laboratory at the National University of Singapore for their timely help and motivation.

I would like to thank my officemates Dr. Neo Wee Keong, Dr. Aravind, Dr. Nguyen Minh Dang, Dr. Afzal Ahmed, Huang Rui, Malarvizhi Sankaranarayanasamy, Lew Maan Tarng for their encouragement and support. I would like to thank Lalitendu Tripathy, Ujjaval Gupta, Vishal Wagholikar, Sumit Goyal, Dipika Berry, Swati Goyal, Mayura Patil and Saurabh Gaidhani for making PhD journey enjoyable.

Finally, I would like to thank my parents Mr. Devidas Chaudhari and Mrs. Pratibha Chaudhari, who inspire me to be a better person every day. I am also grateful to my sister Mrs. Shardul Patil for her support. I would like to

express my sincere gratitude towards all my teachers without whom I would not have reached this stage. Especially, I would like to thank Prof. P.K. Mishra from Indian Institute of Technology Bhubaneswar for encouraging me to pursue a career in research.

TABLE OF CONTENTS

SUMMARY

The deep hole drilling process using single-lip drill is incapacitated by the rapid tool wear, frequent tool breakages, and straightness deviation when employed to machine high aspect ratio hole in Inconel-718 required for oil-field equipment. Tool breakage or excessive hole straightness deviation (exceeding 1 mm per 1 m) lead to expensive reworking or scrapping of the workpiece. The major causes for excessive straightness deviation and tool breakage are improper machine setting parameters, excessive drilling thrust forces, and chip clogging. Although, an optimization of the machine setting parameters and drilling thrust forces is needed; it is expensive and time consuming if conducted experimentally.

In this thesis, a comprehensive predictive approach for straightness deviation is proposed. The three major components of the predictive framework are the predictive modelling of the single-lip drilling forces, quantification of the effect of chip morphologies on the drilling thrust force and the predictive straightness deviation modelling considering the effect of machine set-up parameters.

Initially, a benchmarking study on the single-lip drill engagement was conducted to identify and avoid the causes of cutting edge chipping in the single-lip drill engagement. Hence, a new parameter, 'Drilling Engagement Ratio' was introduced to quantify the effect of instability on the drill edge chipping. The benchmarking study also provided the guidelines for the further experiments.

Secondly, a detail predictive model for single-lip drilling forces was developed considering the effect of cutting edge radius. The model was also used to predict the distribution of the drilling forces along the cutting edges. The predicted results were found to be in good agreement with experimental results for a wide range of drill geometries and drilling parameters.

Thirdly, an experimental study to quantify the effect of chip morphologies on the drilling thrust force was conducted for a wide range of drill geometries and drilling parameters. The mechanism for chip formation and chip breaking were studied using novel high-speed photography set-up. Moreover, guidelines for selection of the drill geometry and the drilling parameters were provided to avoid chip clogging.

Finally, a predictive hole straightness deviation model considering the effect of misalignments at multiple supports, varying support distances and thrust force was developed and experimentally validated. The predicted and the experimental hole straightness deviations were found to be in good agreement. Based on the analysis conducted using proposed model, a novel movable bearing housing was developed and tested successfully for the straightness control. The predictive framework for straightness deviation not only predicted the deviation with reasonable accuracy but also successfully used for the straightness control to achieve deviation within the limit of 1 mm per 1 m.

LIST OF SYMBOLS

A	Yield stress of the material in J-C material model
α_e	Effective rake angle
α	Rake angle
B	Strain hardening modulus in J-C material model
β	Portion of the heat conducted to the workpiece from primary shear zone
C	Strain rate constant
C_o	Oxley's strain rate constant
C_p	Specific heat capacity of workpiece material
c_p	Distance of drill apex point from drill center
ψ	The temperature factor for tool-chip interface
D	Diameter of the drill
dw	Elemental width of the cut
dw_i	Elemental width of the cut at inner cutting edge
dw_o	Elemental width of the cut at outer cutting edge
dF_c	Total elemental cutting force
dF_t	Total elemental thrust force
dF_s	Elemental shear force

dF_f	Elemental frictional force at tool-chip interface
$(dF_c)_s$	Elemental cutting force due to shearing
$(dF_t)_s$	Elemental thrust force due to shearing
$(dF_c)_p$	Elemental ploughing force in cutting direction
$(dF_t)_p$	Elemental ploughing force in feed direction
dN_c	Elemental normal force at tool-chip interface
dR_c	Resultant force at tool-chip interface and at shear plane-AB
d_c	Diameter of the spiral chip
d_{c-max}	Maximum chip diameter which can fit in V-flute
δ	Ratio of tool‑chip interface plastic zone thickness to chip thickness
δ_1	Misalignment at the first support w.r.t. spindle axis
δ_2	Misalignment at the second support w.r.t. spindle axis
δ_3	Misalignment at the fix chip-box support w.r.t. spindle axis
δ_b	Misalignment at the pilot bush w.r.t. spindle axis
E_d	Young's modulus of the drill shaft material
e_k	Drill tip deviation after k^{th} cycle
$\dot{\varepsilon}$	Equivalent strain-rate in J-C material model

$\dot{\varepsilon_o}$	Reference strain-rate in J-C material model
$\dot{\varepsilon_{AB}}$	Equivalent shear strain rate at primary shear zone
ε_{int}	Equivalent shear strain rate at tool-chip interface
ε_{max}	Tensile strain on the free side of the chip
ε_{crit}	Critical strain for chip breaking
$\Delta\varepsilon_{chip}$	Change in strain due to increase in chip up-curl radius
F_{xt}, F_{yt}, F_{zt}	Drilling forces in drill coordinate system
F_X, F_Y, F_Z	Drilling forces in fixed coordinate system
ΔF_{zc}	Increase in thrust force due to chip clogging
f	Feed rate per revolution
γ_{AB}	Shear strain at primary shear zone
$\dot{\gamma}_{AB}$	Shear strain-rate at primary shear zone
$\dot{\gamma}_{int}$	Strain rate at tool-chip interface
h	Tool-chip contact length
I_d	Second area moment of drill shaft cross section area
K	Heat conductivity of workpiece material
k_{AB}	Flow strass at shearing plane-AB with von-Mises criterion

k_{chip}	Flow stress in chip
L	Length of the drill
L_e	Distance travelled by drill before complete engagement
l_1	Distance between the first support and the spindle
l_2	Distance between the second support and the spindle
l_{AB}	Length of primary shear zone
l_c	Length of the spiral chip
l_{cb}	Length of chip box and pilot bush combined
l_{eq}	Effective/usable length of drill
l_{sf}	Distance between the fixed support and the spindle
l_s	Length of the intermediate support base
λ	Friction angle in Oxley's machining theory
m	Thermal softening constant for J-C model
n	Strain Hardening constant in J-C model
n_{eq}	Modified strain hardening constants for J-C model
n_s	Number of intermediate supports
η	Percentage of total shear energy appearing as sensible heat

p_c	Pitch of the spiral chip
ρ	Density of the workpiece
ρ_n	Angle of prow for slip-line model
ϕ	Shear angle
ϕ_r	Angle of drill rotation
φ_i	Inner cutting edge angle
φ_o	Outer cutting edge angle
R	Radius of the drill
RPM	Revolutions per minutes
R_T	Non-dimensional thermal parameter
r_u	Chip up-curl
r_e	Cutting edge radius
r_{ei}	Edge radius on the inner cutting edge
r_{eo}	Edge radius on the outer cutting edge
Δs_1	Thickness of the parallel-sided primary shear zone
Δs_2	Thickness of the secondary shear zone
σ	Flow stress
σ_1	Strength constant used in power law material model

σ_{AB}	Flow stress at shearing plane-AB
σ_N	Normal stress at tool chip interface
T	Instantaneous temperature used in J-C model
T_{AB}	Average temperature of primary shear zone
T_m	Melting point temperature of work material
T_{int}	Average temperature at tool-chip interface
T_o	Workpiece temperature or room temperature
ΔT_{sz}	Average rise temperature in primary shear zone due to plastic work done
ΔT_M	Maximum temperature at tool-chip interface
t_c	Chip thickness
t_{ctr}	Chip thickness ratio
t_{ei}	Engagement time for Phase-I
t_e	Time required for complete engagement of drill
t_o	Uncut chip thickness
τ_{int}	Shear stress at tool-chip interface
θ_c	Angle of conical bottom pilot hole
θ_t	Angle of drill V-flute

μ_{w-t}	Tool-workpiece friction coefficient
V_c	Chip velocity
V_r	Cutting speed at any given drill radius r
V_s	Shear velocity
$\boldsymbol{v}$	Cutting velocity vector
$\boldsymbol{v_f}$	Feed velocity vector
$\boldsymbol{v_{cf}}$	Chip velocity with respect to drill flute
$\boldsymbol{v_{cf}}$	Chip velocity with respect to workpiece
ω	Angular speed of drill
XYZ	Fixed workpiece coordinate system
$x_s y_s z_s$	Spindle coordinate system
$x_t y_t z_t$	Drill coordinate system

LIST OF FIGURES

LIST OF TABLES

NOMENCLATURE

DHD	Deep Hole Drilling
DER	Drilling Engagement Ratio
J-C	Johnson and Cook material model
PSZ	Primary Shear Deformation Zone
SLD	Single-lip Drill
SSZ	Secondary Shear Deformation zone

Chapter 1: Introduction

1.1 Background

One of the most common subtractive manufacturing processes used for hole making is drilling. However, when the length to diameter ratio (also called aspect ratio, L/D) is more than 10, the holes are categorized as deep holes. The machining process employed to make these deep holes is called 'deep hole drilling' (DHD).

The deep holes are required in many applications such as aerospace, nuclear power, hydraulics and oil-field industries. These deep holes cannot be drilled using normal twist drills due to the problems of poor chip evacuation and inferior hole surface quality. Hence, an asymmetrical single-lip drill (SLD) is used to manufacture deep holes. The drill was invented during the American civil war to manufacture high aspect ratio holes for gun barrels. Hence, the drill is also called 'gundrill' and the drilling process is called 'gundrilling'.

The gundrilling process is then successfully developed and used in other industries over a century. The gundrilling process used as a DHD method is capable of drilling precise and large aspect ratio holes. It yields excellent result while drilling conventional materials such as steels, cast iron, aluminium etc. However, some of the new difficult-to-machine materials such as Nickel-Chromium alloys used in oil-field and aerospace industries call for a fresh look into the DHD processes.

1.2 Motivation

Nickel-Chromium alloys are heavily used in oil-field industries for drill collar used for oil-well downhole assembly. In addition, these are also used in the aircraft industry for engine components where 50% jet engine weight is attributed to Inconel 718 which is a Ni-Cr alloy [1]. In the oil-field industries, new developments such as 'measurement while drilling (MWD)' and 'logging while drilling (LWD)' require drill collars that can sustain high temperature, corrosive environment, and high mechanical loading with non-magnetic properties. Nickel based alloys such as K-Monel, Inconel, waspaloy are the best suited options for these applications [2]. These alloys are also called superalloys because their excellent high hot hardness, corrosion resistance, and high yield strength. One of the key requirements for the oil-field Inconel-718 drill collar is the deep holes on the circumference to ensure a passage for data transmission cables from the MWD and LWD sensors as shown in Figure 1.1. Usually, these holes are 8 mm in diameter and 1 to 5 m in length (Aspect ratio : L/D ~125 to 625).

Figure 1.1 Drill collar with high aspect ratio hole [3]

However, the deep hole drilling in Inconel-718 is incapacitated by three major problems –

1. Excessive tool wear
2. Tool breakage due to chip clogging
3. Hole straightness deviation

The Inconel-718 is an expensive material moreover the deep hole drilling process is costly as well due to the higher tooling cost and low productivity because of difficult-to-machine properties of Inconel-718. Straightness deviation 1 mm per 1 m or tool breakage inside the hole may result in discarding or reworking of the expensive Inconel-718 workpiece. In addition, it is economically not feasible to test all the parameters experimentally for the optimization of deep hole drilling process as it is affected by many parameters. Hence, a predictive framework for straightness control is needed.

1.3 Research Scope

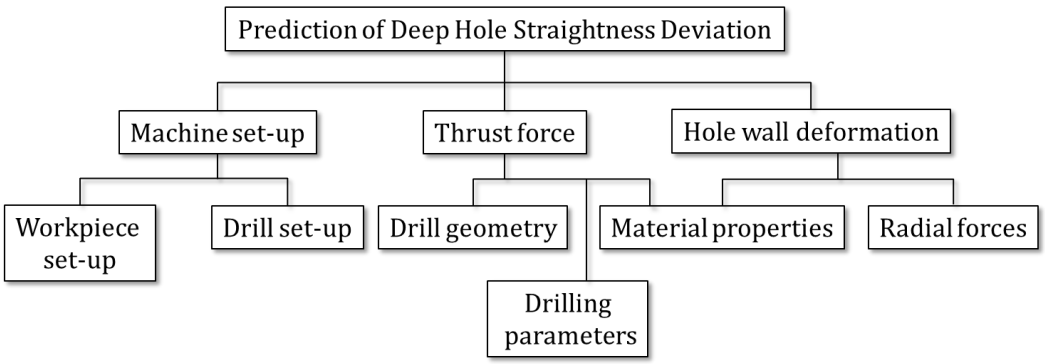

Figure 1.2 Predictive framework for hole straightness deviation

The hole straightness is mainly affected by machine set-up, thrust force, and the hole wall deformation as shown in Figure 1.2. The deep hole drilling

process in Inconel-718 is generally carried out at very low feed rates to avoid straightness deviation. However, at lower feed rates the micro-geometry features of the cutting edges such cutting edge radius influence the cutting drilling forces due to the size effect [4]. Hence, the effect of cutting edge radius must be considered while predicting the drilling forces. Moreover, the chip morphologies have a significant effect on the drilling thrust force which needs to be quantified for deep hole drilling of Inconel-718.

In addition, the hole straightness in deep hole drilling is greatly influenced by the machine setting parameters. It is economically not feasible to quantify the effects of multiple machine setting parameters on the hole straightness experimentally. Hence, a predictive analytical approach is needed to model the effects of machine setting parameters in order to control the straightness deviation.

The main objective of this research is to develop a predictive framework for hole straightness control in deep hole drilling of Inconel-718. Based on this framework following objectives are set for the research,

- Development of a comprehensive predictive model for single-lip drill drilling forces considering the effect of edge radius.

- Quantification of the effects chip morphology on the thrust force, in addition to the study of chip breaking mechanism in deep hole drilling of Inconel-718.

- Development of a predictive model for the hole straightness deviation considering the effect of thrust force and other machine setting parameters.

- Development of a mechanism for straightness control using predictive framework for deep hole drilling.

1.4 Outline of the Thesis

This thesis is organized in six chapters as follows-

Chapter 2 reviews the literature related to deep hole drilling and Inconel-718 drilling. It also includes the review of studies related to modelling of the deep hole drilling process.

Chapter 3 describes the challenges related to pilot hole preparation and its effects on tool-work engagement, especially during initial penetration. A quantitative method is proposed to prevent tool chipping during the engagement, which also standardized the drilling methodology for the further studies.

Chapter 4 includes a predictive analytical model for drilling forces in the single-lip deep hole drilling. The model considers the effect of the tool edge radius on the ploughing forces and uses Johnson and Cook material model.

Chapter 5 presents the results of an experimental study on the effect of tool geometry and feed rate on chip morphology. The effects of chip morphologies on the drilling thrust forces were quantified in this chapter.

Chapter 6 presents a predictive model of hole straightness deviation for deep hole drilling process which considers the effects of various machine setting parameters such as support distances, support misalignments, and drill lengths. Moreover, development and testing of a novel straightness control mechanism is presented in this chapter.

Chapter 7 summarizes the major finding of the research and proposes possible future works.

Chapter 2: Literature Review

2.1 Introduction

The deep hole machining is used for machining hole with very high aspect ratios (usually>10). There are three deep hole drilling techniques which are mainly differentiated on the basis of coolant supply and mechanism of chip removal. The machining processes are,

1. BTA drilling
2. Ejector drilling
3. Gundrilling or Single-lip deep hole drilling

The BTA stands for 'Boring and Trepanning Association' drilling technique which is used for holes with a diameter more than 15mm. The ejector drilling technique can be used for holes with a diameter more than 12 mm, however, it cannot be used for materials which produce difficult to break chips as the pressure available to push chips is very limited. For small and precise holes, gundrilling is the most favorable method as it provides a wide range of diameters from 1.5mm to 40mm. In this research, the focus is concentrated on the gundrilling process with a diameter range of 6mm to 10mm.

In the following section, deep hole drilling machine set-up and drill geometry of the single-lip drill is explained.

2.2 Overview of Single-lip Deep Hole Drilling Process

2.2.1 Single-lip deep hole drilling machine

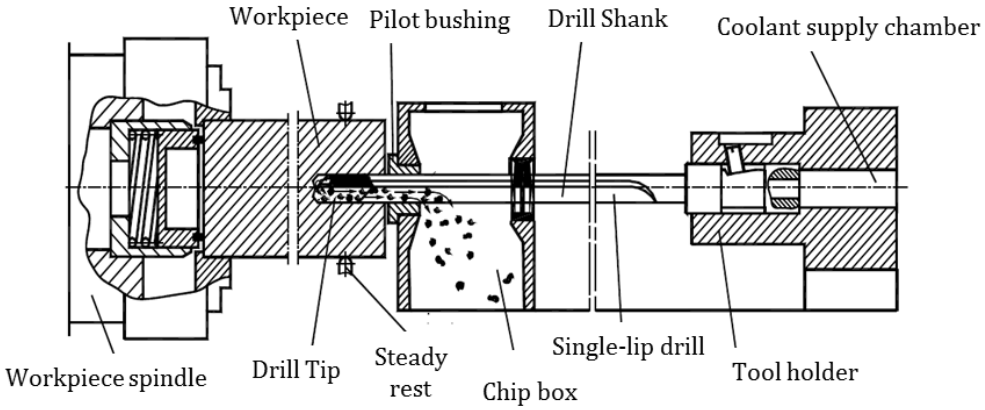

Figure 2.1 Single-lip deep hole drilling machine set-up [5]

In gundrilling, high-pressure coolant is supplied internally from spindle which passes through the shank and reaches the cutting region at the bottom of the hole. The high-pressure coolant dissipates the heat from cutting region and flushes out the chips through V-shape straight flute of the drill. The chips are collected in the chip box and the coolant is recirculated after filtering.

2.2.2 Basic single-lip drill geometry

The gundrill is also known as a single-lip drill (SLD), straight flute drill and self-piloting drill (SPD) because of its unique asymmetrical geometry. The gundrill has three main components 1.carbide tip 2.steel shank and 3. driver as shown in Figure 2.2. In general, the carbide tip is brazed on the steel shank and the length of the shank depends on the drilling depth. However, for smaller diameter gundrills, the entire shank can be made from carbide material to increase the stiffness of the drill. The carbide tip is ground to form inner

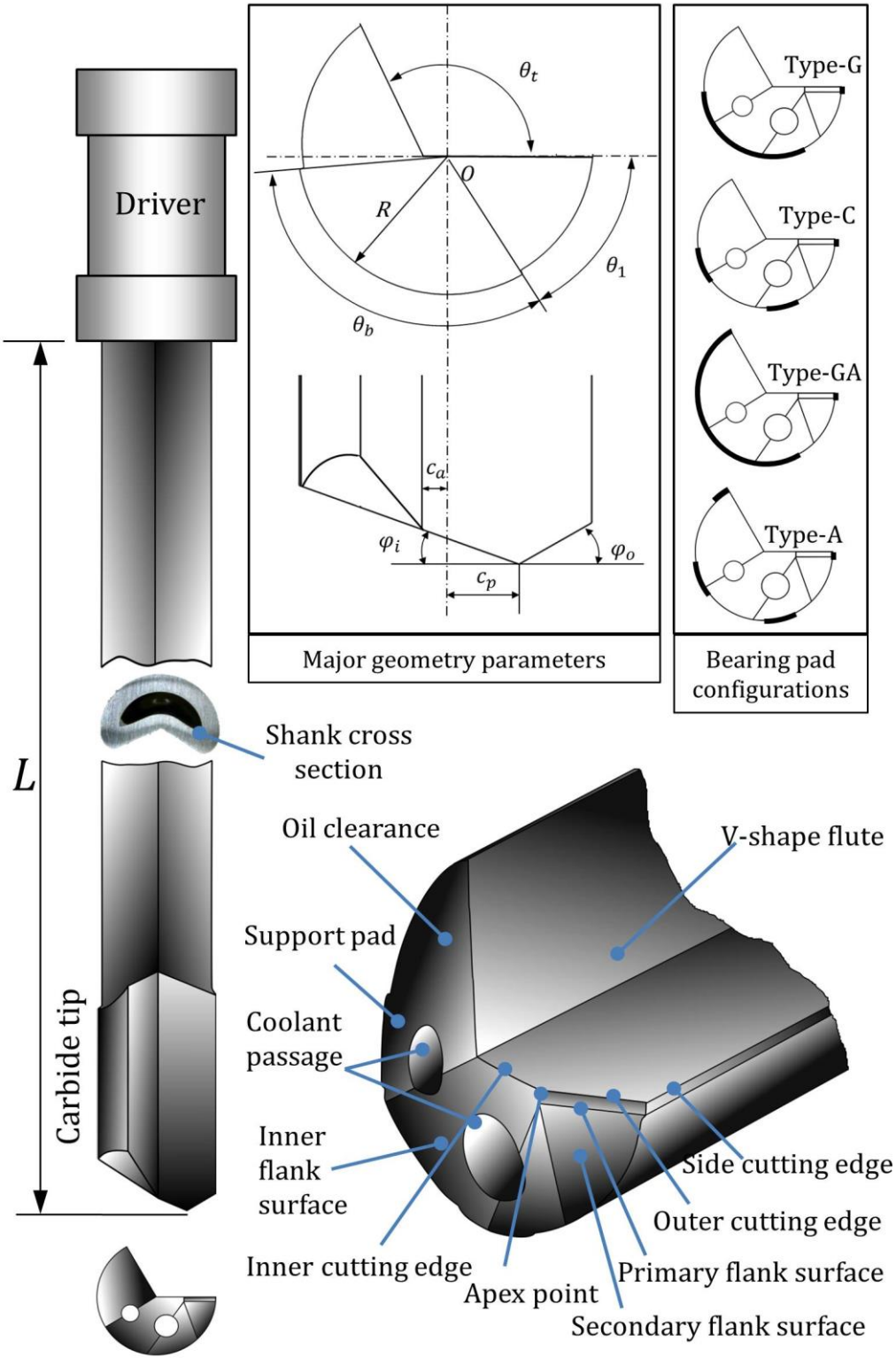

Figure 2.2 Geometry of single-lip drill

cutting edge and outer cutting edge with angles φ_i and φ_o respectively. The cutting edges meet at apex point and the distance of apex is measured from the center the drill as c_p. The other angles provided on the face of carbide tip ensure that, only the cutting edges are in contact with bottom surface of the hole. Unlike the twist drill, the forces in radial and tangential directions are not balanced, hence guide pads are provided on the cylindrical side of the carbide tip. The guide pads are also called bearing pads or support pads and depending on the workpiece material the location and the shape of the guide pad changes. The various bearing pad configurations are shown in Figure 2.2.

2.3 Literature on Deep Hole Gundrilling

The deep hole gundrilling literature can be divided into three major categories as,

- Gundrill force system and stability
- Chip control
- Hole accuracy and straightness.

2.3.1 Gundrill force system and stability

2.3.1.1 Self-piloting in gundrills

The self-piloting action of deep hole gun drills was explained by Sakuma et al.[6] where it was referred as ‘self-guiding action’. According to Astakov [5], the resultant of tangential and radial force is balanced by the supporting pads as shown in Figure 2.3, which provide additional machining operation known as burnishing. The term self-piloting means drill guides itself by

machining the bush due to burnishing. The burnishing action is possible as the bearing pads are located behind the cutting edges.

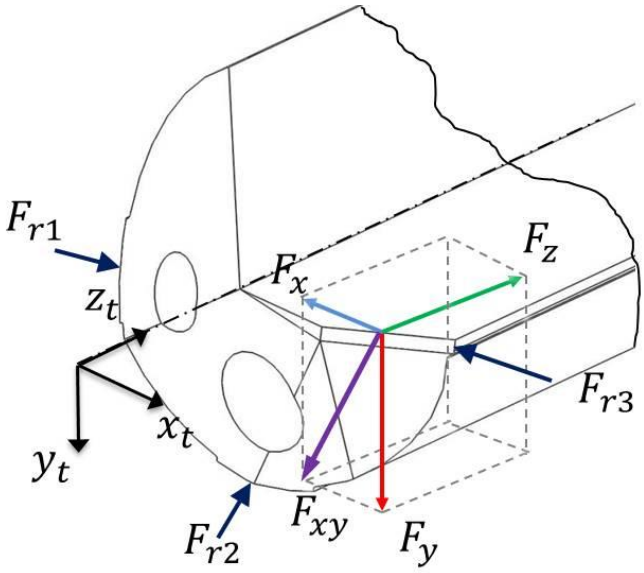

Figure 2.3 Self-piloting action

2.3.1.2 Force modelling in gundrilling

In the study conducted by Griffiths et al.[7], a force system consisting of 23 forces was developed for deep hole drilling tools as depicted in Figure 2.4. The forces were divided into four groups namely oil forces, cutting forces, burnishing forces and frictional forces. The relation between the forces was defined by coefficients which were determined by conducting series of experiments. In the second part of the study, power and energy requirement based on frictional and burnishing coefficient were studied [8].

Later, Astakhov et al.[9] analytically evaluated cutting forces in self-piloting drilling using shear zone model with parallel boundaries. The model satisfactory predicted the forces along the cutting edges. The calculated forces were then used for optimizing the pad location on the tool. They also pointed

out that there was no trend in error values for calculated forces and measured forces owing to inaccuracies in regrinding process [10].

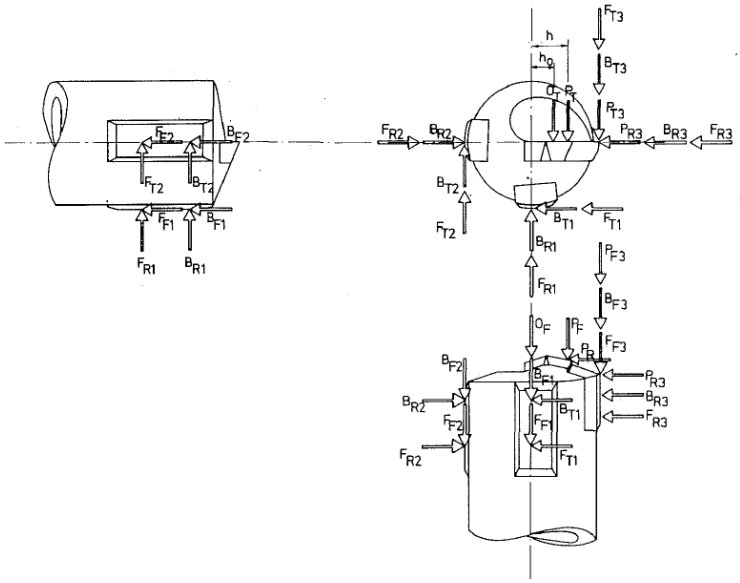

Figure 2.4 Gundrilling force system proposed by Griffiths et al.[7]

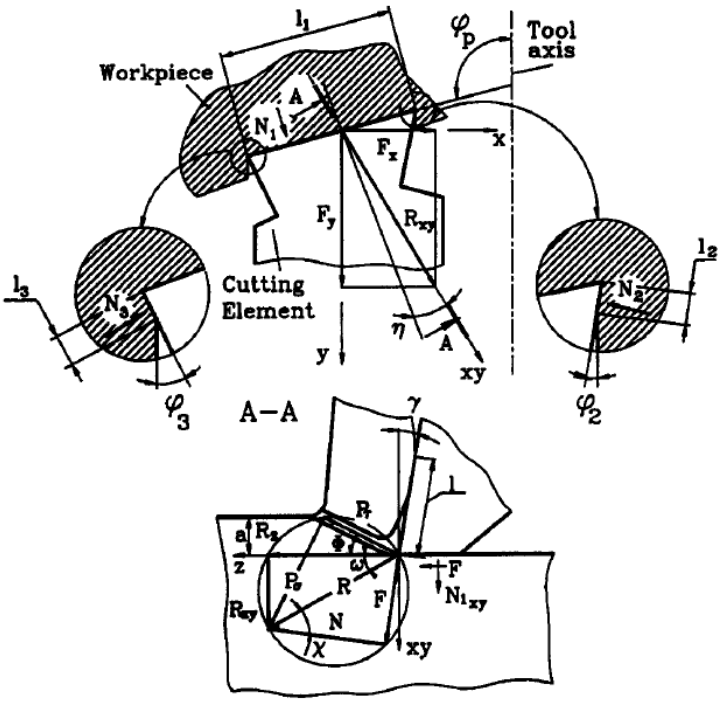

Figure 2.5 Force modelling of gundrilling using slip-line theory by Astakov et al.[9]

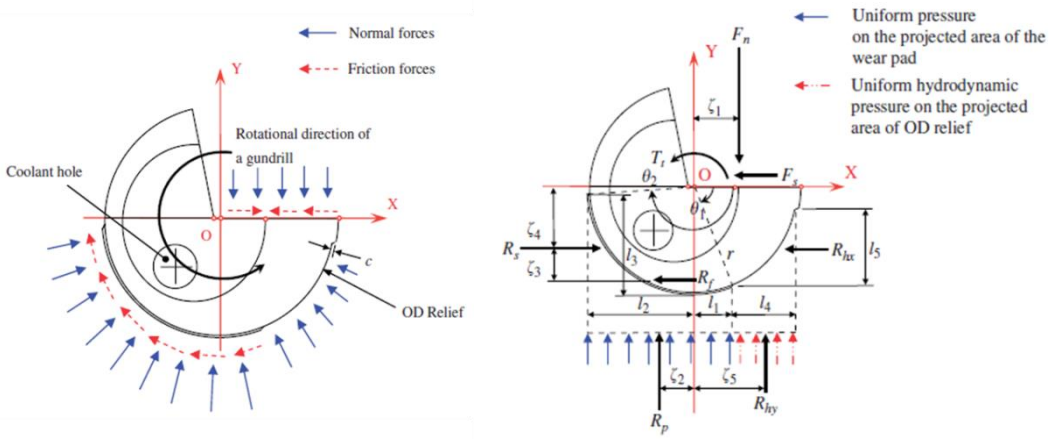

Figure 2.6 Gundrilling force system proposed by Jung et al.[11]

Jung et al.[11] proposed a gundrilling force model. The model not only considered cutting and frictional forces but also included hydrodynamic forces. Cutting forces were calculated using calibration method developed by Chandrasekharan et al.[12]. However, the predicted values of thrust force differ from the measured values by 39 to 59 %.The experimental torque values were found to be in better agreement with the predicted results as compare to force values.

Wang et al.[13] proposed a gundrill force system using specific cutting energy model and evaluated the performance of 'welded carbide gundrill' to cut AISI 1045 steel. An extensive set of experiments was carried out for cutting speed and feed rates. It was reported that the axial force increases with increasing feed rate and reduced cutting speed.

The previous models were developed and tested for conventional materials such as steels, aluminium etc. For these materials, feed rate, cutting speeds are very high and the uncut chip thickness is relatively very high as compare the cutting edge radius of the tool and cutting mechanics is mostly dominated by shearing action. But, for most of the difficult-to-machine materials such as

Inconel 718 conservative feed rates are used to reduce thrust force and drill straightness deviation. According to leading gun drill manufacturer [14-16], feed rates for drilling Inconel-718 are suppressed between 8.95 to 23.3 mm/min. Combining with low rotational speeds between 873 to 1650 rpm. As a result, the uncut chip thickness reduces to micron scale between 8.9 to 14.1 μm. Moreover, commercial gun drills cutting edge radii were found in the range of 6-9 μm which were measured by the author on the gun drills from four different manufacturers. It was clear that the uncut chip thickness to cutting edge radius ratio (t_o/r_e) becomes less than 1, hence the effect of cutting edge radius cannot be neglected and needs to be consider in force modeling for deep hole drilling in Inconel-718.

2.3.2 Chip control in deep hole drilling

The chip control in deep hole drilling has been studied by many researchers over the years. Chin et al. [17] proposed a computer simulation and experimental analysis for chip monitoring in single-lip deep hole drilling. It was reported that the chips flow can be simulated as slug flow for normal chips and for compact chips a new model was proposed. The focus of the study remained on the chip transport model rather than chip formation mechanics.

Astakov et al. [18] proposed a novel approach for single-lip deep hole drill based on the experimental analysis of coolant flow and its effectiveness on chip removal. It was observed that, for particular drill geometries a vacuum region was generated near bottom hole irrespective of coolant flow rate. The vacuum region reduced the chip breaking efficacy of the coolant and chips

were more likely to be long. Based on the analysis, a new drill design was proposed in which a dub-off angle value 0 was found to be effective.

Mellinger et al. [19] developed a mechanistic model for chip evacuation forces and predicted chip clogging based on the torque criteria for twist drills. Calibration tests were performed to determine the frictional coefficients for tool-chip and chip-work contact. The model was used for pecking cycle prediction and prevention of tool breakage. Later, the same model was extended to different drill flute geometries [20].

Potthast et al. [21] developed an ultrasonic piezoelectric actuator for deep hole drilling. The application of the developed apparatus was limited to 0.9 to 6 mm diameter holes for relatively shorter drills with stiff shanks. The similar concept was used by Heisel et al. for deep hole drilling in electrolytic copper ECu 57[22]. They reported improvement in surface roughness on the hole wall surface of 5 mm diameter hole. It is important to note that the drills used in these experiments were solid carbide shank or drills with stiffer shanks and high rigidity. The similar vibrations if applied to the long drill with steel shanks might yield different results due absorption of vibrational energy due to lower stiffness hence may not be useful for the drill which is 1 m or longer.

Some of the recent studies adopted a conventional approach to understand chip formation and breaking mechanics. Wang et al [23] conducted deep hole drilling studies on forged steel S48CS1V TiAlN-coated gun drills. It was reported that the chip surface becomes rougher as the tool wear increases and the chips become thicker with increasing bluntness of tool due to ploughing action.

Biermann et al. [24] used high-speed camera to monitor chip formation in deep hole drilling of Inconel 718 and 20MnCrMo7. They observed that Inconel-718 produced longer chips as compared to 20MnCrMo7 due to high tensile strength. However, these studies were conducted on with 2mm diameter drills. For bigger diameter holes the mechanism of chip formation might change. Klocke et al. [25] developed an innovative optical sensor for chip transport monitoring.

The chip control research in deep hole drilling mostly focuses on monitoring of the chip transport and evacuation for conventional materials. Therefore, there is a need to understand the mechanism of chip formation and chip breaking in deep hole drilling of Inconel-718 to develop better tools. Moreover, it is important to quantify the effect chip morphology on the thrust force which might lead to tool breakage.

2.3.3 Hole accuracy and straightness in deep hole drilling

The hole accuracy in deep hole drills is defined by diametrical accuracy and straightness of the hole. The straightness in deep hole drilling affected by various factors such as support location, support misalignments, pilot bushing misalignments, vibrations, wall deformation etc. In early attempts to model straightness in deep hole drilling, Sakuma et al.[6] considered the effect of the pilot bushing and intermediate support misalignment on straightness profile. However, the effect of axial force was completely ignored and the deflection profile was predicted by considering only geometrical parameters. Katauki et al.[26] studied the influence of workpiece geometry on the axial hole deviation in deep-hole drilling. They also conducted theoretical and experimental

analysis and suggested that tool geometry imbalanced the cutting forces and caused hole deviations. Further studies conducted by Katsuki et al. [27] were focused on the effect of workpiece geometry on hole straightness deviation. The results for the effect of the inclined workpiece on straightness are shown in Figure 2.7. These studies revealed that hole deviation was affected by hole wall thickness and rose aggressively after reaching a certain value.

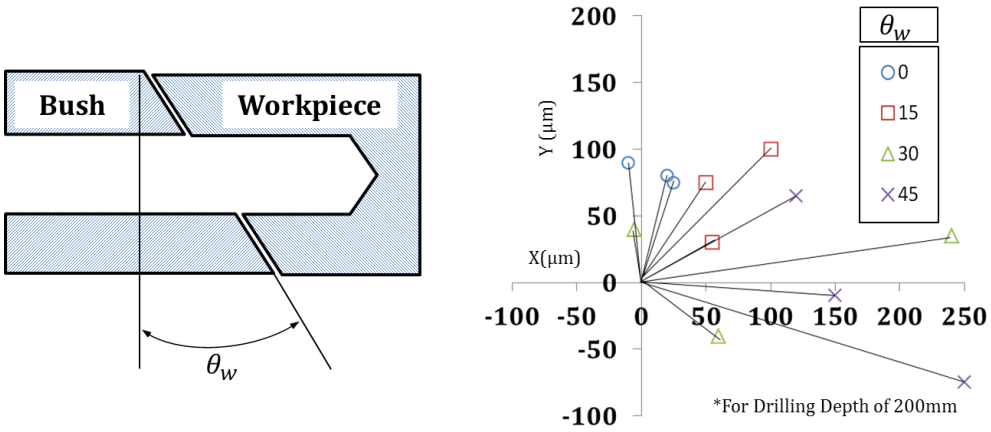

Figure 2.7 Effect of workpiece geometry on hole straightness studied by Katsuki et al. [27]

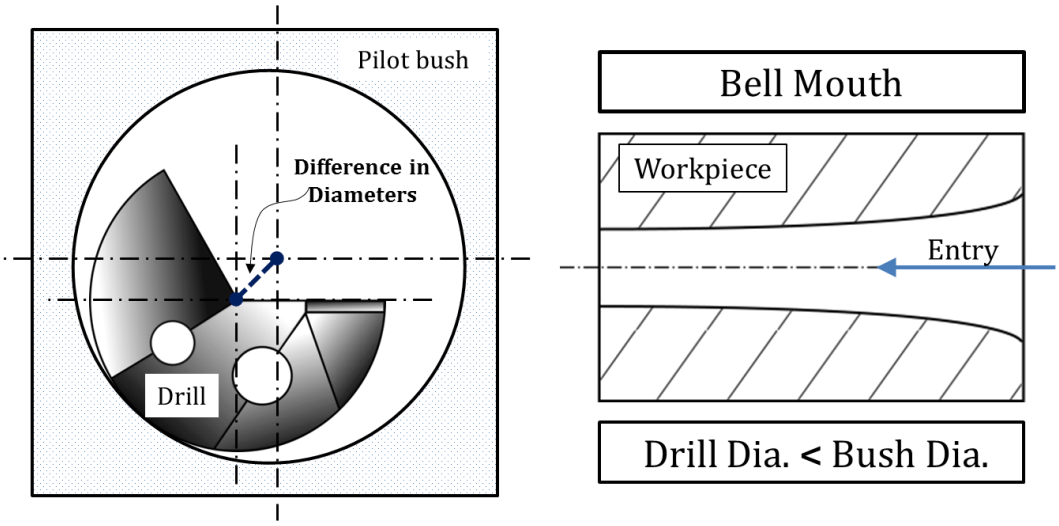

Figure 2.8 Bell mouth formation in deep hole drilling due to large clearance at pilot bush

Astakov [28, 29] studied the effect of pilot bush clearance on bell mouth formation. He concluded that the higher clearance at pilot bush may lead to premature failure of drill moreover, it may also lead to widening of the hole entry diameter as shown in Figure 2.8 (also called bell mouth formation). It was recommended to use dual supporting pads for automotive applications and the supporting pads' locations were optimized based on the force balance.

Al-Ata et al. [30] also studied the bell mouth formation for three working conditions rotating work-stationary tool, stationary work- rotating tool, and counter rotation . However, they could not conclude the study with any definitive recommendation due contradictory observations.

Deng et al. [31] studied the effect of support misalignment on hole straightness deviation based on Euler's beam theory. The model considered the effect of axial thrust force which was neglected by Sakuma et al. [6]. Straightness deviation profile was obtained using iterative process and verified against a large set of experiment. However, the experiments were limited to the drilling depth of 200 mm and the obtained hole straightness profile was linear. Chin et al. [32] compared the straightness deviation model by Deng et al.[31] with finite element model and found that the finite element model performs better in the absence of pilot bush misalignment.

The hole straightness deviation literature is limited to the effect single intermediate support however in practice, multiple supports are being used for deep hole drilling. Hence, a new straightness deviation model is required which considers the effect of misalignments at multiple supports and varying distances between supports during the drilling process.

2.4 Drilling in Inconel-718

Inconel-718 is a Ni-Cr based superalloy which has excellent corrosion resistance, high hot hardness, and non-magnetic properties. Because of its superior mechanical and chemical properties, it is being used in extreme environments such as jet engines[1] and oil-field equipment [2]. However, it is one of the most difficult-to-machine material. The responsible properties for poor machinability of Inconel 718 alloy are [33]-

1. High strength at high temperature.
2. High strain sensitivity which leads to work hardening and causing further tool wear.
3. Poor thermal conductivity resulting in high temperature up to 1200^{o}.
4. Presence of abrasive carbide particles causes abrasive tool wear
5. High chemical affinity towards tool materials one of the causes for diffusion type wear.
6. Cutting forces are higher due to high strength which may cause tool chipping

The detrimental properties of Inconel-718 do not only cause severe tool wear but also lead to excessive surface damage, due to the production of high residual stresses[34]. The high temperature and plastic deformation change material structure and it was found that frictional heat and deformation of surface layer during machining change micro-hardness leading to micro cracks on the machined surface[35].

Unlike turning and milling processes, Inconel drilling has received limited attention in the literature. The literature on drilling is mostly focused on the surface integrity of drilled hole and tool wear on twist drills.

Chen et al.[36] conducted series of experiments to study tool wear mechanism in drilling operation on Inconel-718. In their study, multi-layer TiAlN PVD coated tungsten carbide twist drills were used to drill multiple holes of 30mm depth. They found four stages of tool wear. In the first stage, coated layer was abraded followed by the second stage of built-up edge formation. In the third stage, the tool was weakened by propagation of micro-cracks leading to the fourth stage of serious flank and crater wear. During stage four long chips produced due to extrusion mechanism. However, tool life found to be improved by the addition of nanoparticles in the coolant.

Liao et al.[37] studied the feasibility of ultrasonic vibration in the drilling of Inconel-718 using modified chuck with piezo actuators. Tool life was found increased for low-frequency low amplitude vibrations. Also, force values were reduced and easy chip evacuation was reported. However, high amplitude vibration had a negative effect on tool wear.

Sharman et al.[38] evaluated performance of commercially available TiAlN multilayer PVD coated and uncoated drilling tools for aerospace applications. They found that, tools with a curved cutting edge and radius on the periphery show higher tool life as compered to drills with straight or concave cutting edges and sharp periphery. However, hole integrity was not sufficient for aerospace requirement due to smearing effect. They recommended the use of reaming and mill boring for better surface and dimensional integrity.

Deep hole drilling studies conducted by Woon et al.[39] pointed out that inefficient cooling due long chips lead to catastrophic failure of single flute gun drill. They conducted CFD analysis of coolant flow and found that thermal fatigue caused tool failure. In another study [40], straightness profiles of holes with aspect ratio more than 100 were investigated. It was concluded that dimensional inaccuracies during resharpening process were responsible for deviation of straightness profiles.

Imran et al.[41] studied micro-drilling of Inconel-718 alloy. However, the scope of the work was limited to surface integrity and comparative study of tool wear mechanism. The experiments were conducted at dry and wet drilling conditions using micro-drills of diameter 300 to 500 μm.

2.5 Concluding Remarks

Following research gaps were found after the thorough literature review.

- There is limited literature available for deep hole drilling in Inconel-718 moreover, there are no clear guidelines for drilling in difficult-to-machine materials like Inconel-718. The effect of tool geometry and pilot hole bottom during engagement was neglected. Hence, there is a need to quantify the efficacy of tool-workpiece engagement to avoid chipping which was observed in the initial phase of experiments conducted by the author.

- The force models are semi-empirical in nature, which require expensive experiments to determine force coefficients. Moreover, the models do not consider the effect of cutting edge radius on the thrust

force which is significant at lower feed rates employed while drilling in Inconel 718.

- Mechanics of chip formation and mechanism for chip breakage was not studied for single-lip deep hole drilling of the high strength Inconel- 718. Also, it is necessary to quantify the effect of chip morphologies on the drilling thrust force to avoid catastrophic drill failure and expensive repair work.

- Most of the hole accuracy studies were focused on the hole diametrical accuracy and surface integrity. Very few studies were done on straightness prediction or control. The current straightness prediction models cannot be applied to the multi-support deep hole drilling machines.

Hence, it is important to develop a predictive framework for the straightness control in deep hole drilling of Inconel-718 which includes predictive force model considering the effect of cutting edge radius and predictive straightness deviation model.

Chapter 3: Benchmarking of Single-lip Drill Engagement

In the initial experimental studies, it was observed that the deep hole drilling using a single-lip drill (SLD) without a starting bush induces a severe cutting edge chipping if the pilot hole profile is not selected properly. In this chapter, a geometrical model for tool-work engagement is explained and verified experimentally. Finally, a range of parameters is provided to avoid tool chipping and standardized the drilling methodology for further drilling tests.

3.1 Background

The drill geometry for SLD is selected on the basis of the workpiece material, favorable chip shape, hole surface integrity and accuracy requirements of the hole. However, for difficult-to-machine materials such as Inconel-718, the effects of SLD geometries have not been sufficiently understood.

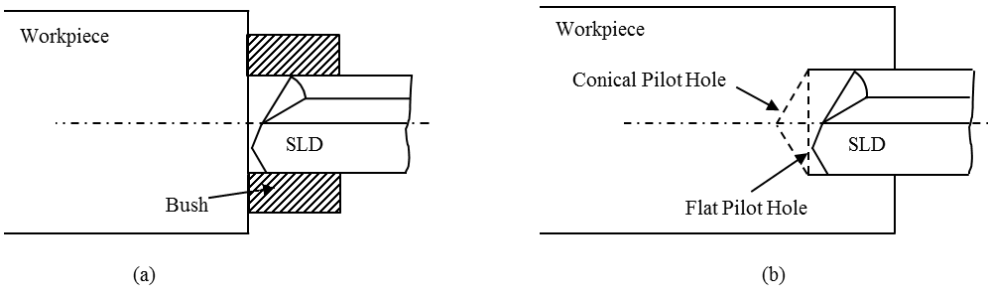

Figure 3.1(a) Deep hole drilling set-up with pilot bush (b) Deep hole drilling with flat or conical pilot hole profile

In conventional deep hole drilling using SLD, a pilot bush is used as shown in Figure 3.1(a) when a special purpose deep hole machinery is available. For smaller components, installation and mounting of a pilot bushes are difficult, time consuming and expensive. Moreover, inner diameter tolerances of guide bushes are difficult to control. If the tolerance is excessive, drills will not be

guided properly. During the preliminary engagement, the drill will slip randomly over the entrance face also known as 'the walking phenomenon' which will ultimately result in 'bell-mouth formation' where the entrance hole diameter is unnecessarily widened [28, 29]. On the other hand, if the tolerance is insufficiently provided, drills will be overly constrained and often break catastrophically upon engagement.

In the absence of specialized deep hole drilling machines, general purpose machining centers and lathe machines can be used alternatively for drilling deep holes. Here, the pilot bush is replaced with pilot holes to guide SLD into the workpiece as shown in Figure 3.1(b). These pilot holes are necessary to facilitate the self-piloting action of SLD during preliminary tool-work engagement. However, preliminary engagements of SLD are not stable because the cutting edge is in partial contact with the workpiece. Moreover, drilling of Inconel-718 produces higher forces than conventional materials which increase the tendency of chipping formation on cutting edges during tool-work engagement if pilot hole geometry is not established properly.

Conventional drilling setup using guide bushes was previously studied by Astakov [28]. It was reported that gundrilling stability during engagement was influenced by the type of guide pads, the diameter of pilot bush and geometry of SLD. Moreover, when pilot holes are made to replace the use of guide bushes, the geometry of pilot holes be it flat or conical (Figure 3.2 (b)) will affect tool-work engagement efficacy, as well. In this chapter, the effect of pilot hole geometry on the tool-work engagement efficacy is studied.

3.2 SLD Engagement

3.2.1 Stability during engagement

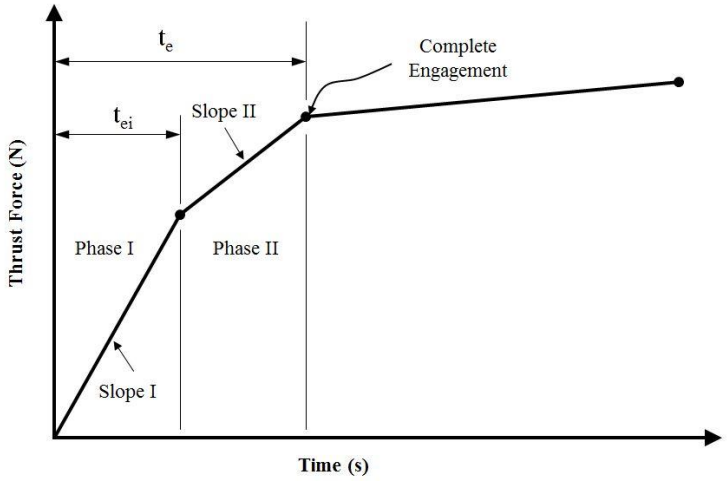

Figure 3.2 Thrust force variation during engagement

The engagement of the SLD with a pilot hole can be divided into two phases as shown in Figure 3.2. The cutting starts when drill touches the workpiece and at the end of Phase-I, one of the edges completes the engagement. Phase-II ends when both the edges are completely engaged with the workpiece. The time required for this engagement has a significant influence on the thrust force and eventually on the tool chipping.

The rate of change of thrust force during engagement is defined by Slope-I and Slope-II for Phase-I and Phase-II respectively. If one of the edges engages quickly with the workpiece, the sudden change in the thrust force will cause chipping on the cutting edges. However, this phenomenon is unexplored and often subjected to the experience of the machine tool operator. Here, a new parameter is introduced for selection of pilot hole for the given drill geometry.

3.2.2 Drilling engagement ratio

To compare the performance of SLD during the engagement, a new parameter called 'Drilling Engagement Ratio' (DER) was introduced. It can be defined as the time required for completion of Phase-I divided by total engagement time.

$$DER = \frac{t_{ei}}{t_e} \tag{3.1}$$

Where, t_{ei} is the time required for completion of Phase I and t_e is the time taken to complete engagement of both the cutting edges. The ratio lies in the range of 0 to 1. The DER has direct influence on the Slope-I of thrust force. The cutting edge will be suddenly engaged with workpiece when DER is near 0 and Slope-I will be near 90^o. Whereas, cutting edges will engage smoothly when DER is near one meaning the time taken for completion of Phase-I and total engagement time are equal. For smoother engagement, DER near one is preferred. The DER can be calculated based on the combination of tool and pilot hole geometry.

3.2.3 Engagement times

Depending on tool geometry and pilot hole profile, the engagement can be classified in four different ways. The four cases are as depicted in Figure 3.3-3.6. The dotted line in the figures represents drill location at the end of complete engagement and total distance travelled by drill before total engagement is given by L_e. The drill geometry was defined by four parameters; inner cutting edge angle (φ_i), outer cutting edge angle (φ_o),

location of drill apex point from center (c_p) and radius of the drill (R). The pilot hole geometry was characterized by angle of conical bottom (θ_c). For each case, the Phase-I completes when point 'c' reaches point 'r' and the time required for completion of Phase I is given by t_{ei} and can be calculated using Eq.(3.2)-(3.9) where distance travelled by drill depends on the combination of pilot hole and drill geometry.

3.2.3.1 Case I: $l_i + l_c > l_o$; $L_e = l_i + l_c$

Initially, the apex point will come in contact with the hole bottom, at the end of Phase-I outer edge will be in complete contact with the workpiece. Once, the point 'a' on drill reaches the point 'p', the engagement completes. The time taken for completion of Phase-I and complete engagement is given as,

$$t_{ei} = \frac{l_o}{f} = \frac{c_p\left(\tan\varphi_o - \cot\frac{\theta_c}{2}\right)}{f} \tag{3.2}$$

$$t_e = \frac{L_e}{f} = \frac{c_p\left(\tan\varphi_i + \cot\frac{\theta_c}{2}\right)}{f} \tag{3.3}$$

3.2.3.2 Case II: $l_i + l_c < l_o$; $L_e = l_i + l_c$

In this case, the apex point will come in contact with the hole bottom, however, at the end of Phase-I, inner edge will be in full contact with the workpiece. The time taken for completion of Phase I and complete engagement is given as,

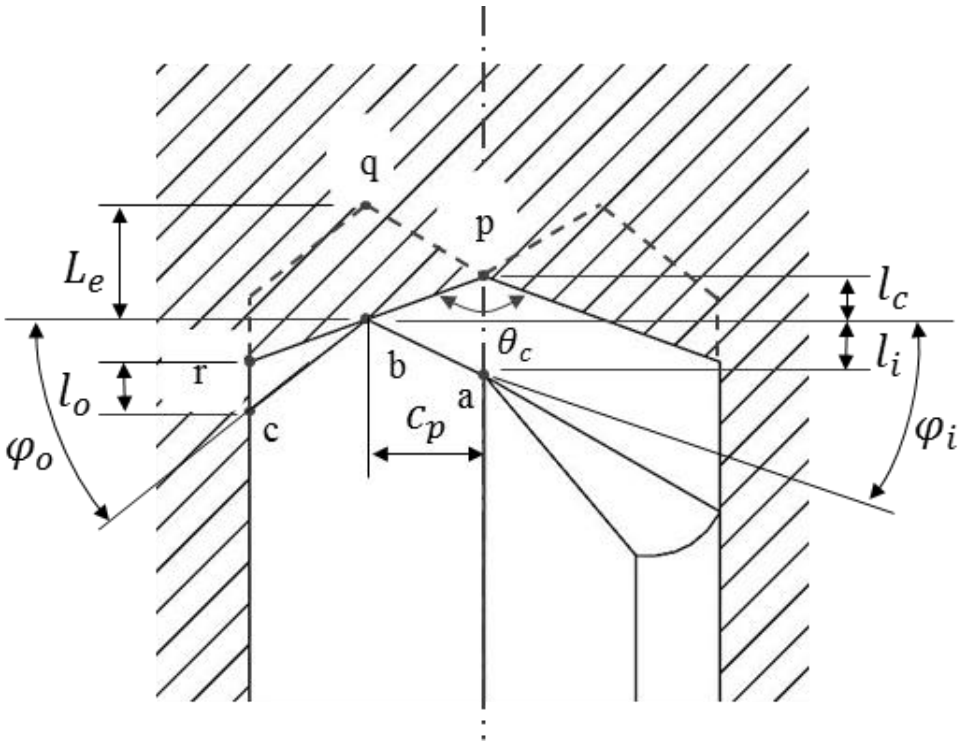

Figure 3.3 Case I: $l_i + l_c > l_o$; $L_e = l_i + l_c$

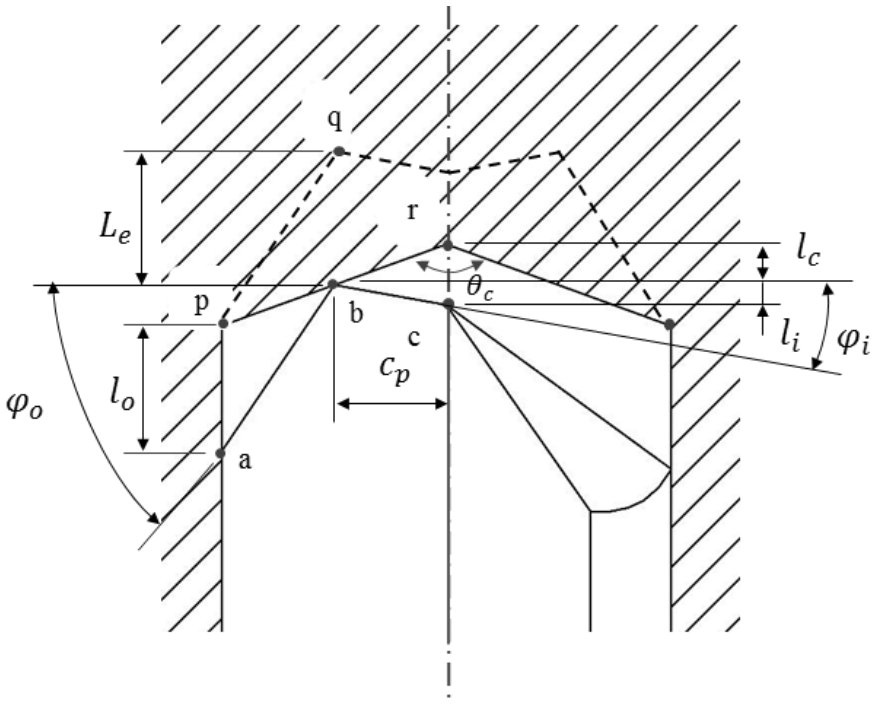

Figure 3.4 Case II: $l_i + l_c < l_o$; $L_e = l_i + l_c$

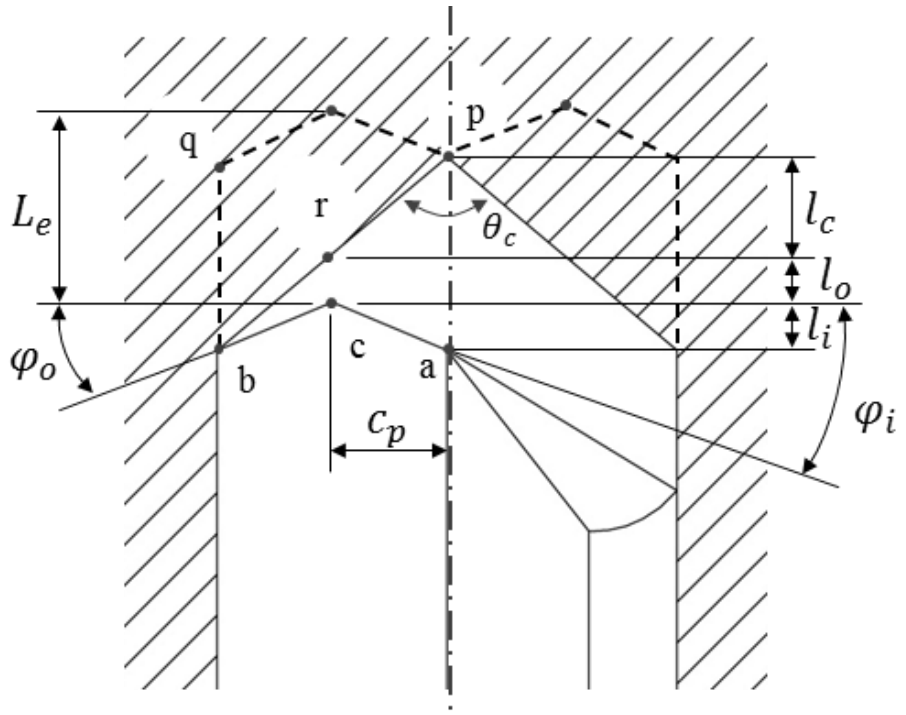

Figure 3.5 Case III: $\frac{\theta}{2} > \varphi_o$; $L_e = l_i + l_c + l_o$

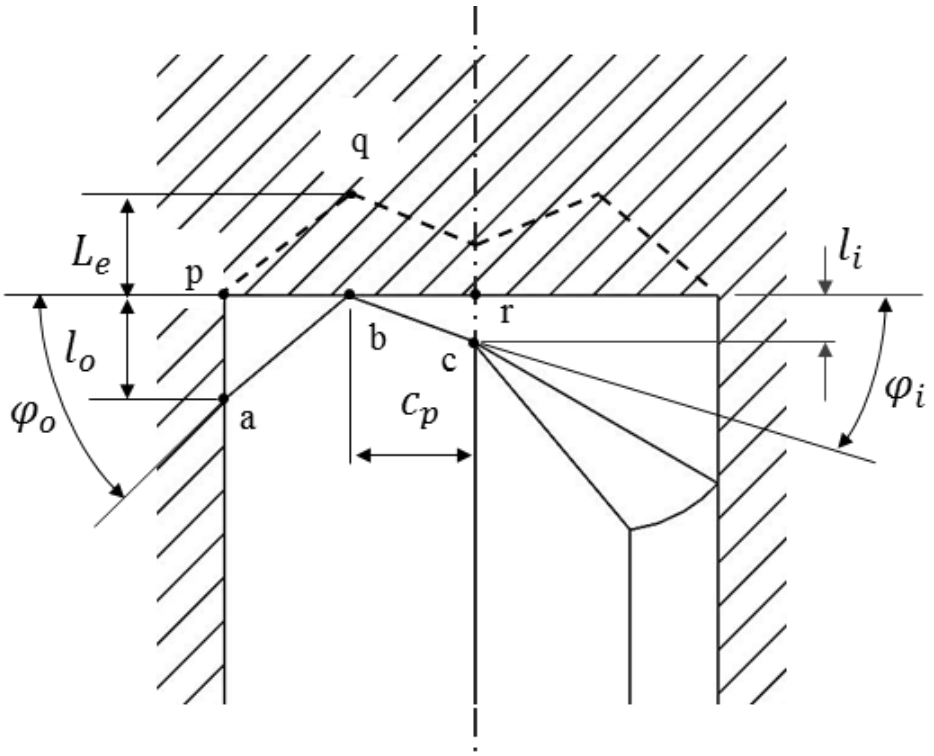

Figure 3.6 Case IV: $\theta = 180^o$ (Flat bottom pilot hole), $L_e = l_o$

$$t_{ei} = \frac{l_i + l_c}{f} = \frac{c_p\left(\tan\varphi_i + \cot\frac{\theta_c}{2}\right)}{f} \tag{3.4}$$

$$t_e = \frac{L_e}{f} = \frac{\left(R - c_p\right)\left(\tan\varphi_o - \cot\frac{\theta_c}{2}\right)}{f} \tag{3.5}$$

3.2.3.3 Case III: $\frac{\theta}{2} > \varphi_o;\ L_e = l_i + l_c + l_o$

Contrary to Case I and Case II, the outermost point engages first with the hole bottom and at the end of Phase-I outer edge is completely engaged with the hole bottom. The time taken for completion of Phase-I and complete engagement is given as,

$$t_{ei} = \frac{l_o}{f} = \frac{(R - c_p)\left(\cot\frac{\theta_c}{2} - \tan\varphi_o\right)}{f} \tag{3.6}$$

$$t_e = \frac{c_p\left(\tan\varphi_i + \cot\frac{\theta_c}{2}\right) + (R - c_p)(\cot\frac{\theta_c}{2} - \tan\varphi_o)}{f} \tag{3.7}$$

3.2.3.4 Case IV: $\theta = 180^o$ *(Flat bottom pilot hole),* $L_e = l_o$

In this case, the pilot hole bottom is kept flat where the apex point engages first and at the end of Phase-I inner cutting edge is in complete contact with the workpiece. Especially, this condition is very commonly encountered in the case of supported deep hole drilling machine where pilot bushes are used. The time taken for completion of Phase I and complete engagement is given as,

$$t_{ei} = \frac{l_i}{f} = \frac{c_p \tan \varphi_i}{f} \tag{3.8}$$

$$t_e = \frac{L_e}{f} = \frac{(R - c_p) \tan \varphi_o}{f} \tag{3.9}$$

3.3 Experiments

Experimental studies were carried out on DMU 80P duoBLOCK® five-axis machining center. A combination of four SLD geometries and three pilot holes were tested. The feed rate (*f*) and the RPM were kept 8 mm/min (0.010 mm/rev) and 800 respectively. In addition, coolant pressure of 4MPa was used. Total 12 distinctively different combinations were used during the experiments as depicted in Figure 3.7.

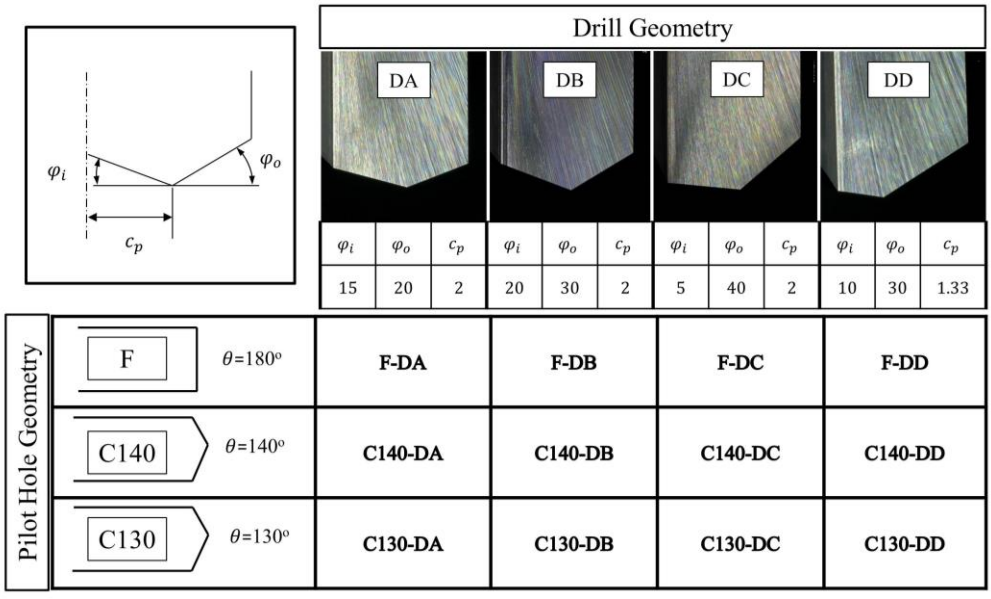

Figure 3.7 Experimental conditions for SLD engagement study

The conical pilot holes, C140 and C130 were drilled using self-centering twist drills with lip angle 140 and 130 respectively. The twist diameter was 7.8 mm

and pilot holes were drilled up to the depth of 1.5D i.e. 12 mm. The holes were reamed to a final diameter of 8 mm. End-mill was used to machine four flat bottom pilot holes. The diameter and roundness values of the reamed holes were measured by CMM and found to be in the tolerance range of IT7 in order to eliminate the effects of pilot hole finishing on the engagement behavior. Two repetitions were performed for each drilling condition. The mechanical properties of workpiece material are given in Table 3.1.

The cutting forces were acquired using Kistler Type 9257B multicomponent dynamometer and vibrations were captured using accelerometer sensor Kistler Type 8762A50. The SLD was inserted into the pilot hole up to the length of 8 mm without any rotation. Then the feed was given along with coolant supply. Drilling was continued up to the length of 8 mm to simulate the engagement process.

Table 3.1 Mechanical properties of Inconel-718 workpiece.

Yield Point (MPa)	Tensile Strength (MPa)	Elongation (%)	Area Reduction (%)	Hardness (HRC)
1058	1327.5	10	20	42-45

3.4 Results and Discussions

The DER calculated based on the geometrical model can provide qualitative criteria for selection of appropriate pilot hole. The critical range of values for DER has to be found based on Slope-I and its effect on the tool. In this

section, the calculation for Slope-I/-II and its relation with DER are explained. Finally, a range of DER values for Inconel 718 was recommended based on observations on tool chipping during the engagement.

3.4.1 Calculation of Slope-I and Slope-II

For calculating the Slope I, the thrust force was plotted against time using MATLAB. The times required for completing Phase I and II were calculated based on the experimental conditions using Eq(3.2)-(3.9). The values of forces at the completion of Phase I and Phase II were manually determined at the respective timing. The procedure is illustrated in Figure 3.8 for experimental condition C140-DB. For C140-DB, the apex point touches the pilot hole bottom first and the Phase I completed when the outer edge was completely engaged with the workpiece. The time required for completion of Phase I and complete engagement of both cutting edges were calculated using Eq. (3.2) and (3.3).

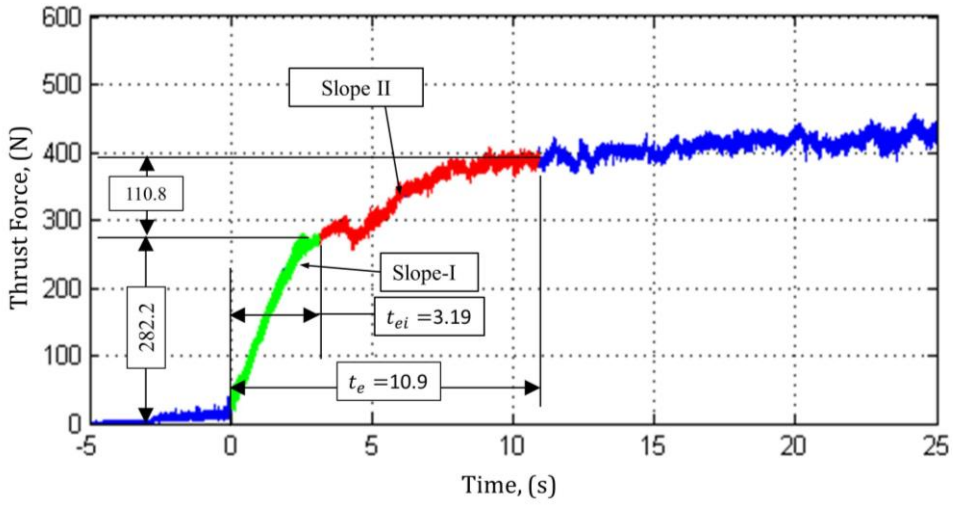

Figure 3.8 Calculation of Slope-I and Slope-II

The force values were determined from the graph at the calculated t_{ei} and t_e. Slope-I and Slope-II were calculated using force values and time.

Table 3.2 Calculated DER, Slope-I and Slopes-II values for experimental conditions

Case No.	Experimental Condition	t_{ei}	t_e	DER	Slope-I (^{o})	Slope- II (^{o})
I	C140-DA	0	9.5	0	90	52.05
	C140-DB	3.19	10.9	0.29	77.25	35.67
	C140-DD	2.13	5.40	0.39	80.60	69.42
	C130-DB	1.67	12.45	0.13	78.76	38.64
	C130-DC	5.6	8.3	0.67	68.78	37.12
	C130-DD	1.11	6.47	0.17	82	70.04
II	C140-DC	6.75	7.13	0.94	67.34	41.35
III	C130-DA	1.53	12.43	0.12	84.18	21.27
IV	F-DA	4.01	5.46	0.73	75.15	67.33
	F-DB	5.45	8.66	0.62	70.06	52.95
	F-DC	1.31	12.58	0.10	83.80	50
	F-DD	1.76	11.54	0.15	78.11	54.23

Similarly, the force signals for all the experimental conditions were analyzed and the slopes were calculated. The results were categorized into four classes based on the engagement conditions. The results are summarized in Table 3.2.

3.4.2 Relation between DER and Slope-I /Slope-II

Slope-I and II were plotted against DER and it was observed that the Slope-I decreases linearly with respect to DER. The relation between DER and Slope-I signify the importance of the DER and its effectiveness for performance evaluation during the engagement. However, Slope-II did not show any relation with DER.

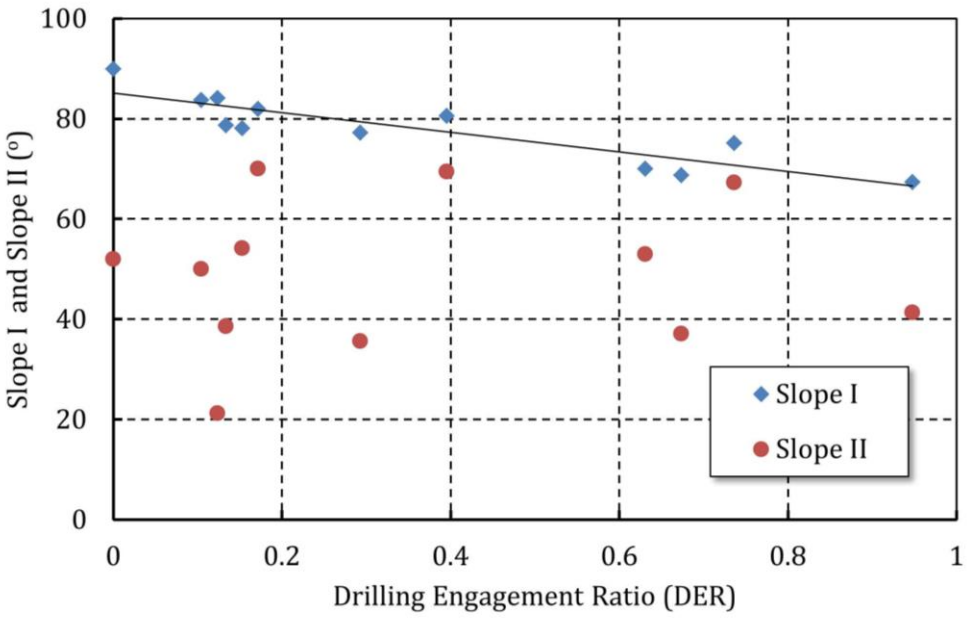

Figure 3.9 Slope-I and Slope-II plotted against Drilling Engagement Ratio

As it can be seen in Figure 3.9, Slope-II is always smaller than Slope-I for all the experimental conditions. The effects of pilot hole geometry on the Slope-I and tool chipping is shown in Figure 3.10. When drill DC was used with a flat pilot hole (F-DC), the inner edge quickly engaged with the workpiece (DER=

0.1) causing a sudden increase in thrust force on the inner edge. As a result, the Slope-I was 83.80 and inner edge experienced heavy chipping. Whereas, the same drill geometry when used with a conical pilot hole (C140-DC), both edges engaged gradually (DER=0.94) hence the change in thrust force was not drastic (Slope-I= 67.34). Hence, no chipping was observed in the case of C140-DC. The opposite effect of pilot hole geometry was found in the case of drill DB. It did not experience any chipping when a flat pilot hole was used (Figure 3.11 (i)). However, the same tool experienced chipping on the outer edge when used with conical bottom pilot hole (θ_c=130 and 140) as shown in Figure 3.11(d)&(g).

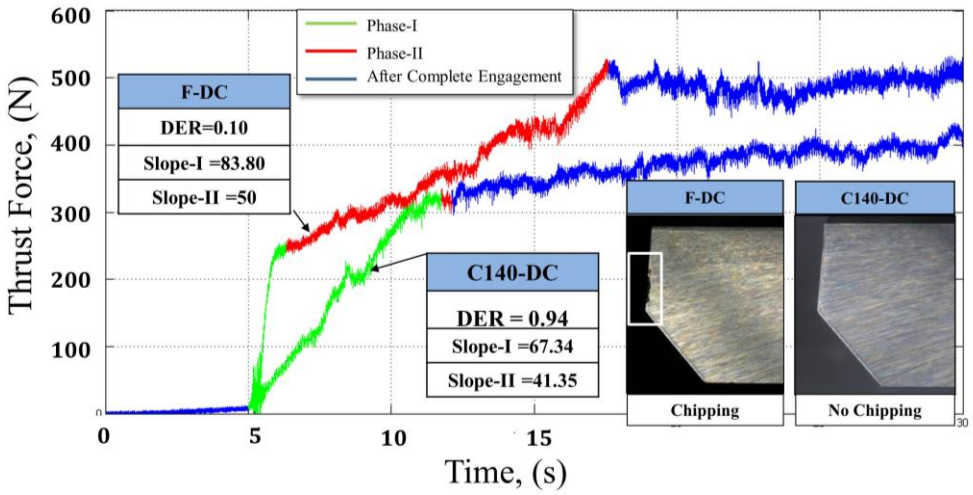

Figure 3.10 Effect of pilot hole geometry on Slope-I/II and cutting edge chipping for drill DC

It was found that for DER < 0.4, chipping was severe on the edge which engaged first with the workpiece as compared to the other edge. However, for DER> 0.6 uniform wear was observed along both the cutting edges. The tool wear study showed that drills with an inner angle less than 10^o were susceptible to chipping when used with flat bottom hole, whereas, other tools showed smooth engagement with flat pilot hole. The range for smooth

engagement for drilling alloy 718 was defined as 0.6 < DER < 1. These observations were also consistent with the second set of experiment.

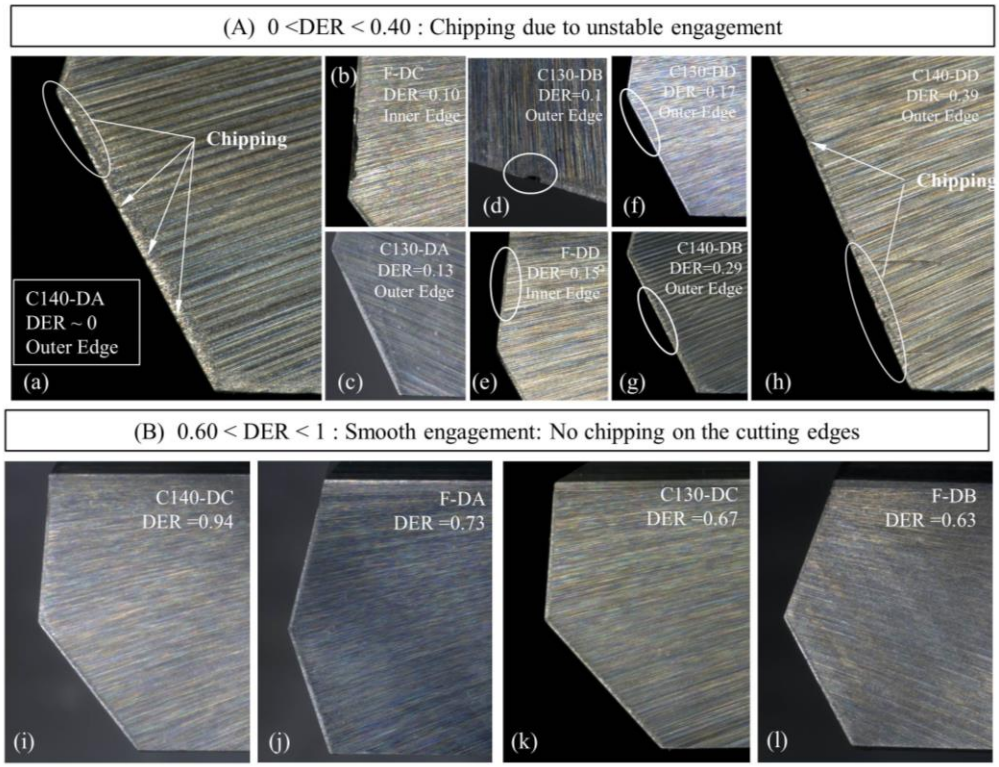

Figure 3.11 Effect of Drilling Engagement Ratio on tool edge chipping (a) Unstable Engagement and severe chipping on the cutting edge for 0<DER<0.4 (b) Smooth Engagement and uniform wear along cutting edges for 0.6<DER<1.

3.5 Concluding Remarks

Based on the analysis and experimental results following conclusions are derived for the too-work engagement efficacy.

- The pilot hole has to be reamed to IT7 diametrical tolerance as the conventional twist drills fail to meet the requirement.

- It is important to consider the effect of pilot hole bottom geometry on the deep hole drilling process in addition to the diametrical accuracy of the pilot hole.

- The drilling engagement ratio provides a quantitative approach to avoid the probability of drilling edge chipping during engagement phase. The DER should be kept in the range of 0.6 to 1 to reduce the probability of cutting edge chipping during the engagement.

- The SLD with an inner angle less than 10 should not be used with a flat bottom pilot hole. This is an important finding which is not only applicable in unsupported but also in supported deep hole drilling process where the pilot bush and the workpiece form the flat bottom hole case.

- The study provided guidelines for conducting further experiments used in this research.

Chapter 4: Predictive Modelling of Drilling Forces

In this chapter, a comprehensive predictive model for single-lip drill (SLD) drilling forces considering the effect of edge radius is proposed. Initially, a detail geometrical model for tool geometry is presented followed by the drill force system. A wide range of drilling experiments was carried out to check the accuracy of the predictive model.

4.1 Modelling Framework

The modelling framework for single-lip drilling is summarized in Figure 4.1.

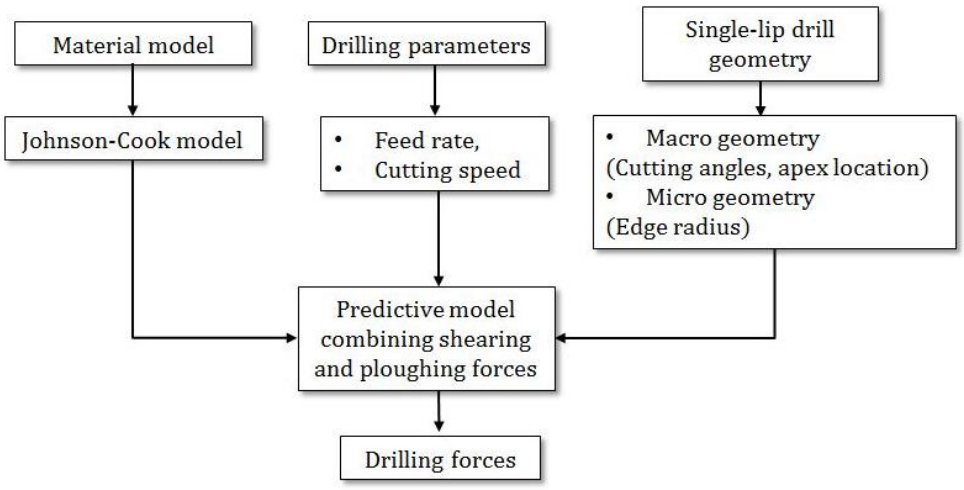

Figure 4.1 Modelling framework for the single-lip drilling forces

There are three main input categories required for the thrust force prediction-material properties, drilling parameters and SLD geometry. In this study, unlike the previous models as reviewed in the section 2.3.1 a new parameter, cutting edge radius is added. The material behavior is modeled using the Johnson and Cook (J-C) material model. The shearing and ploughing components of the drilling forces are predicted and combined in order to obtain the total drilling forces.

4.2 Force System

4.2.1 Coordinate systems

A rotating frame of reference $(x_t y_t z_t)$ is defined at the center of the drill, where z_t axis is parallel to the drill axis. The x_t axis passes through the apex point of the drill and y_t axis is perpendicular to the x_t and z_t axes. The workpiece coordinate system (XYZ) is a fix co-ordinate system parallel to the dynamometer co-ordinate system where the Z axis is parallel to z_t and normal to $x_t y_t$ plane. The angle of rotation for $(x_t y_t z_t)$ with respect to the (XYZ) is ϕ_r.

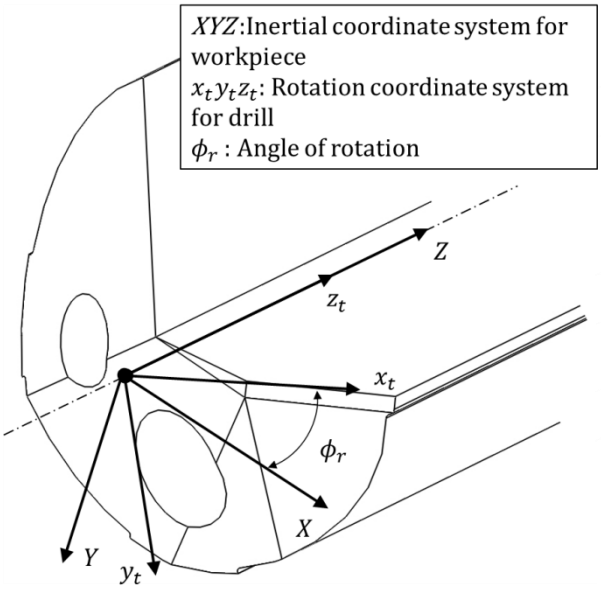

Figure 4.2 Inertial and rotational coordinate systems for SLD

4.2.2 Drill geometry

The drill geometry of the single-lip drill is defined as shown in Figure 4.3. The major macro parameters are inner cutting edge angle (φ_i), outer cutting edge angle(φ_o), apex point (c_p) and tool cutting edge rake angle (α) in addition to

the micro geometry parameter cutting edge radius (r_e). The effective rake angle (α_e) is influenced by the ratio (t_o/r_e) of uncut chip thickness (t_o) to the cutting edge radius (r_e).

The effective rake angle (α_e) can be calculated using the method suggested by Bissacco et al. [42] as follows.

$$\alpha_e = \sin^{-1}\left(\frac{t_o}{r_e} - 1\right) \; for \; t_o < t_{lim}$$
$$\alpha_e = \alpha \; for \; t_o > t_{lim} \tag{4.1}$$

Where t_{lim} is calculated using Eq.(4.2).

$$t_{lim} = r_e(1 + \sin\alpha) \tag{4.2}$$

4.2.3 Drilling forces

The drilling forces on cutting edges were determined by dividing the edges into m_i elements at inner cutting edge and m_o elements at outer cutting edge of length dr each. The cutting element dr is considered as the orthogonal cutting element. The width of cutting element along the cutting edge is,

$dw_i = \frac{dr}{\cos\varphi_i}$ at inner cutting edge and

$dw_o = \frac{dr}{\cos\varphi_o}$ at outer cutting edge.

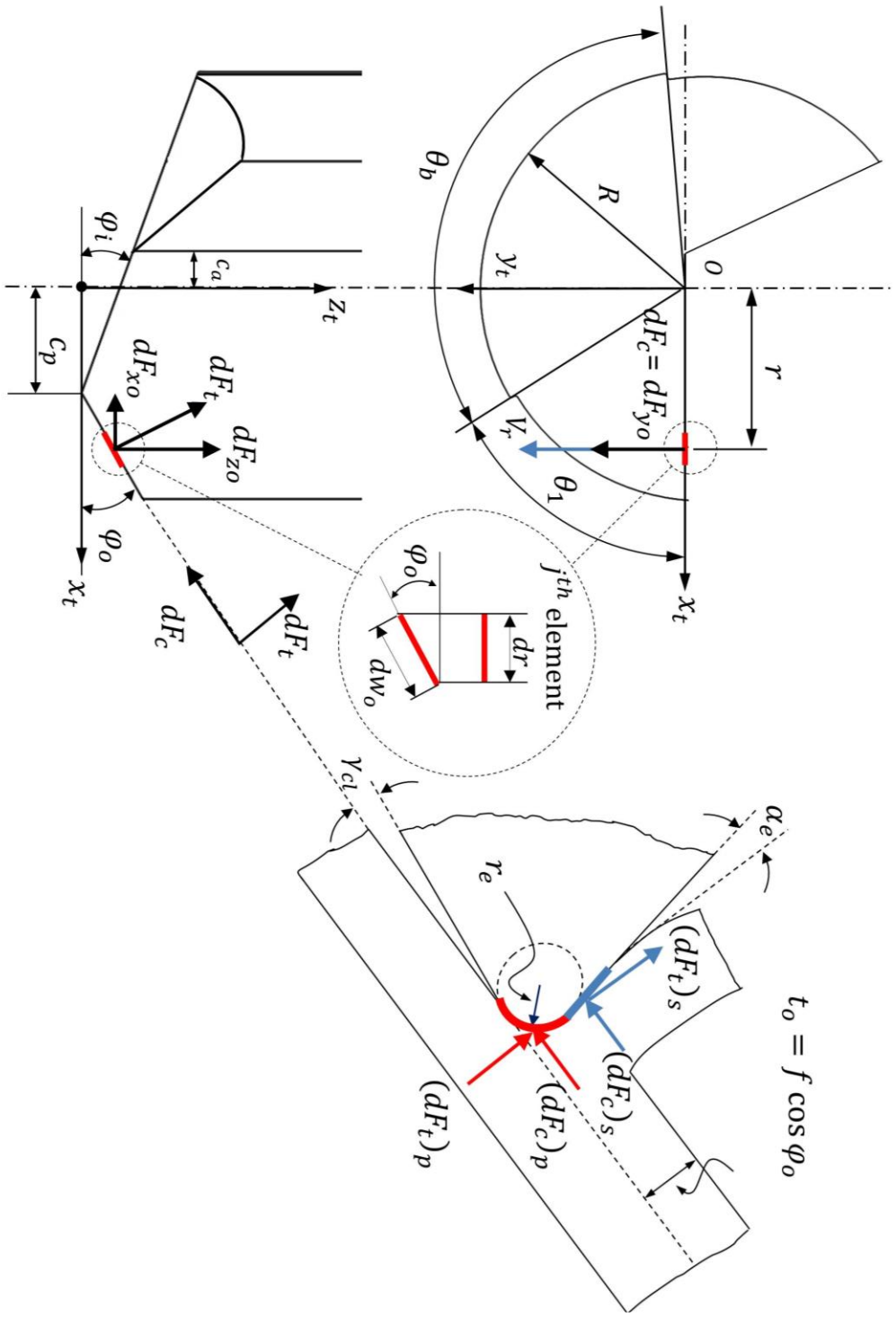

Figure 4.3 Drill geometry and drilling forces

The shearing components of the forces acting on the cutting elements are $(dF_c)_s$ and $(dF_t)_s$. The elemental force $(dF_c)_s$ is parallel to the direction of cutting velocity (V_r) at any given radius (r) whereas $(dF_t)_s$ is normal to the plane containing cutting velocity and cutting edge. The ploughing components were added to the shearing components to get total elemental forces in cutting anf feed directions are,

$$dF_c = (dF_c)_s + (dF_c)_p \tag{4.3}$$

$$dF_t = (dF_t)_s + (dF_t)_p \tag{4.4}$$

Where, $(dF_c)_p$ and $(dF_t)_p$ are the ploughing components in cutting and feed direction respectively. The elemental forces in the tool coordinate system are given as Eqs.(4.5)-(4.7) for outer cutting edge and Eqs.(4.8)-(4.10) for inner cutting edge.

$$|dF_{zo}| = |dF_t| \cos \varphi_o \tag{4.5}$$

$$|dF_{xo}| = |dF_t| \sin \varphi_o \tag{4.6}$$

$$\left|dF_{yo}\right| = |dF_c| \tag{4.7}$$

$$|dF_{zi}| = |dF_t| \cos \varphi_i \tag{4.8}$$

$$|dF_{xi}| = |dF_t| \sin \varphi_i \tag{4.9}$$

$$\left|dF_{yi}\right| = |dF_c| \tag{4.10}$$

The total drilling forces in tool coordinate system are given as,

$$F_{xt} = F_{xi} - F_{xo} = \sum_{j=1}^{m_i} (dF_{xi})_j - \sum_{j=m_i+1}^{m_i+m_o} (dF_{xo})_j \tag{4.11}$$

$$F_{yt} = \left(F_{yi} + F_{yo}\right) = \sum_{j=1}^{m_i} (dF_{yi})_j + \sum_{j=m_i+1}^{m_i+m_o} \left(dF_{yo}\right)_j \tag{4.12}$$

$$F_{zt} = F_{zi} + F_{zo} = \sum_{j=1}^{m_i} (dF_{zi})_j + \sum_{j=m_i+1}^{m_i+m_o} (dF_{zo})_j \tag{4.13}$$

Finally, the forces are transformed into inertial frame of reference using following transform matrix,

$$\begin{bmatrix} F_X \\ F_Y \\ F_Z \end{bmatrix} = \begin{bmatrix} \cos\phi_r & \sin\phi_r & 0 \\ -\sin\phi_r & \cos\phi_r & 0 \\ 0 & 0 & 1 \end{bmatrix} \begin{bmatrix} F_{xt} \\ F_{yt} \\ F_{zt} \end{bmatrix}$$

4.2.4 Material model

In this study, Johnson and Cook (J-C) material model is used to define flow stress of the work material. In J-C model, the flow stress (σ) is defined as the function of the yield strength, strain rate and change in temperature [43] as Eq.(4.14).

$$\sigma = (A + B\varepsilon^{n})(1 + C ln\frac{\dot{\varepsilon}}{\dot{\varepsilon_o}})(1 - \left[\frac{T - T_o}{T_m - T_o}\right]^{m}) \quad (4.14)$$

Where, ε is the average shear strain, $\dot{\varepsilon}$ is the average shear strain rate and $\dot{\varepsilon}_o$ is the reference plastic strain rate, T is the instantaneous temperature of the workpiece, T_m and T_o are the melting temperature and the room temperature respectively. Moreover, A is the yield strength of the material, B is the strength coefficient, C is the strain rate constant, n is the strain hardening coefficient and m is the temperature exponent. The material parameters used by various researchers for Inconel-718 are summarized in Table 4.1.

Table 4.1 The J-C material parameters for Inconel-718

Reference	A (MPa)	B (MPa)	C	n	m	$\dot{\varepsilon_o}$ (s^{-1})	Heat Treatment
Ref. [44]	450	1798	0.0312	0.9143	0	1.0	Annealed
Ref. [44]	1350	1139	0.0134	0.6522	0	1.0	Aged
Ref. [45]	450	1700	0.017	0.65	1.3	0.001	Annealed
Ref.[46]	1241	622	0.0134	0.6522	0	1	Aged
Ref. [47]	1241	622	0.0134	0.6522	1.3	1	Aged

The average yield strength of the age hardened Inconel-718 used in this analysis is 1300 MPa. Hence, the material properties used by Lorentzon et al. [47] were selected for the calculation purposes.

The thermal conductivity and specific heat capacity are defined as the function of temperature. The variation of these properties with respect to temperature is shown in Figure 4.4 and Figure 4.5. The Eq.(4.15) and Eq.(4.16) are obtained by the curve fitting of the data for thermal conductivity and thermal specific heat capacity of Inconel-718 respectively.

$$K = 0.016T + 6.67 \tag{4.15}$$

$$C_p = 290.92 - 9 \times 10^{-12}T^{5} + 3 \times 10^{-8}T^{4} - 3 \times 10^{-5}T^{3} + 0.0102T^{2} - 0.9215T \tag{4.16}$$

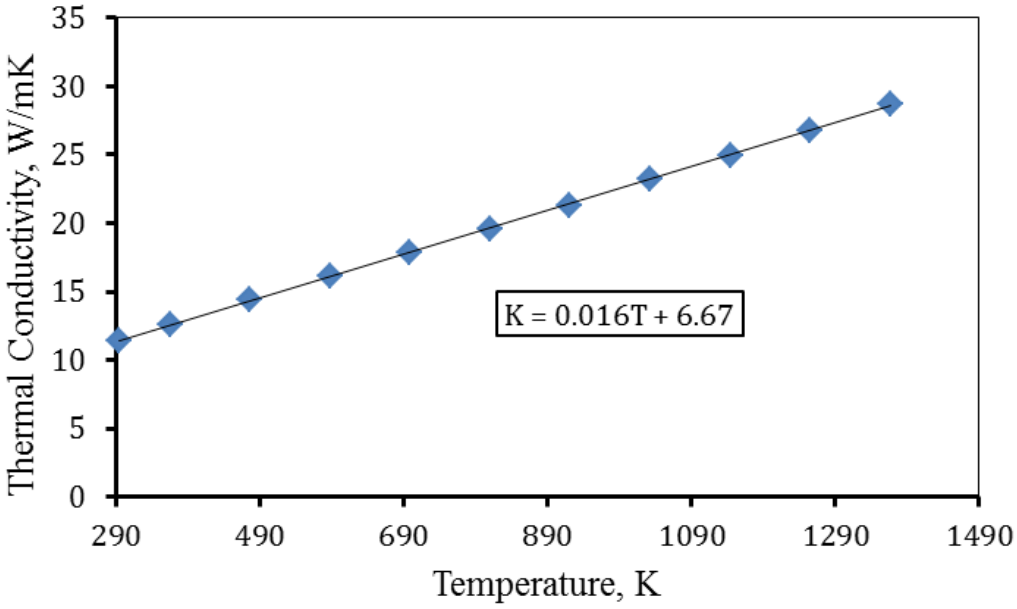

Figure 4.4 Variation in thermal conductivity (K) with respect to temperature for Inconel-718[48]

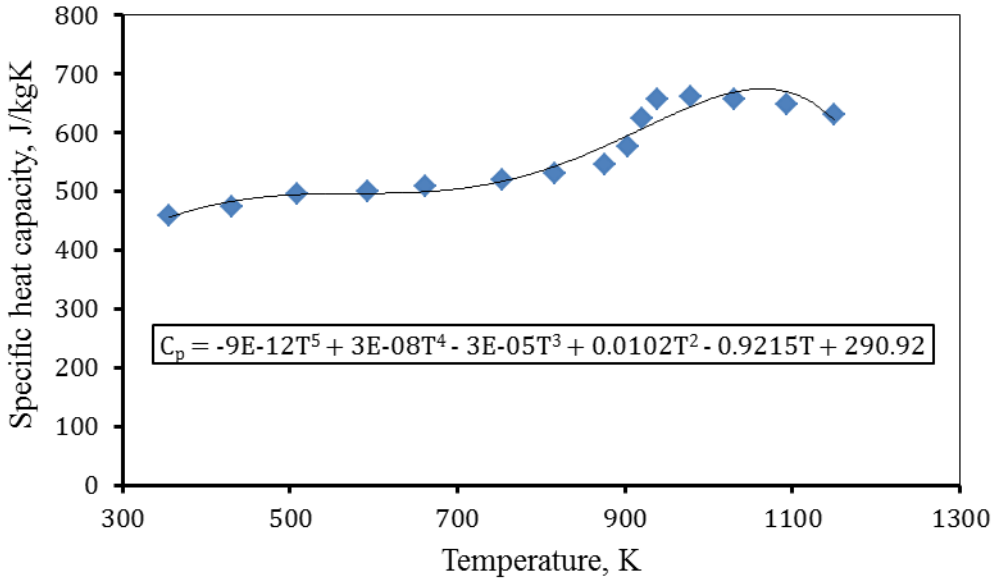

Figure 4.5 Variation in specific heat capacity (C_p) with respect to temperature for Inconel-718 [49, 50]

4.3 Prediction of the Drilling Forces

The framework for the prediction of the drilling forces is depicted in Figure 4.6. A MATLAB program was written to automate the iterative process. Initially, J-C material model related parameters, thermal properties and mechanical properties were given as input. In addition, the tool geometry parameters such as cutting edge radius on the inner edge (r_{ei}), cutting edge radius on the outer edge (r_{eo}) were updated in the program.

The number of cutting elements at inner cutting edge (m_i) and outer cutting edge (m_o) were calculated considering the length of each cutting element (dr). The other parameters such as cutting edge width (dw) and uncut chip thickness were calculated at inner and outer cutting edges separately. The prediction of $(dF_c)_s$, $(dF_t)_s$, $(dF_c)_p$ and $(dF_t)_p$ is discussed in the following sections.

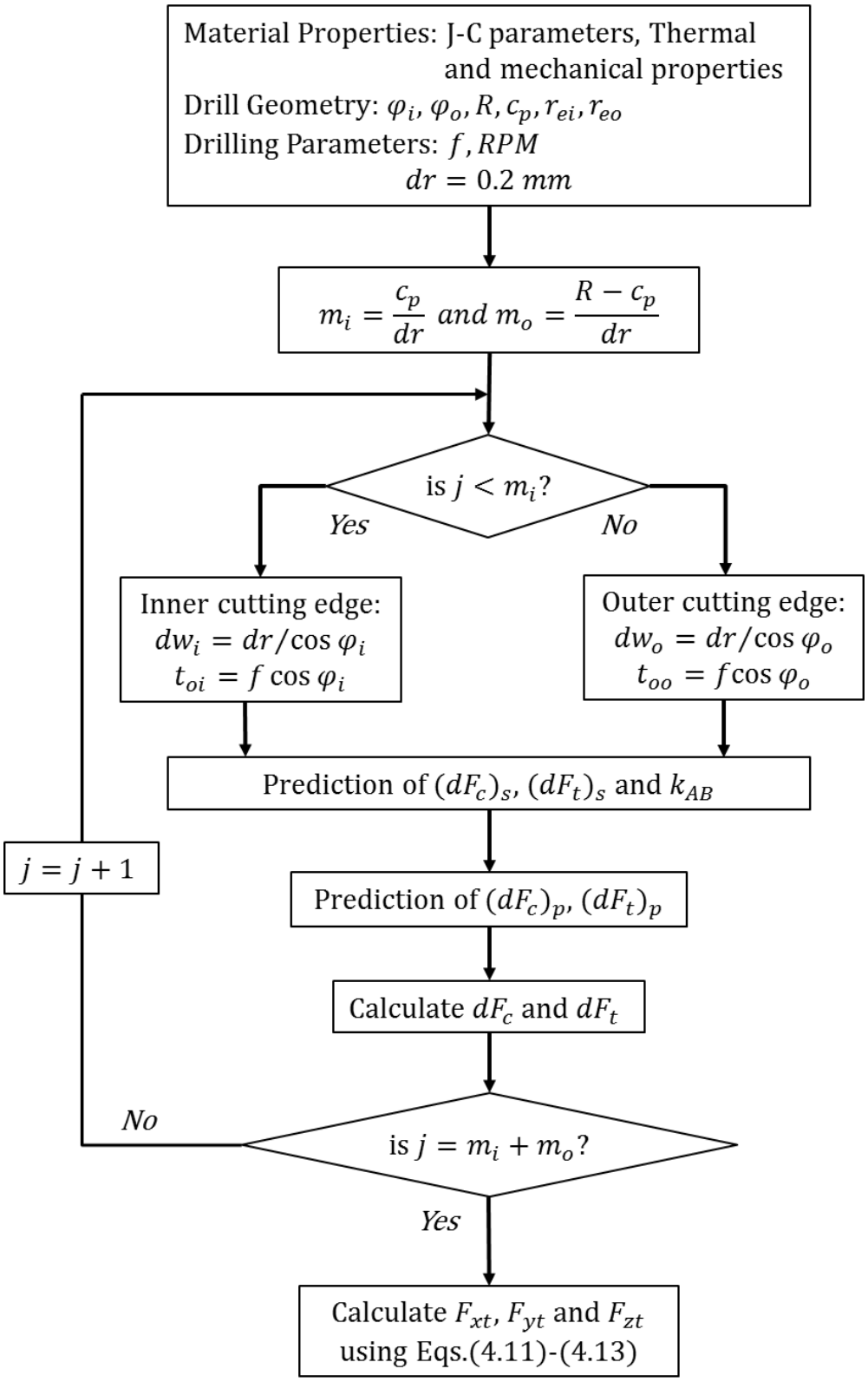

Figure 4.6 Flowchart for prediction of the drilling forces

4.3.1 Prediction of $(dF_c)_s$ and $(dF_t)_s$

The shearing forces in cutting and feed direction were calculated using parallel-sided shear zone theory developed by Oxley. The predictive analytical model developed by Oxley [51] used power law material model for flow stress calculations.

$$\sigma = \sigma_1 \varepsilon^n \tag{4.17}$$

Where, σ is flow stress and ε is strain, the constants σ_1 and n are strength and strain hardening coefficients respectively. The constants depend on the velocity modified temperature. However, the power law material model is available for the limited number of materials such as low carbon steels and few aluminum alloys. Hence, Amir H. Adibi-Sedeh et al. [52] extended the predictive modelling theory to use other material models such as J-C model. The extended model was improved by Lalwani et al. [53] by modifying the strain hardening constant. In this study, extended Oxley's predictive model for J-C developed by Lalwani et al. [53] is used to predict shearing force components in the cutting and thrust direction.

The primary shear zone (PSZ) was modelled as parallel-sided with line AB as straight slip line which is depicted in Figure 4.7. The tool-chip interface is also called the secondary shear zone (SSZ) which is assumed to be of constant thickness for simplifying the analysis.

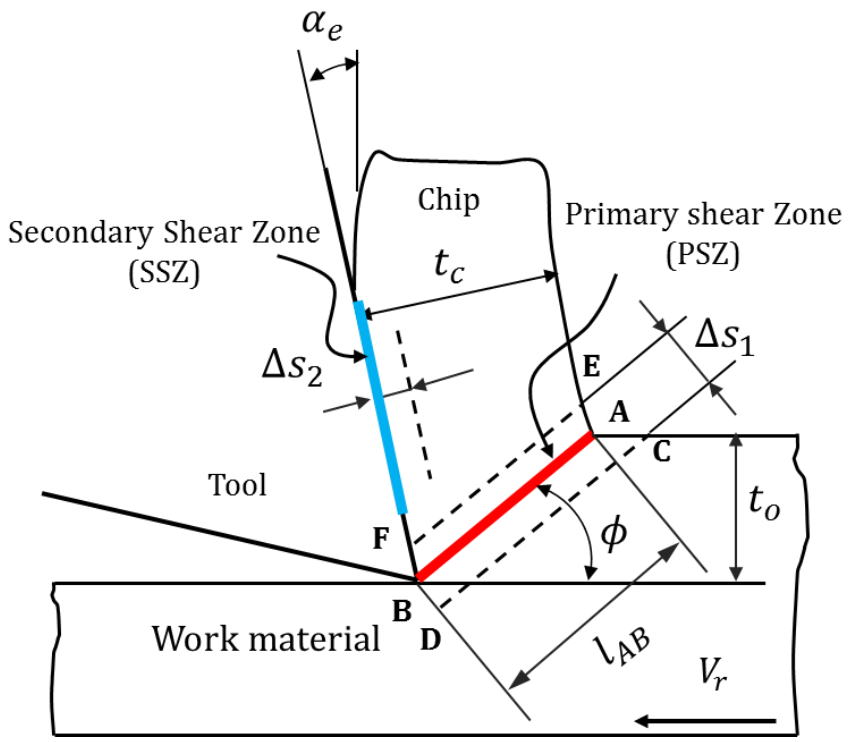

Figure 4.7 Oxley's parallel sided slip-line model

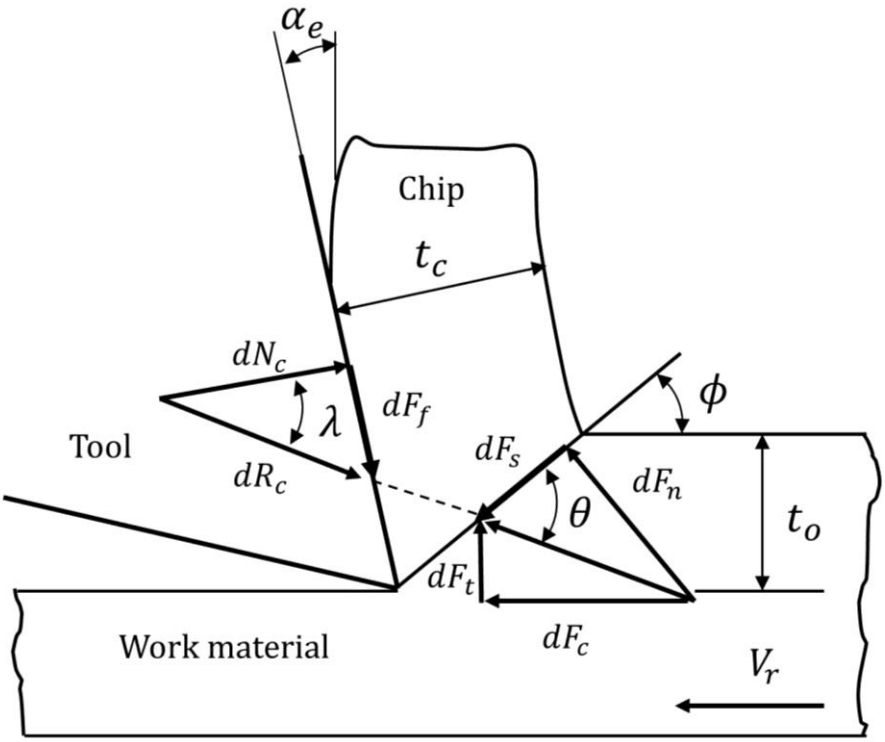

Figure 4.8 Elemental forces acting at PSZ and SSZ

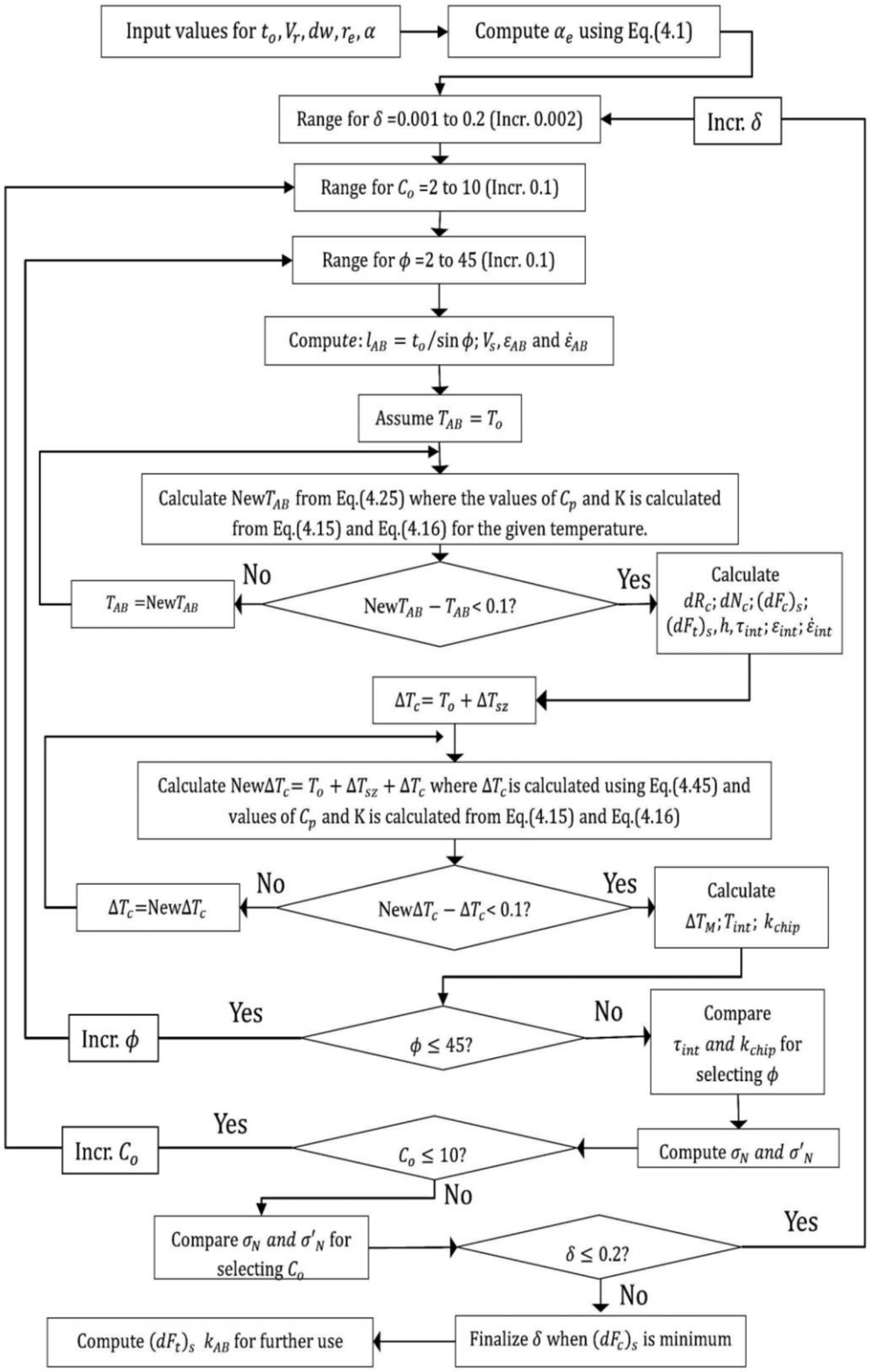

Figure 4.9 Flowchart for prediction of $(dF_c)_s$ and $(dF_t)_s$

In order to predict the forces, shear angle (ϕ) must be determined with two other constants, C_o and δ. The strain rate constant, $C_o(= l_{AB}/\Delta s_1)$ relates shear strain rate with the length of primary shear zone whereas $\delta(= \Delta s_2/t_c)$ is the ratio of plastic zone thickness (Δs_2) at tool-chip interface and the chip thickness (t_c). The shear angle (ϕ), constants C_o and δ are determined by an iterative process as shown in Figure 4.9 where the following three conditions are met. A MATLAB program was written to automate the iterative process.

Condition 1: For determination of shear angle, the shear stress (τ_{int}) at tool-chip interface should be equal to the shear flow stress in the chip material (k_{chip}).

Condition 2: For finalizing the value of C_o, the normal stress (σ_N) at tool-chip interface should be equal to the normal stress (σ'_N) at point B.

Condition 3: The value of δ is finalized where $(dF_c)_s$ is minimum.

The resultant force acting on at PSZ is in equilibrium with the resultant force acting at SSZ as shown in Figure 4.8. The relation of the forces is given by Eqs.(4.18)-(4.23)

$$dR_c = \frac{dF_s}{\cos\theta} \tag{4.18}$$

$$dF_f = dR_c \sin\lambda \tag{4.19}$$

$$dN_c = dR_c \cos\lambda \tag{4.20}$$

$$(dF_c)_s = dR_c \cos(\lambda - \alpha_e) \tag{4.21}$$

$$(dF_t)_s = dR_c \sin(\lambda - \alpha_e) \tag{4.22}$$

$$dF_s = k_{AB} l_{AB} dw \tag{4.23}$$

The flow stress (k_{AB}) at the primary shear zone is calculated as,

$$k_{AB} = \frac{\sigma_{AB}}{\sqrt{3}} = \frac{1}{\sqrt{3}}(A + B\varepsilon_{AB}^{n})(1 + Cln\frac{\dot{\varepsilon}_{AB}}{\dot{\varepsilon}_o})(1 - \left[\frac{T_{AB} - T_o}{T_m - T_o}\right]^{m}) \tag{4.24}$$

The parameters required to calculate the flow stress are determined as follows. The average temperature in the primary shear zone (T_{AB}) is given as,

$$T_{AB} = T_o + \eta \Delta T_{sz} \tag{4.25}$$

The average rise in the temperature at primary shear zone (ΔT_{sz}) is given by Eq.(4.26) where, dF_s is the shearing force, V_s is the shear speed, ρ is the density of the material, V_r is the instantaneous cutting speed, dw is the width of cut and C_p is the specific heat capacity of the work material. The temperature factor η accounts for the part of total shear energy appearing as sensible heat. In this analysis, the value of η is considered as 0.9.

$$\Delta T_{sz} = \frac{(1-\beta) dF_s\, V_s}{\rho\, V_r\, t_c\, dw\, C_p} \tag{4.26}$$

The portion of the heat conducted (β) to the workpiece from the shear zone varies for different ranges of ($R_T \tan\phi$) as follows.

$$\beta = 0.5 - 0.35 \log_{10}(R_T \tan\phi) \text{ for } 0.04 \leq R_T \tan\phi \leq 10$$
$$\beta = 0.3 - 0.15 \log_{10}(R_T \tan\phi) \text{ for } R_T \tan\phi > 10 \tag{4.27}$$

The non-dimensional thermal parameter can be calculated as,

$$R_T = \frac{\rho V_r t_o\, C_p}{K} \tag{4.28}$$

Where, K is the thermal conductivity of the material and t_o is the uncut chip thickness. The uncut chip thickness can be calculated for inner and outer cutting edges as shown in Figure 4.6. The shear velocity (V_s) can be determined by using Eq.(4.29)

$$V_s = \frac{\cos\alpha_e}{\sin(\phi - \alpha_e)} \tag{4.29}$$

The equivalent shear strain (ε_{AB}) and the equivalent shear strain rate ($\dot{\varepsilon}_{AB}$) at AB is calculated using von Mises criterion.

$$\varepsilon_{AB} = \frac{\gamma_{AB}}{\sqrt{3}} \tag{4.30}$$

$$\dot{\varepsilon}_{AB} = \frac{\dot{\gamma}_{AB}}{\sqrt{3}} \tag{4.31}$$

The shear strain (γ_{AB}) at PSZ is given by

$$\gamma_{AB} = \frac{\cos \alpha_e}{2 \sin \phi \cos(\phi - \alpha_e)} \tag{4.32}$$

Whereas, the average shear strain rate ($\dot{\gamma}_{AB}$) at PSZ is given as

$$\dot{\gamma}_{AB} = \frac{C_o V_s}{l_{AB}} \tag{4.33}$$

Considering the stress boundary at B (Figure 4.8), the normal stress (σ'_N) at B is calculated using Eq.(4.34) which is modified for J-C material model.

$$\sigma'_N = k_{AB} \left(1 + \frac{\pi}{2} - 2\alpha - 2C_o n_{eq}\right) \tag{4.34}$$

Whereas, the normal stress (σ_N) at tool-chip interface is calculated as,

$$\sigma_N = \frac{dN_c}{hdw} \tag{4.35}$$

The shear stress at tool-chip interface is calculated as

$$\tau_{int} = \frac{dF_f}{hdw} \tag{4.36}$$

The plastic deformation at the secondary shear zone is influenced by the secondary shear zone thickness (Δs_2) and the too-chip contact length (h). The shear strain rate at tool chip-interface is given as,

$$\dot{\varepsilon}_{int} = \frac{\dot{\gamma}_{int}}{\sqrt{3}} = \frac{1}{\sqrt{3}} \frac{V_c}{\delta t_c} \tag{4.37}$$

The chip speed (V_c) and the chip thickness (t_c) are calculated using Eq.(4.38) and (4.39) respectively.

$$V_c = \frac{V_r \sin\phi}{\cos(\phi - \alpha_e)} \tag{4.38}$$

$$t_c = \frac{t_o \cos(\phi - \alpha_e)}{\sin\phi} \tag{4.39}$$

Whereas, the equivalent shear strain at the tool-chip interface is,

$$\varepsilon_{int} = \frac{\gamma_{int}}{\sqrt{3}} = \frac{2\gamma_{AB} + 0.5\gamma_M}{\sqrt{3}} \tag{4.40}$$

Where, $\gamma_M = \frac{h}{\delta t_c}$ and γ_{AB} can be calculated using Eq.(4.32).

The tool-chip contact length (h) is calculated as,

$$h = \frac{t_o \sin\theta}{\cos\lambda \ \sin\emptyset}\left(1 + \frac{C_o n_{eq}}{3\left(1 + 2\left(\frac{\pi}{4} - \phi\right) - C_o n_{eq}\right)}\right) \tag{4.41}$$

In Eq.(4.41), the strain hardening constant (n_{eq}) is modified for the J-C model as suggested by Lalwani et al. [53] in Eq.(4.42).

$$n_{eq} = \frac{nB\varepsilon_{AB}^{n}}{A + B\varepsilon_{AB}^{n}} \tag{4.42}$$

The angle between resultant of cutting and thrust force (dR_c) and shear plane is,

$$\theta = \tan^{-1}(1 + 2\left(\frac{\pi}{4} - \phi\right) - C_o n_{eq}) \tag{4.43}$$

The friction angle (λ) between the normal force (dN_c) and resultant force (dR_c) at tool-chip interface is,

$$\lambda = \theta - \phi + \alpha_e \tag{4.44}$$

The average temperature at tool-chip interface is,

$$T_{int} = T_o + \Delta T_{sz} + \psi \Delta T_M \tag{4.45}$$

Where, the temperature factor ψ is 0.9 and the maximum rise in temperature ΔT_M is calculated using Eq.(4.46) as suggested by Boothroyd [54].

$$\log_{10}\left(\frac{\Delta T_M}{\Delta T_C}\right) = 0.06 - 0.195\,\delta\sqrt{\frac{R_T t_c}{t_o}} + 0.5\log_{10}\left(\frac{R_T t_c}{h}\right) \tag{4.46}$$

The average temperature rise in the chip is,

$$\Delta T_C = \frac{dF_f V_c}{\rho V t_c\, dw\, C_p} \tag{4.47}$$

Once the equivalent shear strain, the equivalent shear strain-rate and temperature at the tool-chip interface is known, the flow stress at SSZ can be calculated as,

$$k_{chip} = \frac{1}{\sqrt{3}}(A + B\varepsilon_{AB}^{n})(1 + Cln\frac{\dot{\varepsilon}_{AB}}{\dot{\varepsilon_o}})(1 - \left[\frac{T_{AB} - T_o}{T_m - T_o}\right]^{m}) \tag{4.48}$$

Once the value of $(dF_c)_s$ is obtained, the corresponding flow stress at PSZ (k_{AB}) was saved for the further use.

4.3.2 Prediction of $(dF_c)_p$ and $(dF_t)_p$

The next step is to determine ploughing forces. The ploughing components are determined using slip-line model proposed by Waldorf et al. [55] as shown in Figure 4.10. The ploughing component in cutting and feed direction are determined by the Eq.(4.49) and Eq.(4.50) respectively.

$$(dF_c)_p = k_{AB} dw[cos(2\eta_n)\, cos(\phi - \gamma_n + \eta_n) + (1 + 2\theta_n + \gamma_n + sin(2\eta_n))sin(\phi - \gamma_n + \eta_n)]CA \tag{4.49}$$

$$(dF_t)_p = k_{AB} dw[(1 + 2\theta_n + \gamma_n + \sin(2\eta_n))\cos(\phi - \gamma_n + \eta_n) - \cos(2\eta_n)\sin(\phi - \gamma_n + \eta_n)]CA \tag{4.50}$$

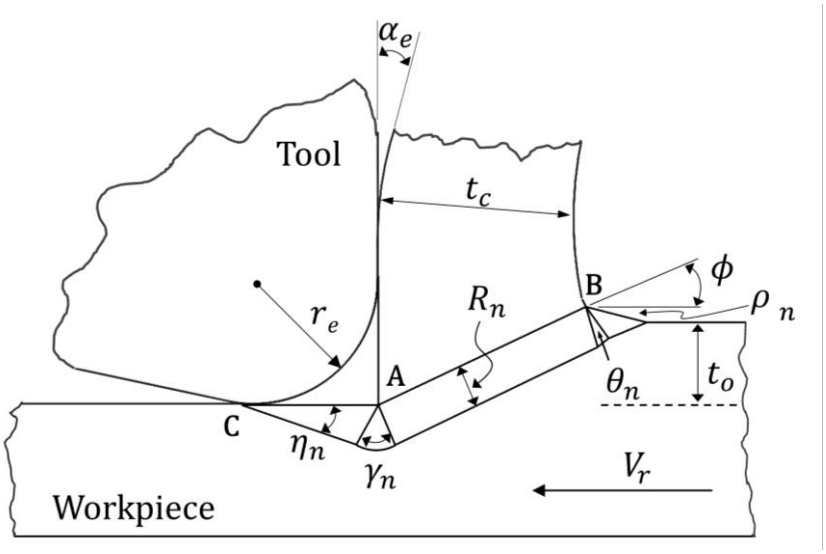

Figure 4.10 Slip-line model for ploughing [55]

The parameters are calculated as follows,

$$\eta_n = 0.5 \cos^{-1} \mu_{w-t} \tag{4.51}$$

Where, μ_{w-t} is the tool-workpiece friction co-efficient. Its value varies from 0.8 to 0.4 in the velocity range of 1 to 20 m/min as experimentally determined by Zemzemi et al [56]. In this analysis, an average value of 0.6 is used for the calculations.

$$\gamma_n = \eta_n + \phi - \sin^{-1}\left(\sqrt{2}\ \sin\rho_n \sin\eta_n\right) \tag{4.52}$$

$$\theta_n = \frac{\pi}{4} - \rho_n - \phi \tag{4.53}$$

Where, ρ_n is prow angle and assumed as 1^o for this analysis.

$$CA = \frac{R_n}{\sin\eta_n} \tag{4.54}$$

Where, R_n is determined by solving the implicit Eq.(4.55).

$$R_n = \sin\eta_n \sqrt{\left(r_e \tan\left(\frac{\pi}{4} + \frac{\alpha_e}{2}\right) + \frac{\sqrt{2}\, R_n \cos\rho_n}{\tan\left(\frac{\pi}{2} + \alpha_e\right)}\right)^2 + 2[R_n \sin\rho_n]^2} \tag{4.55}$$

The above mentioned steps were performed till the complete drill radius is covered. The total drilling forces calculated by summarizing the elemental forces using Eqs.(4.5)-(4.10).

4.4 Experimental validation

The experiments were conducted in two parts. In the first set of experiments, the predictive model was tested for the effects of micro and macro geometry in addition to varying feed rate on the thrust force. Whereas, the effect of variation of cutting speed on drilling forces along the cutting edges was verified in the second set of experiments.

4.4.1 First set of the experiments

Four nose grind designs with 8 mm diameter were selected for the first part of the study as listed in Table 4.2. The drilling parameters such as feed rate (f), the average cutting edge radius (r_e) and drill macro geometry type used for drilling experiments are summarized in Table 4.3. The cutting edge radii were measured using Alicona InfiniteFocus at three points on inner and outer cutting edge each as depicted in Figure 4.11.

Table 4.2 Details of drill geometries

Drill type	φ_i	φ_o	c_p	Bearing pad (θ_1, θ_2)
A	15	20	D/2	G (55^o,165^o)
B	20	30	D/2	G (55^o,165^o)
C	5	40	D/2	G (55^o,165^o)
D	10	40	D/3	G (55^o,165^o)

The cutting edge radius for fresh SLDs is found to be in the range of 5 to 8 μm. However, sharp drill cutting edges are susceptible to chipping during engagement due to high hardness of Inconel-718 as discussed in Chapter 3. The cutting edges were honed to $r_e = 20 \pm 3\ \mu m$ and $50 \pm 2\ \mu m$ on both the cutting edges to study the effect cutting edge radius on the drilling thrust force.

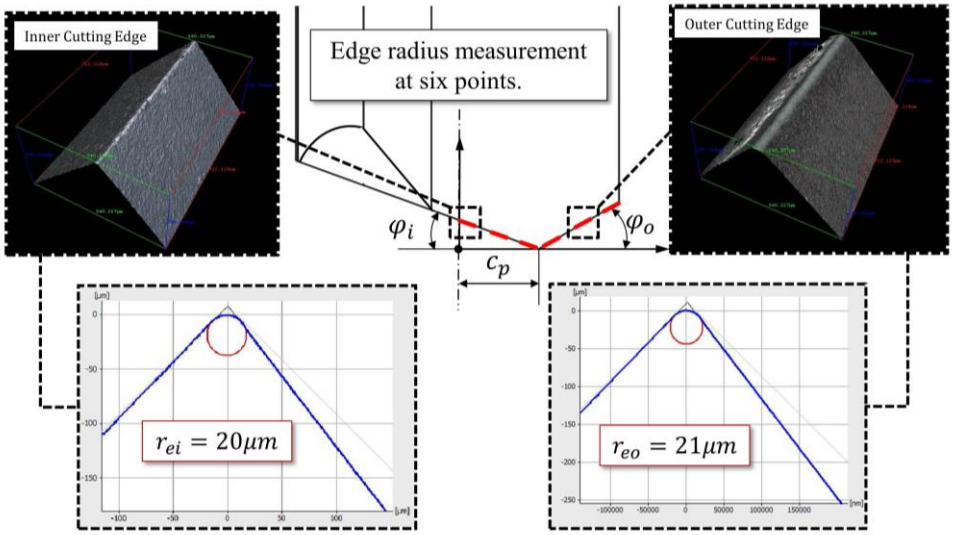

Figure 4.11 Sample measurements of cutting edge radii at inner and outer cutting edges for the honed drill.

Table 4.3 Drilling parameters for the first set of experiments

Test No.	Drill Type	$f\,(\mu m/rev)$	$r_e\ (\mu m)$
1	A	20	20
2	B	20	20
3	C	20	20
4	D	20	20
5	B	30	20
6	B	10	20
7	B	20	50
8	B	20	8

The experimental setup for the first set of experiments is depicted in Figure 4.12. Two repetitions of the drilling tests as listed in Table 4.3 were conducted at the fix RPM 800.

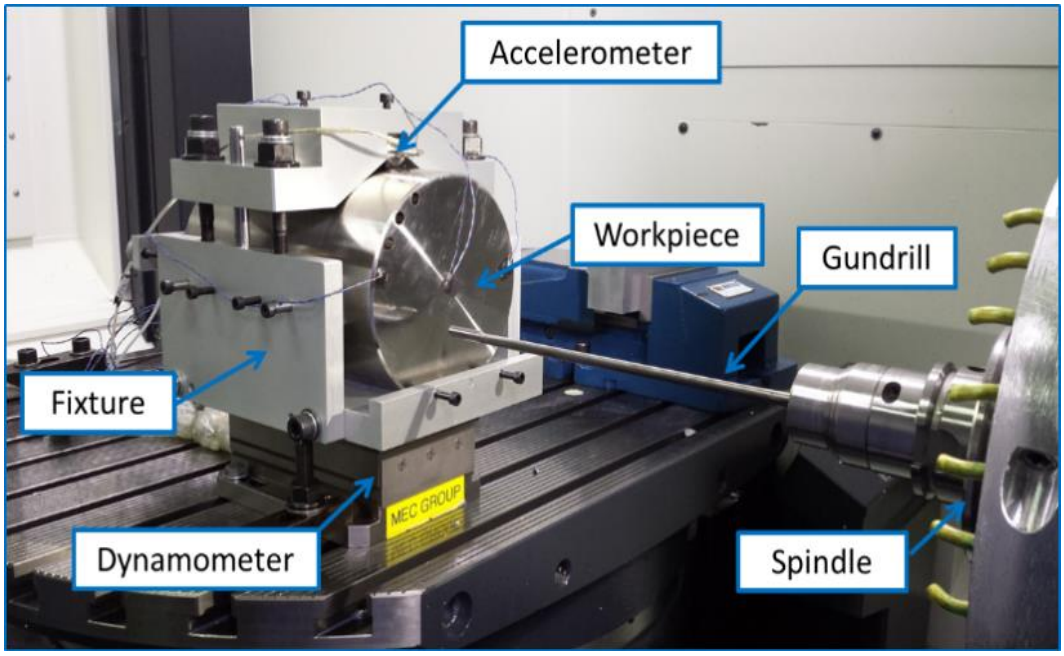

Figure 4.12 Setup for the first set of experiments

4.4.2 Second set of the experiments

The second part of the study was carried out using a different experimental setup as shown in Figure 4.13. A ring of 1 mm thickness and 20 mm outer diameter was mounted on the spindle. A short SLD was mounted on the dynamometer with eccentricity. The eccentricity can be varied to change the location of cutting edge in contact with the workpiece. The tests were conducted at four cutting speed values as 2.5, 7.5, 12.5 and 17.5 m/min which resemble with the cutting speed variation on the single-lip drill cutting edges at the drill radius of 0.5, 1.5, 2.5 and 3.5 mm respectively. The cutting speeds were achieved by changing the spindle speeds. Two repetitions were conducted with Type B drill at the feed rate of 20 $\mu m/rev$. The chip thickness

was measured using Keyence VHX-1000 Series optical microscope for which molds were prepared. A detailed procedure for the mold preparation is described in Section 5.2.2.

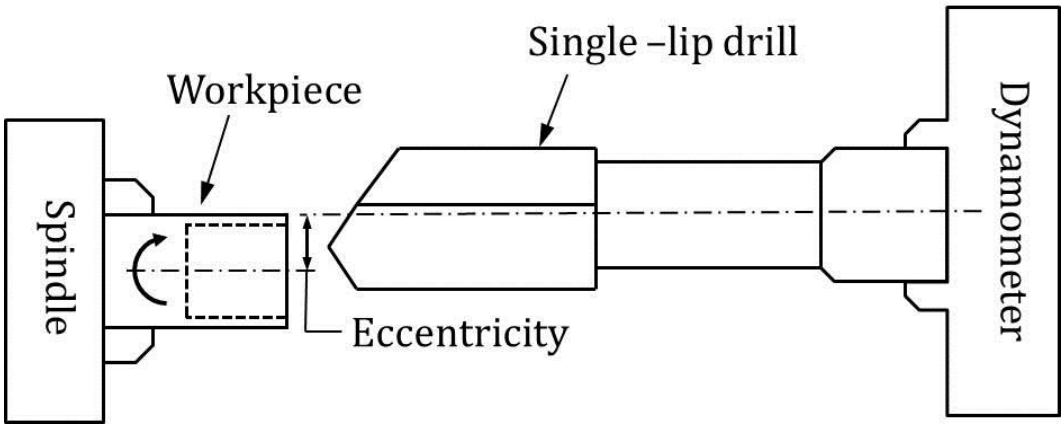

Figure 4.13 Set-up for second set of experiments

4.5 Results and Discussions

4.5.1 The effects of drill geometry on the thrust force

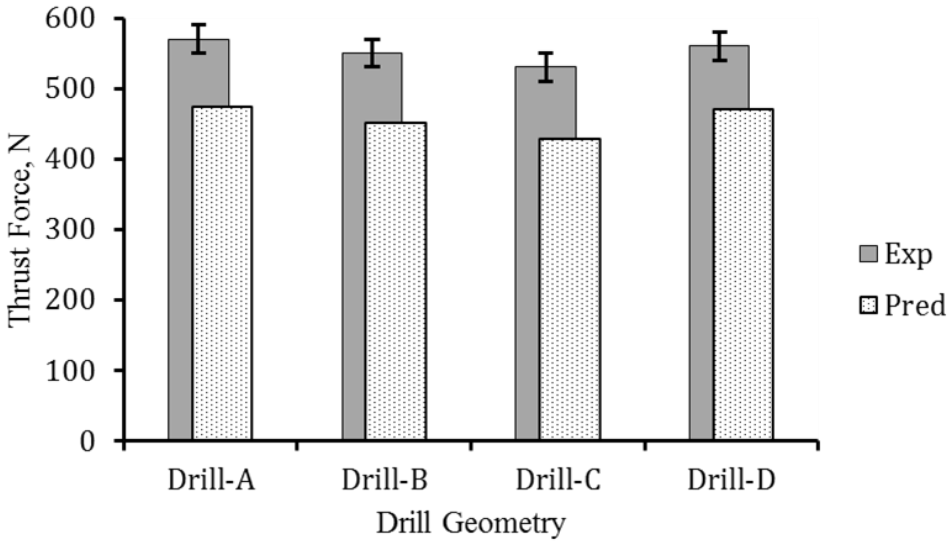

Figure 4.14 Effect of drill geometry on the thrust force
(f=20μm/rev, r_e=20 μm)

Figure 4.14 shows the variation of thrust force with respect to the drill geometry when the feed rate and cutting edge radius are kept constant.

Figure 4.14 shows the variation of thrust force with respect to the drill geometry when the feed rate and cutting edge radius are kept constant. As the outer cutting edge angle increases the thrust force decreases. As the outer cutting edge angle increases the component of F_{to} in the Z direction decreases.

4.5.2 The effect of feed rate on drilling thrust force

As the feed rate increases the thrust force increases due to increasing chip load on the cutting edge as shown in Figure 4.15.

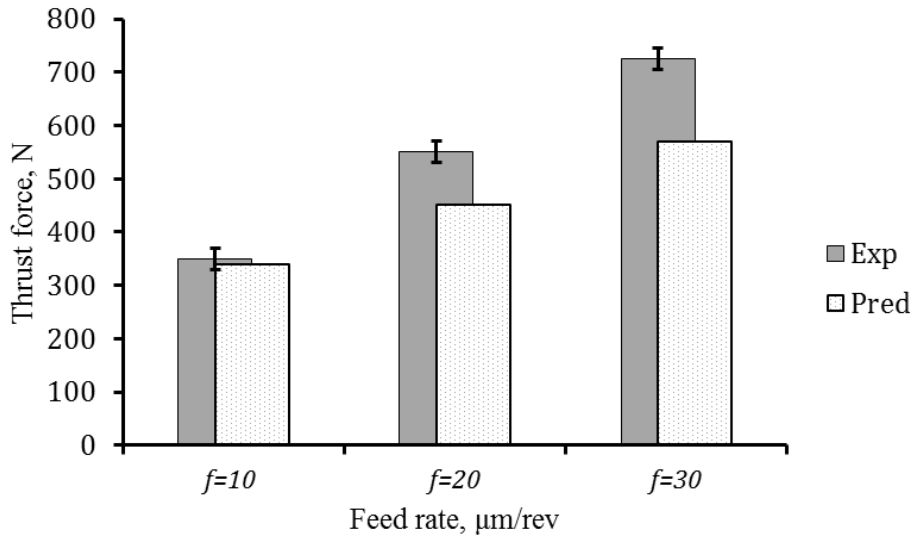

Figure 4.15 Effect of the feed rate on the drilling thrust force (r_e=20 µm, Drill-B)

It was observed that the difference between measured and predicted results also increases with increasing feed rates. It can be attributed to the frictional force generated due to long and thick chips at higher feed rates which were not considered in the predictive model. The details of this phenomenon are discussed in Chapter 5.

4.5.3 The effects of cutting edge radius on the thrust force

The thrust force increases for same feed rate ($f = 20\,\mu m$) when the cutting edge radius (r_e) increases as shown in Figure 4.16. The increase of thrust force is attributed to the increasing ploughing force due to the edge radius effect. The ratio (t_o/r_e) of uncut chip thickness to cutting edge radius changes from 2.5 to 0.4 as the cutting edge radius changes from 8 μm to 50 μm. The effective rake angle (α_e) was calculated using Eq.(4.1) and it was found to be -23.57^o for the cutting edge radius of 50 μm. The increased negative rake angle causes excessive ploughing which leads to increase in the thrust force. It was also observed that the predictive model overestimates the thrust force for negative rake angles. Similar observations were also reported by Adibi-Sedeh et al. [52].

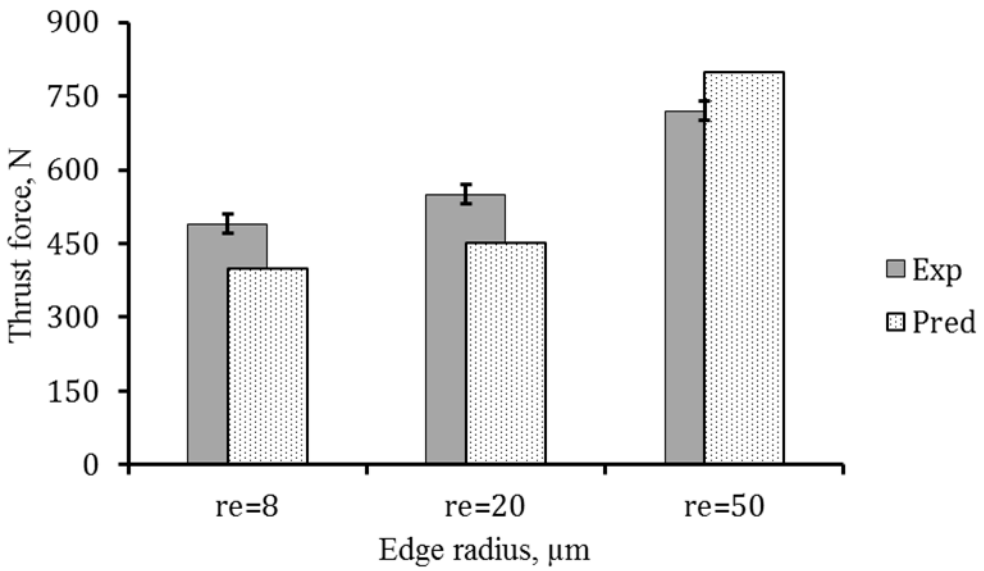

Figure 4.16 Effect of the cutting edge radius on the drilling thrust force (*f*=20µm/rev, Drill-B)

4.5.4 Force distribution on the cutting edges

The drilling forces decrease along the cutting edge as the radius increase as shown in Figure 4.17. The change in cutting forces can be attributed to the thermal softening effect. As the drill radius increases the cutting speed also increase which causes an increase in temperature at primary deformation zone.

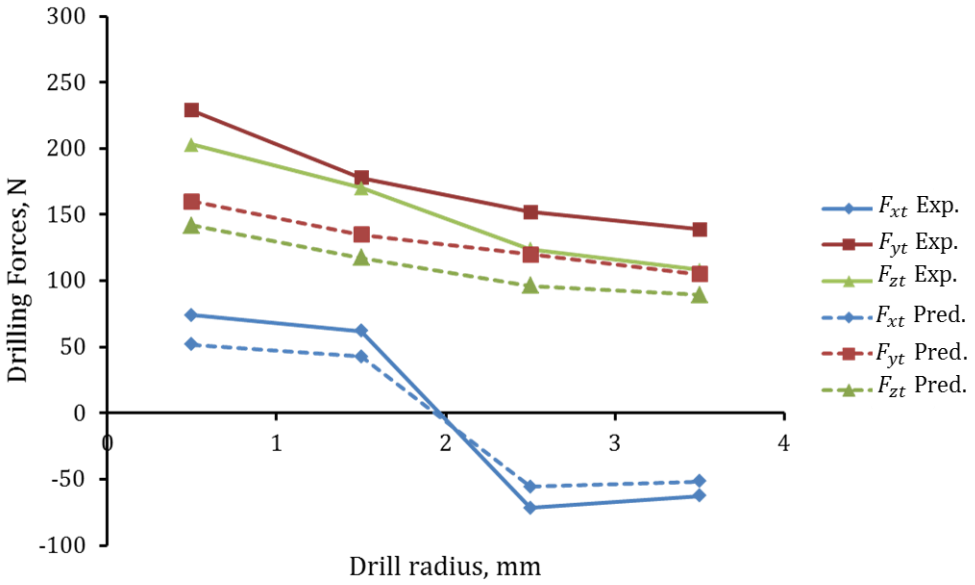

Figure 4.17 Variation in F_{xt}, F_{yt} and F_{zt} with respect to radius.

As a result, flow stress value decreases leading to decrease in the drilling forces. Moreover, the frictional coefficient is higher at lower cutting speed as reported by Zemzemi et al. [56] which also causes an increase in drilling forces at lower cutting speeds. The different between the predicted and the measured results was found to be in good agreement at higher cutting speeds as compared to the lower cutting speeds. The error can be further reduced at lower cutting speeds by modeling the tool-workpiece frictional coefficient (μ_{t-w}) as a function of cutting speed. The distribution of the drilling force along the cutting edge can be further used for optimization of bearing pads

configuration to ensure stable burnishing process. Moreover, the finding can be used in analysis of wall deformation during machining of thin walled deep holes as studied experimentally by Biermann et al.[57].

4.5.5 Variation in shear angle and chip thickness

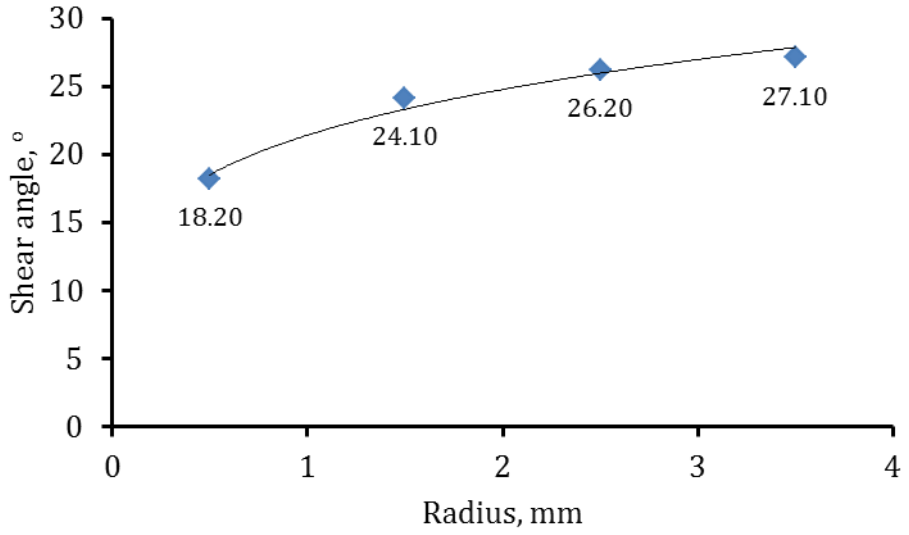

Figure 4.18 Predicted change in shear angle along drill radius

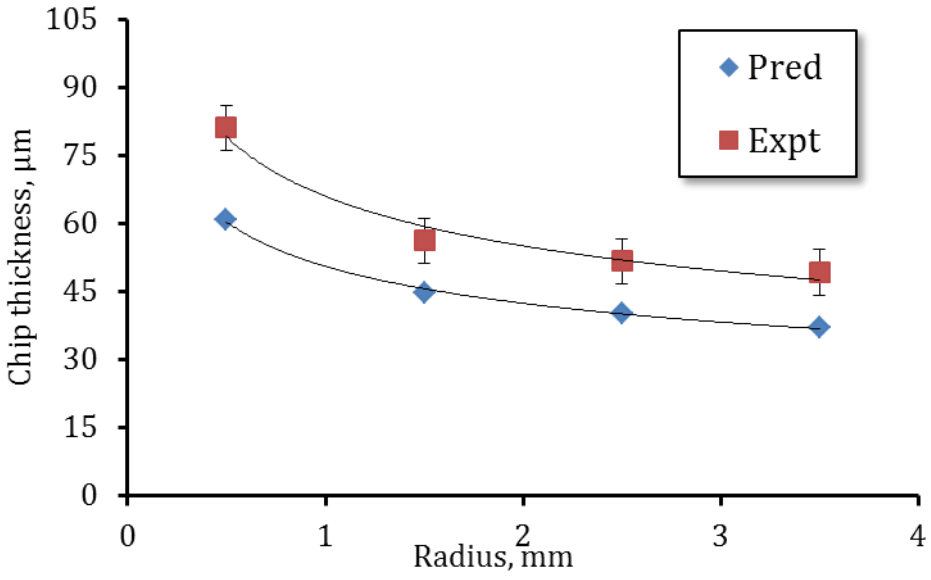

Figure 4.19 Change in chip thickness along the drill radius

The shear angle increases as the drill radius increases as depicted in Figure 4.18, as a result, the chip thickness decreases along the drill radius as shown in Figure 4.19. The average error in the predicted and experimental values was found to be less than 20 %.

4.6 Concluding Remarks

A comprehensive predictive model was developed which considers the effect of edge radius on single-lip drilling forces for Inconel-718. The effects of tool geometry, feed rate, and cutting edge radius on the drilling forces were predicted and experimentally validated. In addition, variation in the force distribution along the cutting edges was also predicted. The major findings are summarized as follows.

- Micro geometry has a higher influence on the drilling thrust force as compared to the macro drill geometry, especially at lower feed rates. The cutting mechanism is dominated by ploughing when the ratio of uncut chip thickness and cutting edge radius is below one leading to higher thrust forces.

- The drilling cutting forces are higher on the inner cutting edges as compared to the outer cutting edges which has significant implications for drill stability.

- As the cutting speed increases along the cutting edge the shear angle increase and the chip thickness decreases.

- The predicted results show good agreement with experimental results with an error less than 20%. Hence, the developed model can be used for the prediction of thrust force required in the straightness analysis.

Chapter 5: Chip Morphologies in DHD of Inconel-718

In this chapter, mechanics of chip formation in the single-lip drilling of Inconel- 718 is discussed. A novel method was introduced to observe real time chip formation using high-speed camera. The effect of tool geometry on a chip morphology is explained in addition to chip breaking mechanism. Finally, the effect of chip morphology on thrust force is quantified.

5.1 Background

A limited number of studies is available for chip formation in deep hole drilling of Inconel-718. The studies are mostly experimental in nature and report few observations based on the chip in hand. As reported earlier, Biermann et al. [24, 58] studied the single-lip drilling of Inconel-718 and chip formation using high-speed camera for 1.5 and 2 mm diameter holes. They observed that Inconel-718 chips are difficult to break and chip curling plays a major role in chip breaking. However, these studies were conducted at smaller diameter with microscopic feed rates hence the results may not apply to the drills with a bigger diameter such as 8 mm. Hence, in this study, a comprehensive set of experiments was performed to understand the effect of drill geometry on chip morphology and chip breaking. Moreover, it was reported in Chapter 4 that the chip morphology at higher cutting feed rates affects the drilling thrust force which needs to be quantified.

The chip morphology is governed by the factors listed in Figure 5.1. Moreover, the factors are interlinked and it is hard to separate their effect on

the chip morphology. Understanding of interdependence of these factors is important for chip control in deep hole drilling of Inconel-718.

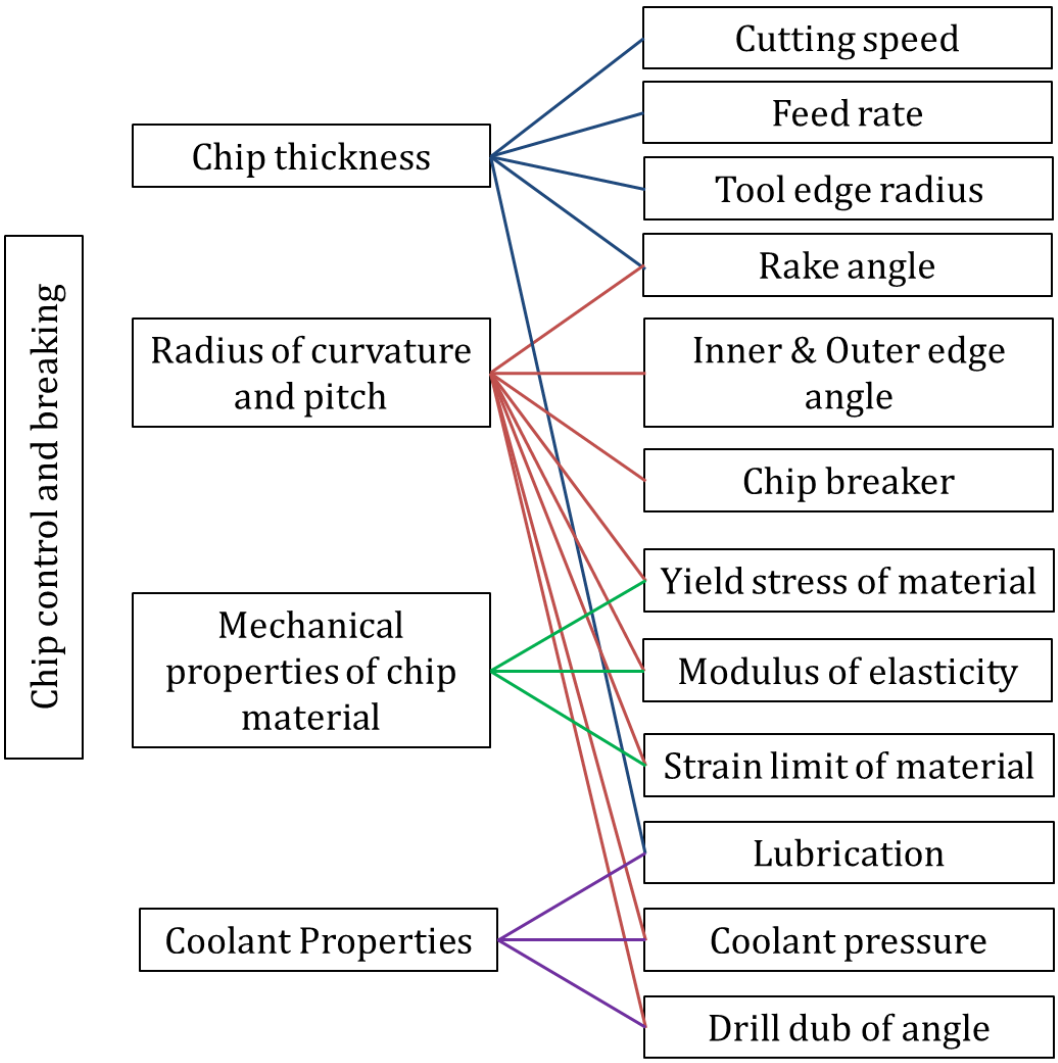

Figure 5.1 Relation between different factors and chip morphology in single-lip deep hole drilling.

5.2 Experimental Study

5.2.1 Drilling parameters

To understand the effect of various parameters on the chip morphology a comprehensive set of experiments was conducted. Three nose grind designs with increasing outer cutting edge (φ_o) angle and one drill with D/3 apex

location were selected. The details of the drill geometries are given in Table 5.1. To avoid chipping, the cutting edge radii for all the drills were honed to 20 μm.

Table 5.1 Drill geometries used for chip morphology study

Drill	$\varphi_i(^o)$	$\varphi_o(^o)$	c_p(mm)	D (mm)
A	15	20	2	8
B	20	30	2	
C	5	40	2	
D	10	40	1.33	

The experiments were conducted on DMU 80P duoBLOCK® five axis machining center with maximum coolant pressure of 4 MPa. The tests were conducted at three levels of feed rate (f) as 10, 20 and 30 $\mu m/rev$. The spindle RPM was set as 800 for all the drilling conditions. The forces were recorded using Kistler Type-9257B three-component dynamometer and LabVIEW software. The pilot holes were machined based on guidelines described in Chapter 3.

Table 5.2 Mechanical properties of Inconel-718 used for chip morphology study

Yield Point (MPa)	Tensile Strength (MPa)	Elongation (%)	Area Reduction (%)	Hardness (HRC)
1058	1327.5	10	20	42-45

The mechanical properties of the Inconel-718 workpiece are listed in Table 5.2.

5.2.2 Chip characterization

The spiral chips were characterized based on chip diameter (d_c), length (l_c), pitch (p_c) and thickness (t_c) whereas only chip thickness was used for snarled and elemental chips because of their irregular shape.

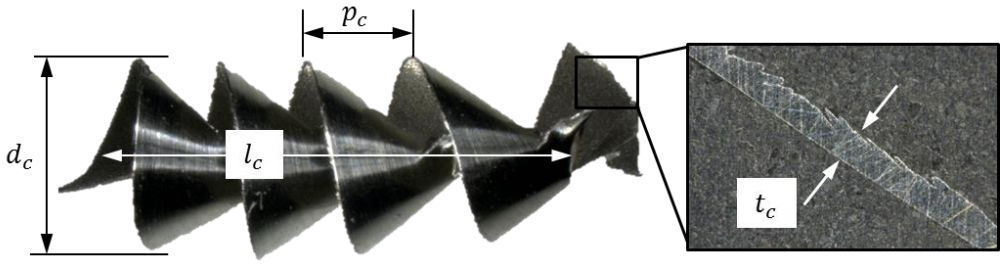

Figure 5.2 Parameters for chip characterization

The measurements were performed on 10 randomly selected chips for each experimental condition. Epoxy molds were prepared for the chip thickness measurements. Method for mold preparation is depicted in Figure 5.3 where initially a chip is placed in the epoxy mold and the mold was polished till the half diameter of the chip is reached. Keyence VHX-1000Series microscope was used for the measurements.

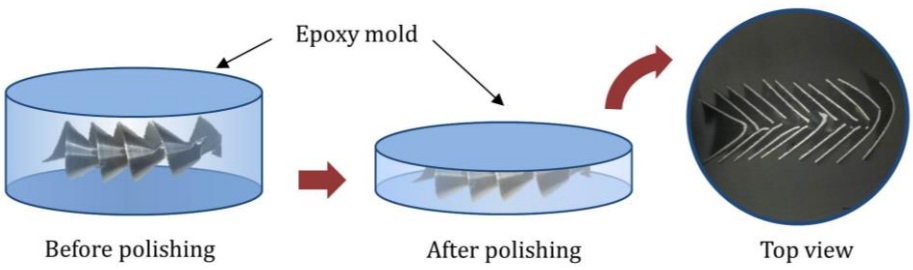

Figure 5.3 Mold preparation for chip thickness measurements

5.3 Results and Discussions

The chips generated during single-lip deep hole drilling in Inconel-718 are shown in Figure 5.5. The chips were classified based on the simplified ISO chip classification [59] as shown in Figure 5.4.

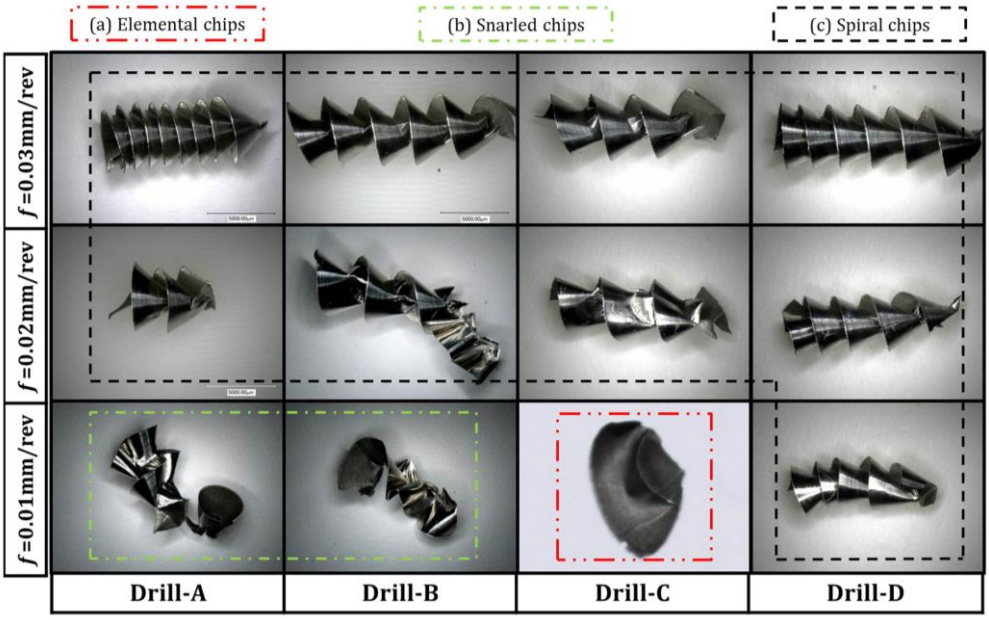

Figure 5.4 Classification of chips for deep hole drilling in Inconel-718: (a) Elemental chips, (b) snarled chips and (c) spiral chips

The chips generated during deep hole drilling in Inconel-718 can be divided into three main categories:

1. Spiral chips
2. Snarled chips
3. Elemental Chips

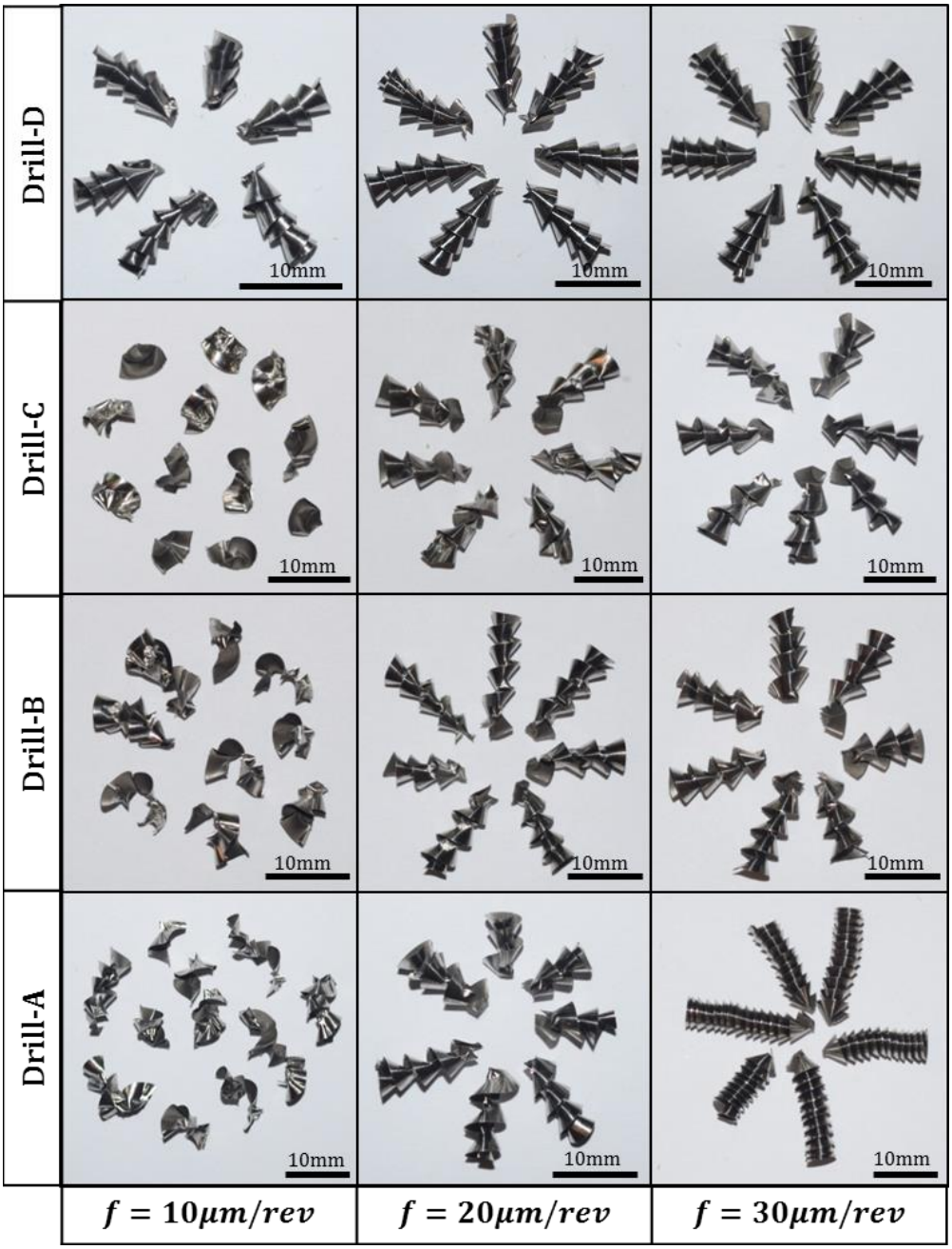

Figure 5.5 Chip morphologies in single-lip deep hole drilling of Inconel-718

The chips observed in the present experiments were dominated by the spiral chips unlike the chips reported by Biermann et al. [24, 58]. The mechanics of chip formation and reasons for the variation in chip morphologies are explained in the next sections.

5.4 Mechanics of Chip Formation

In the following sections mechanism of chip formation and chip breaking for elemental, snarled and spiral chips are discussed.

5.4.1 Elemental and snarled chip formation

A novel experimental set-up was used to visualize the real time chip formation. Inconel-718 bar of 8 mm diameter was fixed on the spindle while 8 mm diameter drill was fixed on the machine table. An acrylic tube with 8 mm internal diameter and 2 mm thickness was used to cover the drill and the Inconel-718 workpiece. High-speed camera was used to record the chip formation. The schematic of the set-up is shown in Figure 5.6.

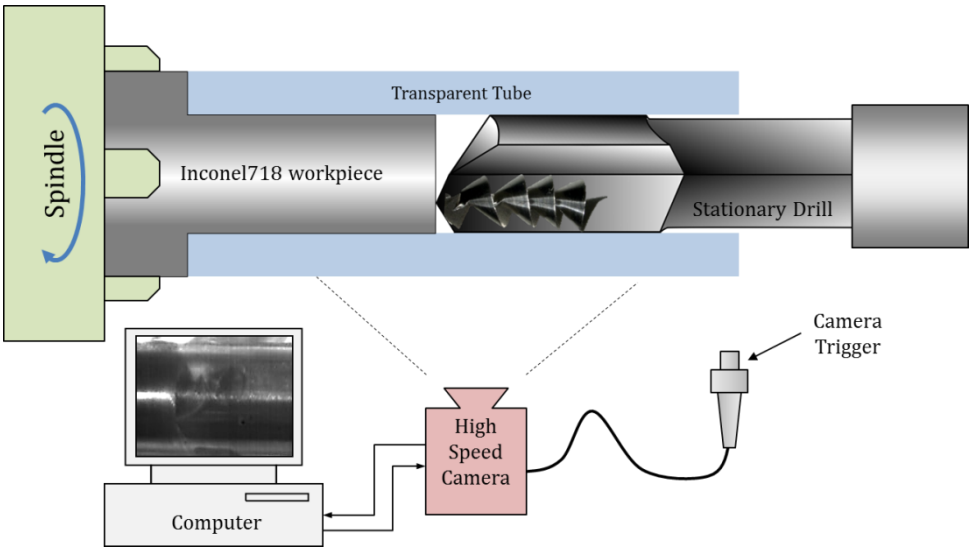

Figure 5.6 Visualization of chip formation using high-speed camera

The experiments were conducted without any coolant supply to maintain a high level of visibility for high-speed photography. However, pressurized air was circulated during the experiments to simulate the effect of coolant pressure. Drill geometry B ($\varphi_i = 20^o, \varphi_o = 30^o, c_p = 2$ mm) was used with

feed rate of 10 $\mu m/rev$ at 400 RPM. The average cutting edge radius for drill was $7.5 \pm 2\mu m$. It was observed that the elemental and snarled chip formation follows three steps.

5.4.1.1 Step 1: Chip formation starts

The chip formation starts as the apex point of the drill engages with workpiece material. During the engagement, the cutting edges are not in full contact with the workpiece. The high-speed video was recorded once the engagement had completed. Initially, the chip was not visible in the image as the view was obstructed by the unique profile of the hole bottom.

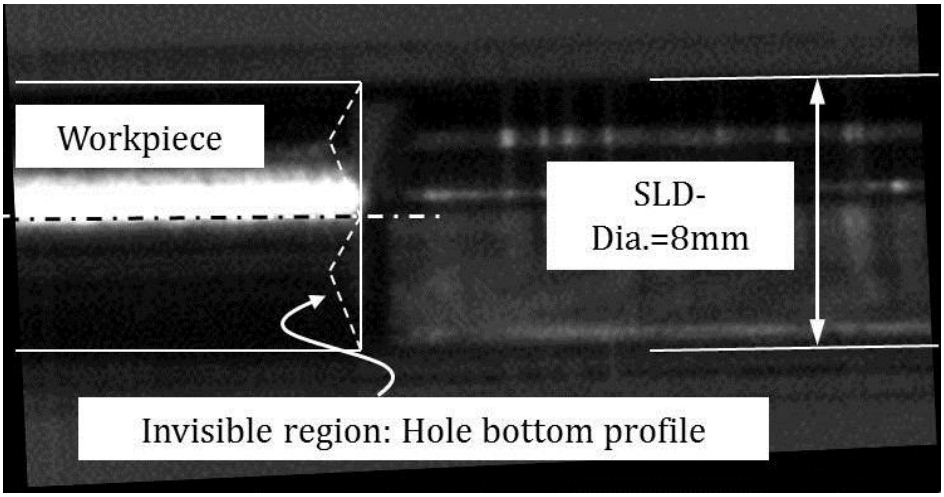

Figure 5.7 Step 1: Chip formation starts

5.4.1.2 Step 2: Separation of chip from tool rake surface

As the chip continues to form, chip separates from the rake face and up-curling start due to internal stress induced on the both sides of the chips. In general, the up-curling is hard to achieve without any chip breakers [60] however, in the single-lip drilling the up-curling at the low feed rate is caused by ploughing phenomena. At lower cutting feed rate the ploughing action

dominated the chip formation as the cutting edge radius is comparable to the uncut chip thickness.

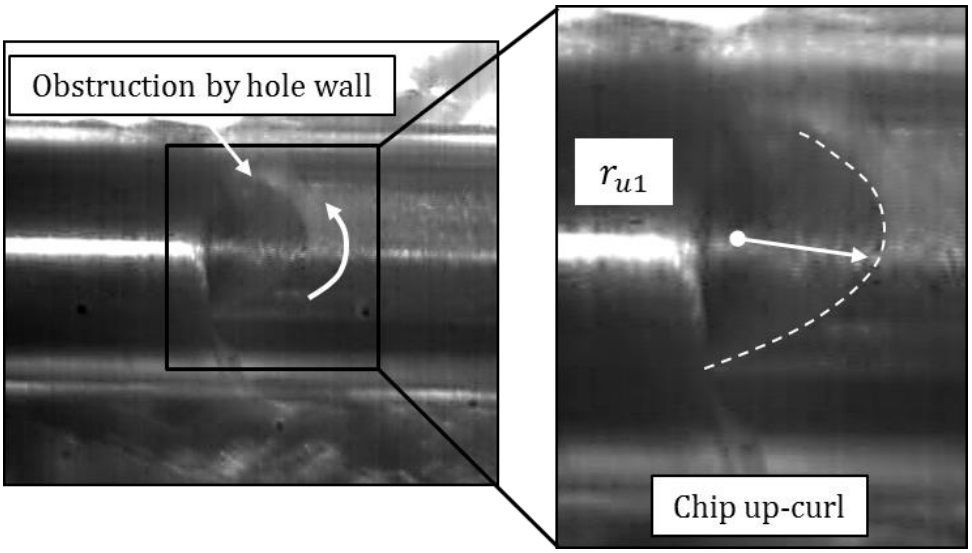

Figure 5.8 Step 2: Up-curling of the chip

The chip experiences very high compressive load on the free side of the chips as the effective rake angle becomes negative in some cases Figure 5.9(a). As a result, chip thickness ratio was higher for low feed rates as shown in Figure 5.11. The up-curl radius for the chip before reaching the hole wall is r_{u1} as shown in Figure 5.8. The tool-chip separation due to chip up-curling is visible in Figure 5.9(b).

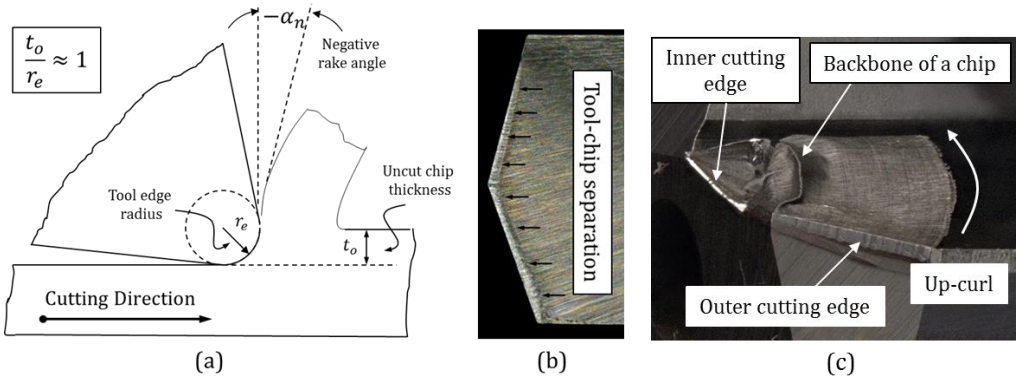

Figure 5.9 (a) Negative rake angle at lower feed rates (b)Tool-chip separation region for Drill-A at *f=10 µm/rev* (c) Backbone of a chip

The cutting edge angles also play an important role in defining the chip up-curling. The chip flow direction at the inner cutting edge and the outer cutting edge differ significantly at apex point forming a ridge which is called the backbone of the chip as shown in Figure 5.9(c). It was observed that the chip up-curling is smaller if the difference between the inner and outer cutting angle is higher.

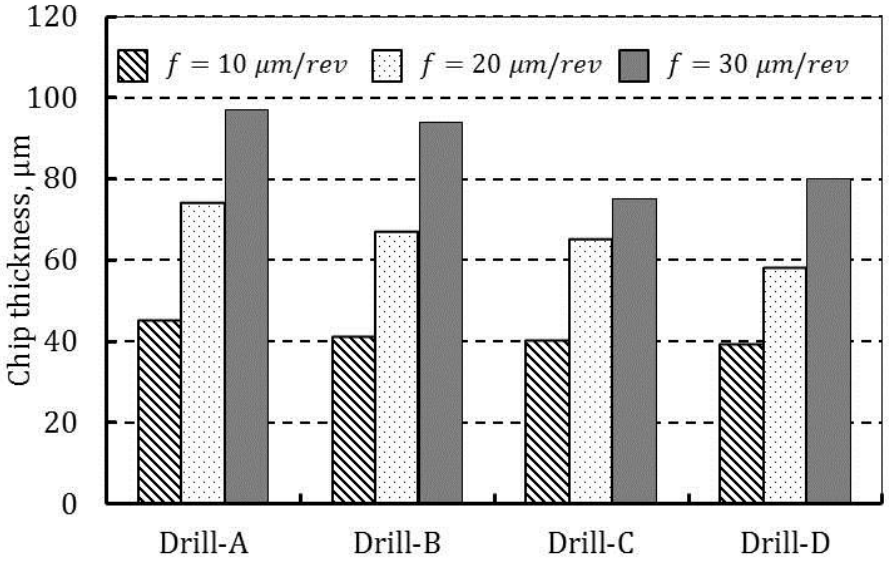

Figure 5.10 Measured chip thickness

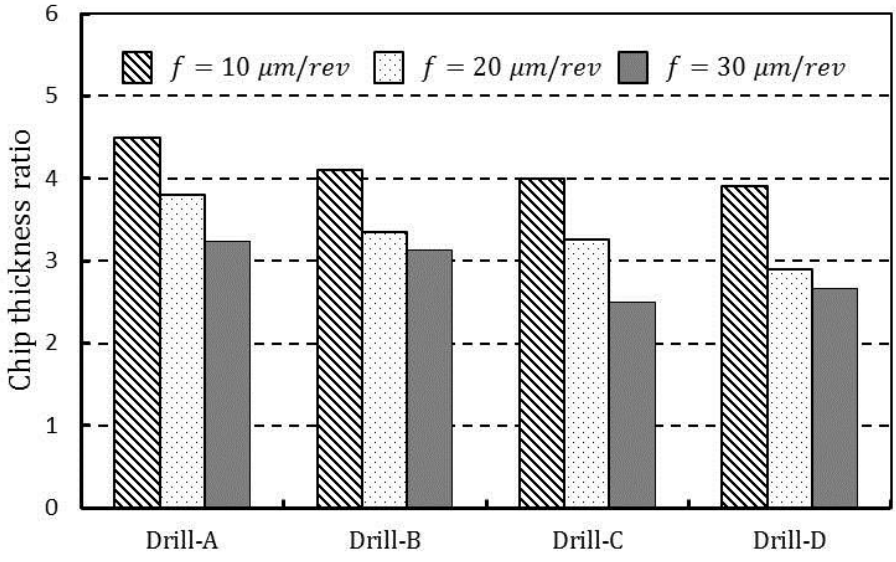

Figure 5.11 Measured chip thickness ratio

The difference in chip morphologies can be observed for chips generated by Drill-A and Drill-B which have more up-curling as compared to the chips generated by Drill-C at $f = 10\mu m/rev$ as it can be seen in Figure 5.4. However, there was no adiabatic shear band formation as reported by Pawade et al. [61] which can be attributed to the lower cutting speeds used while drilling.

5.4.1.3 Step 3: Elemental chip breaking

According to Nakayama et al. [62] the chip breaking starts when the maximum strain (ε_{max}) on the free side of the chip crosses a threshold strain (ε_{crit}) which depends on the chip up-curl radius . Initially, the chip has up-curl radius of r_{u1}, however, the up-curl radius increases and reaches r_{u2} when chip is obstructed before reaching the critical stain threshold. The increase in strain on the free side of the chip is given by,

$$\Delta\varepsilon_{chip} = \frac{t_c}{2}\left(\frac{1}{r_{u1}} - \frac{1}{r_{u2}}\right) \tag{5.1}$$

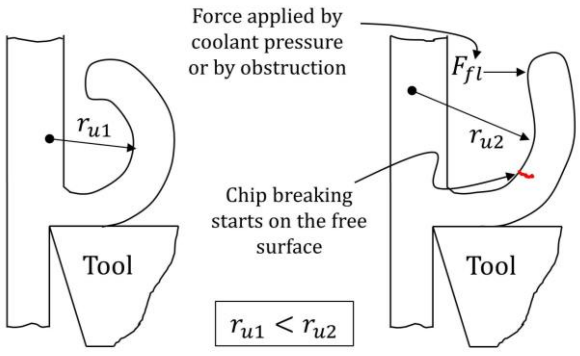

Figure 5.12 Increase in up-curl radius due to coolant pressure leading to chip breaking

In single-lip drilling, the obstruction can be caused either by the wall of the hole or by the coolant flow. For the current experiments, the coolant flow was not available hence the increase in the chip up-curl radius was induced due to obstruction by a wall of the hole as it can be observed in Figure 5.13.

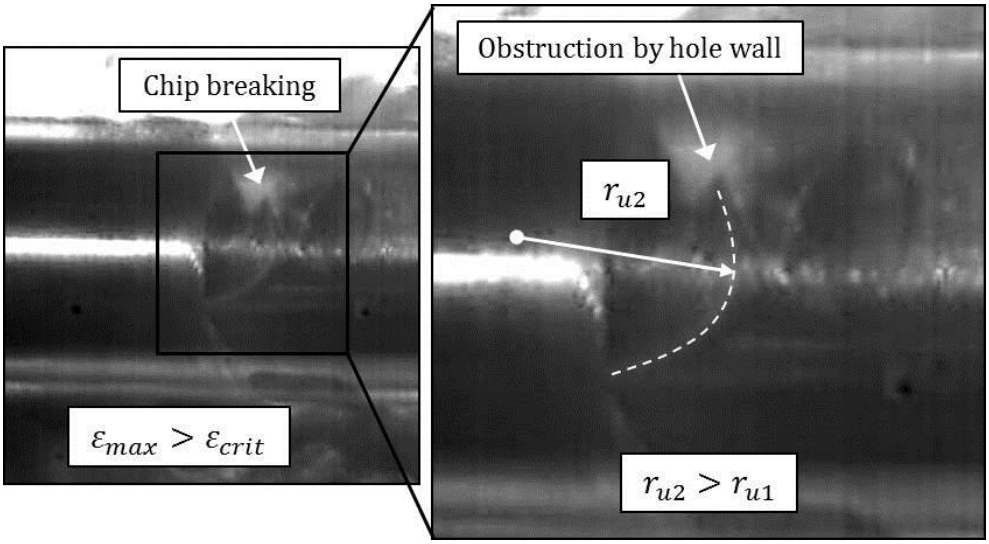

Figure 5.13 Step 3: Elemental chip breaking

As discussed earlier, the cutting edge angles also influence the up-curl radius significantly. Larger up-curl radius in case of Drill-C at lower feed rates combined with smaller chip thickness induces higher tensile strain in the chip. The additional increase in up-curl radius caused by the coolant flow was sufficient to break the chip hence the elemental chips were generated.

5.4.1.4 Snarled chip formation

Inconel-718 has very high tensile strength, moreover, it has a very high threshold for ductile failure hence higher elastic strains are needed to initiate chip breaking. In the case of Drill-A and Drill-B while drilling at lower feed rate the chip up-curl radius are smaller and the chip thickness is higher as shown in Figure 5.10. The required chip up-curl radius for reaching the

critical tensile strain cannot be induced by the applied coolant pressure hence snarled chips are generated. This was also observed during the high-speed photography experiments as shown in Figure 5.14.

The chips continue to form despite obstruction and multiple cracks can be found on the free side of the chip as shown in Figure 5.15. However, it only breaks when the surface area becomes sufficiently large to exert required force due to coolant pressure to break the chip.

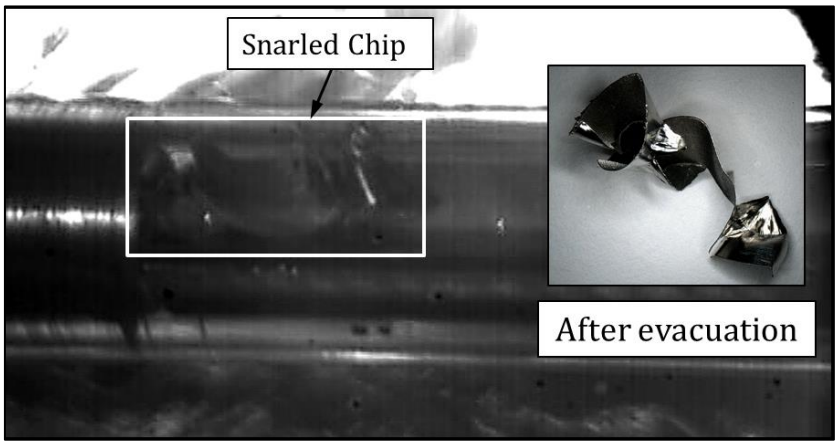

Figure 5.14 Snarled chip formation in deep hole drilling of Inconel-718

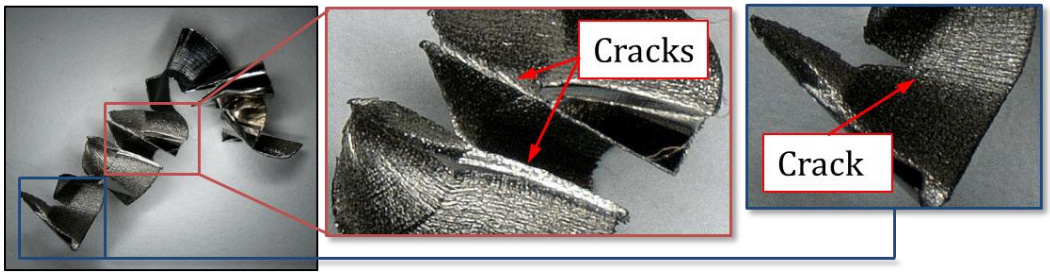

Figure 5.15 Cracks formed on the snarled chip

The elemental and snarled chips were characteristics of the drilling feed rates up to 10 $\mu m/rev$ as seen in Figure 5.5. It is important to note that there was no coolant used for the visualization experiments hence snarled chips were formed due to the lack of sufficient coolant pressure. However, at higher feed

rates the chip morphology changes and spiral chips are formed thought coolant is used.

5.4.2 Mechanism of spiral chip formation

The spiral chip formation could not be visualized using the method proposed in the previous section. After several unsuccessful attempts, it was concluded that the acrylic tube was unable to sustain higher drilling forces at higher feed rates. Moreover, the experiments were conducted without any coolant which caused excessive heat build near the cutting edge leading to melting of the tube material and making it opaque which made visualization impossible. Hence, a model was proposed based on the observations made on the drills and spiral chips in hand to explain chip formation and breaking mechanism. The spiral chip formation is divided into three steps as follows.

5.4.2.1 Step 1: Side-curling of the chip

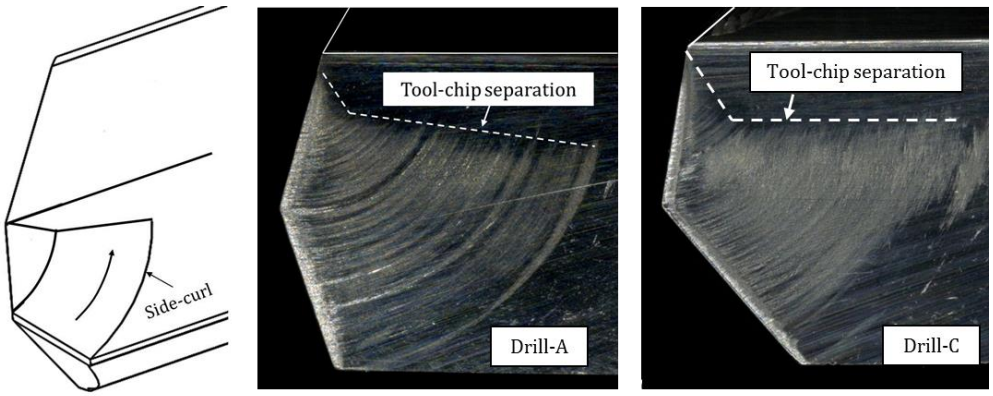

(a) (b) (c)

Figure 5.16 (a) Step I: Chip side curling (b) Chip marks and tool-chip separation line for Drill-A at *f= 30* $\mu m/rev$, (c) Chip marks and tool-chip separation line for Drill-C at *f= 30* $\mu m/rev$

The mechanics of chip formation changes as the feed rate increases. The chip up-curl is not guaranteed without the chip breaker when the uncut chip

thickness is higher than the cutting edge radius of the drill cutting edge [60]. In single-lip drilling, the chip formation starts when the drill engages with the workpiece and the chip then continues to move on the rake face as the drill is fed. Unlike the chip formation at a lower feed rate, the chip shape is dominated by the side curling and the up-curling is latent in this region. The chip continues to be in contact with the rake face until it reaches the wall of the V-flute on the drill. This is evident from the marks generated by the chip on the drill rake face which were observed on the various drill geometries as shown in Figure 5.16.

The chip flow angles on the inner and outer cutting edges change significantly however chip side curling is dominated by the chip flow angle on the outer cutting edge angle as the material flow is two times higher on the outer cutting edge.

5.4.2.2 Step 2: Up-curling of the chip

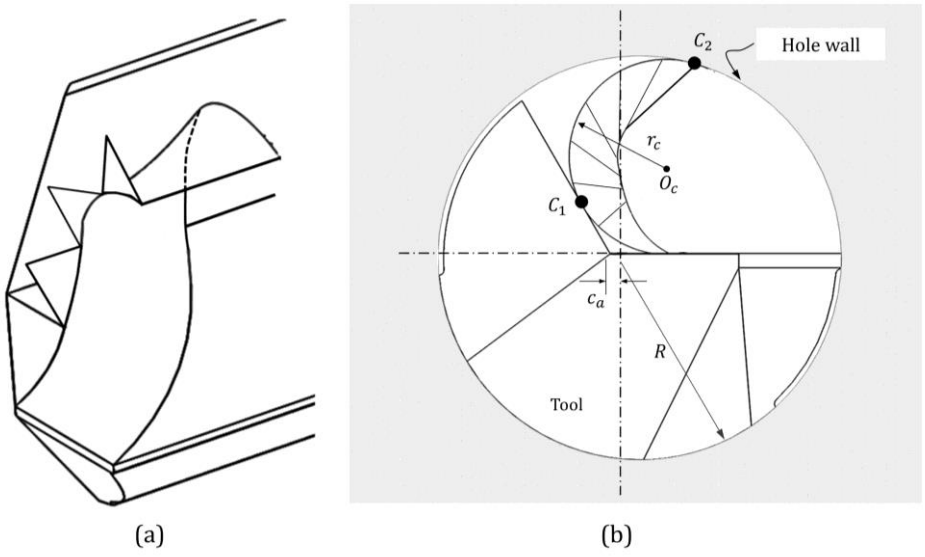

Figure 5.17 (a) Step 2: Up-curling of the chip (b) Chip up-curl due to obstruction from drill flute wall and hole wall.

The chip starts to up-curl once the chip reaches the wall of V-flute. The chip continues to curl as it comes in contact with hole wall as shown in Figure 5.17. The combined effect of side-curl and up-curl leads to spiral chip formation.

5.4.2.3 Step 3: Spiral chip formation

As the chip continues to form, it reaches the rake face of the drill and completes a loop of the spiral. The subsequent loops are formed as the chip continues to form before breaking.

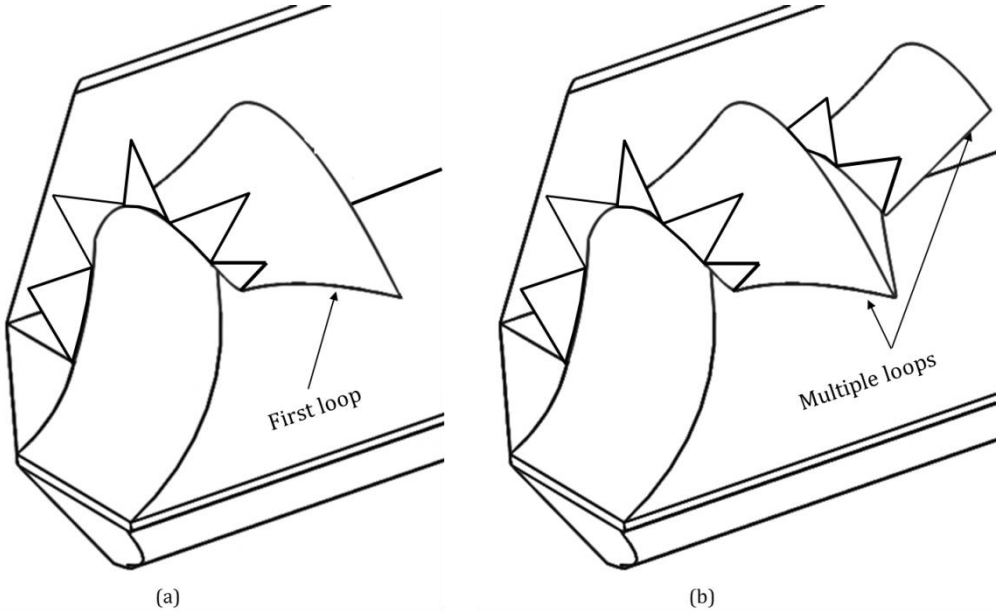

Figure 5.18 Step 3: Spiral chip formation (a) Completion of first loop of the spiral chip (b) Subsequent loop formation of the spiral chip.

The chip moves forward relative to the drill flute with the velocity vector $\boldsymbol{v_{cf}}$.

The cutting velocity for drill is given as,

$$\boldsymbol{v} = \boldsymbol{R} \times \boldsymbol{\omega} \tag{5.2}$$

Where $\boldsymbol{R}$ is the radius vector and $\boldsymbol{\omega}$ is the angular velocity of the drill.

The drill feed velocity is $\boldsymbol{v_f}$ and the absolute chip velocity with respect to workpiece is $\boldsymbol{v_{cw}}$ which is calculated using following Eq.(5.3).

$$\boldsymbol{v_{cw}} = \boldsymbol{v} - \boldsymbol{v_f} + \boldsymbol{v_{cf}} \tag{5.3}$$

For smooth removal of the chip, the angle φ_c between $\boldsymbol{v_{cw}}$ and $\boldsymbol{v_{cf}}$ should be as small as possible. The value of $\boldsymbol{v_{cw}}$ and $\boldsymbol{v_{cf}}$ is affected by chip morphology as follows.

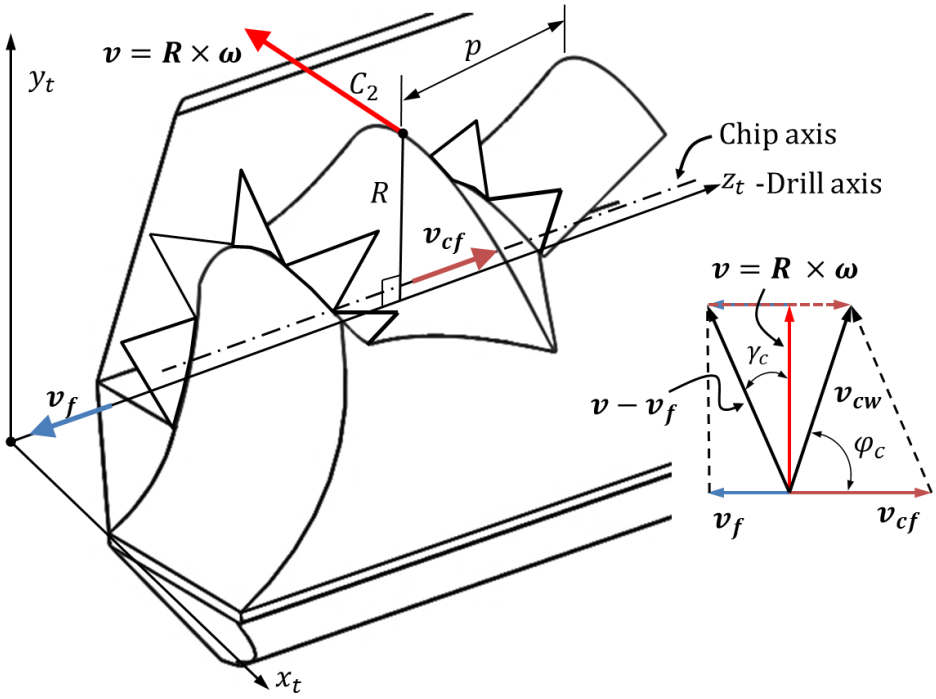

Figure 5.19 Velocity analysis of spiral chip.

The maximum possible chip radius (r_c) for the given single-lip drill can be calculated using Eq.(5.4).

$$\tan\left(\frac{\theta_t}{2}\right)\left(c_a + \sqrt{(R - r_c)^2 - {r_c}^2}\right) = r_c \tag{5.4}$$

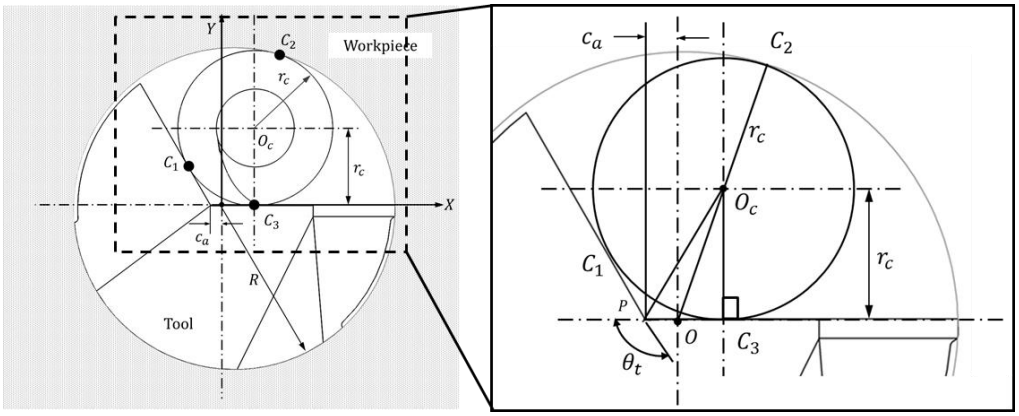

Figure 5.20 Maximum chip radius for the single-flute drill.

Where, r_c is the maximum possible spiral chip radius which can be calculated by solving the implicit Eq.(5.4) derived based on the geometrical model shown in Figure 5.20. The V-flute angle (θ_t) was 120^o and the clearance (c_a) was 0.5 mm for the drills used in this analysis. The maximum chip diameter (d_{c-max}) was found to be 3.82 mm.

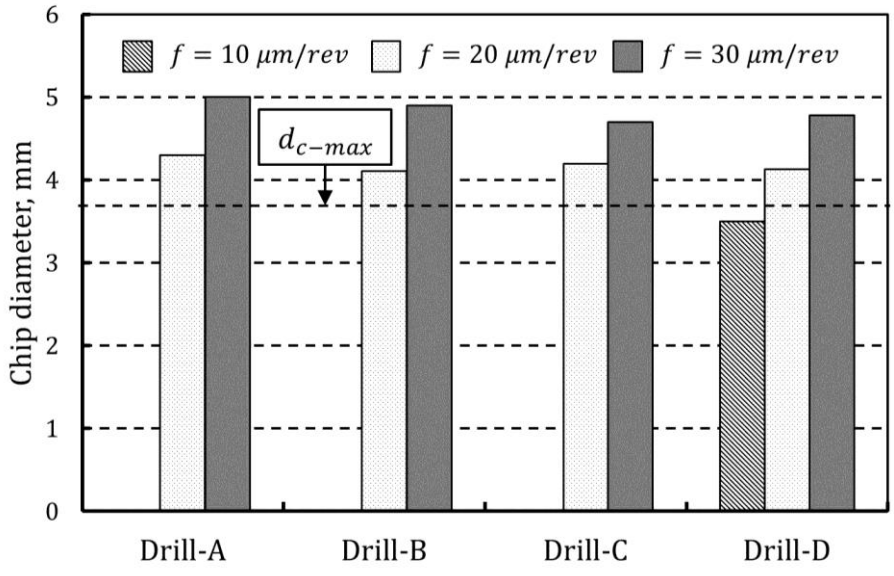

Figure 5.21 Measured chip diameter for spiral chips.

However, the measured diameters as shown in Figure 5.21 for the spiral chips exceed the calculated value for d_{c-max} which can be attributed to the elastic

recovery of the chip. It was also found that the thicker chips experienced more elastic recovery leading to bigger diameter once evacuated from the flute.

The spiral chip exerts normal forces at point C_1,C_2 and C_3 as F_{nc1}, F_{nc2} and F_{nc3} for each loop of the spiral chip due to elastic recovery inside the hole. The magnitude of these forces depends on the extend of elastic recovery which is defined by thickness of the chip. Moreover, the chip is obstructed by the corresponding frictional forces (F_{fc1}, F_{fc2} and F_{fc3}) acting at the contact points as shown in Figure 5.22.

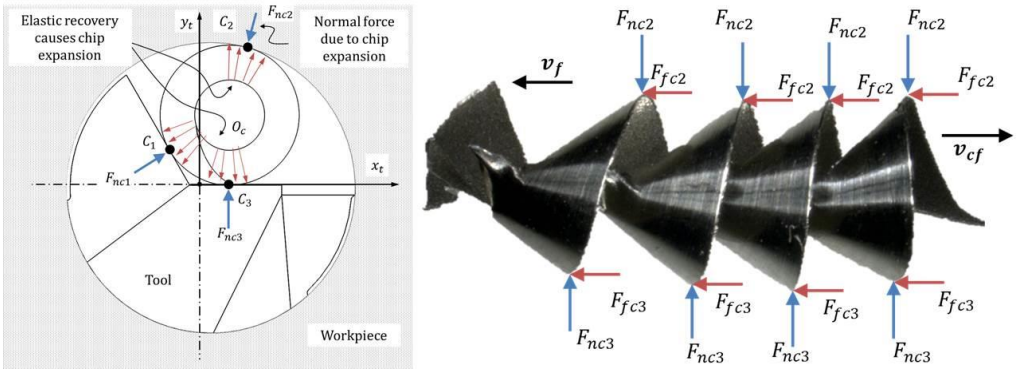

Figure 5.22 Normal and frictional forces acting on spiral chip due to elastic recovery

As the number of loops increases the contact points also increase causing increasing frictional forces which increase the φ_c as the $\boldsymbol{v_{cf}}$ decreases.

According to Feng et al.[63], the spiral chip speed with respect to drill flute can be approximately calculated as,

$$v_{cf} = \frac{R\omega}{t_{ctr}\pi d_{c-max}} p_c \tag{5.5}$$

Where, t_{ctr} is the chip thickness ratio, p_c is the pitch of the spiral chip, R is the drill radius and ω is the angular speed.

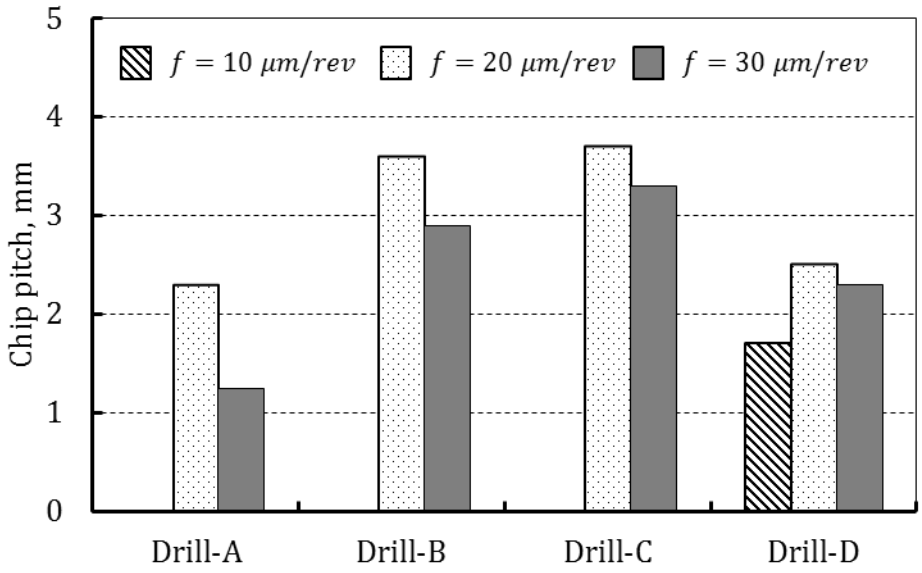

Figure 5.23 Measured chip pitch for spiral chips.

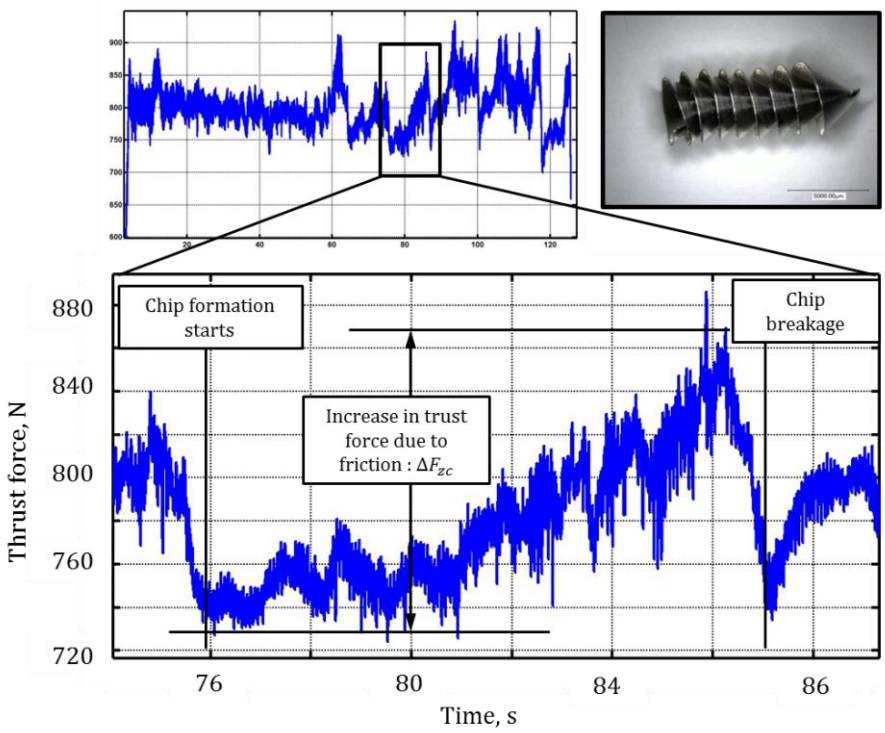

Figure 5.24 Increase in thrust force due to chip clogging for Drill-A at $f = 30\mu m/rev$

It is clear from Eq.(5.5) that the smaller pitch decreases the v_{cf} leading to difficult chip removal. It was also observed that as the outer cutting edge increases the pitch of the chip increases but decreases as the feed rate increases which can be seen in Figure 5.23. Increase in fictional force due to smaller pitch and larger diameter can cause chip clogging leading to increase in thrust force profile as shown in Figure 5.25 for Drill-A at $f = 30\mu m$. The increase in thrust force due to chip friction is summarized in Figure 5.25. The chips generated by Drill D at $f = 10\mu m$ did not increase the thrust force because its diameter was smaller than maximum possible chip diameter.

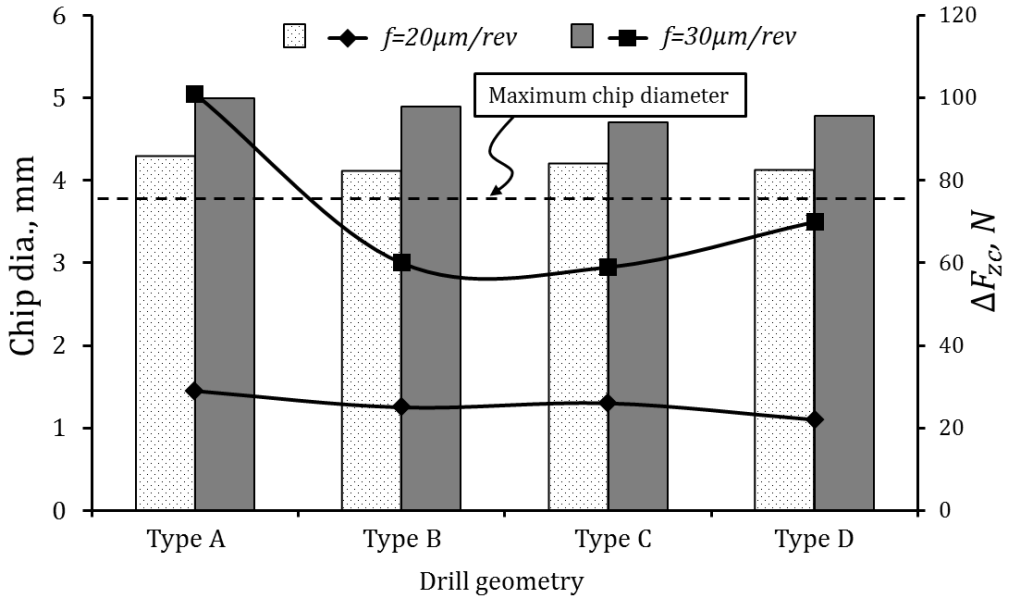

Figure 5.25 Increase in thrust force due to chip friction

5.4.3 Mechanism of spiral chip breaking

The total normal force and the frictional force increase with an increase in a number of loops of the spiral chip as the chip is in contact with drill and hole wall at more points. At the same time the surface area of the chip also increases. If the force exerted by the coolant is sufficiently high the chips are

broken. This condition was observed for spiral chips which were produced at $f = 20\mu m/rev$ and at $f = 30\mu m/rev$ for Drill-B and Drill-C. However, chip breaking mechanism changes at $f = 30\mu m/rev$ for Drill-A and Drill-D. At particular point when the frictional force is very high the $\boldsymbol{v_{cf}}$ becomes zero and the chip stops to move. The chip formation continues at the cutting edge which pushes the chips but resisted by the preexisting chips in the flute. At this point the chip starts to unwind which increases the pitch and the up-curl of the chip. As a result, the tensile strain on the free side of the chip increases and eventually reaches the critical limit due to chip straightening as shown in Figure 5.26.

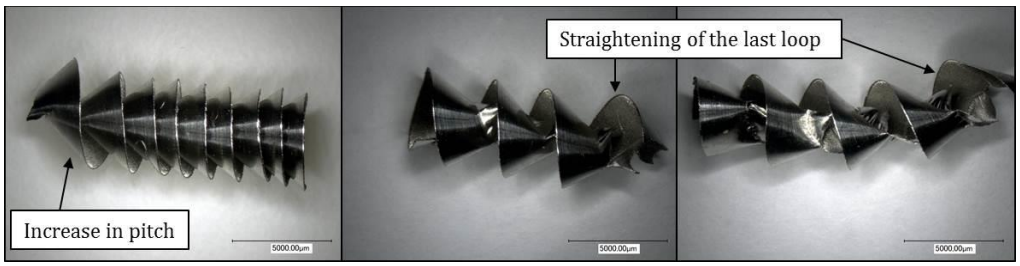

Figure 5.26 Increase in chip pitch and straightening of the chip

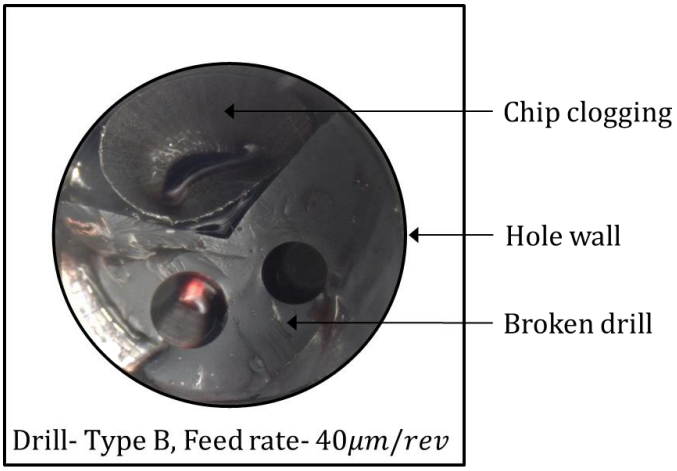

Figure 5.27 Broken drill due to chip clogging at $f = 40\ \mu m/rev$

The new chips in addition to the coolant pressure then push the broken chips. This particular condition is undesirable in deep hole drilling as the drilling depth increases, it may lead to tool breakage as shown in Figure 5.27.

5.5 Concluding Remarks

In this chapter, a comprehensive experimental study was presented to study the mechanics of chip formation in the single-lip drilling of Inconel 718. Based on the analysis following conclusions are drawn –

- The mechanism of chip formation changes with increasing feed rate and variation in tool geometry.
- At lower feed rates the elemental chips were produced which were easily broken by the available coolant pressure.
- At higher feed rates, spiral chips are formed which are difficult to break.
- The spiral chips with higher pitch are broken easily and the pitch is controlled by the outer cutting edge angle. Higher the outer cutting edge angle higher the pitch of the chips.
- The thicker chips experience greater elastic recovery hence exert greater frictional force which destabilizes the drilling process.
- To prevent chip clogging outer cutting edge angle should be more than 20^{o} and the feed rate should be less than 20 μm when coolant pressure is 4 MPa.

Chapter 6: Straightness Control in Deep Hole Drilling

In this chapter, a predictive hole straightness deviation model for multi supports deep hole drilling process is introduced. The model considers the effect of misalignment at whip guides in addition to the effects of the varying distance among the supports. The model also considers the effects of the thrust force and the drill lengths. Furthermore, the model was experimentally substantiated. Based on the understanding of misalignments and its effect on the straightness, a novel support module was developed to actively change the misalignment for the straightness control.

6.1 Drilling Strategy

The deep hole drilling process follows steps depicted in Figure 6.1.

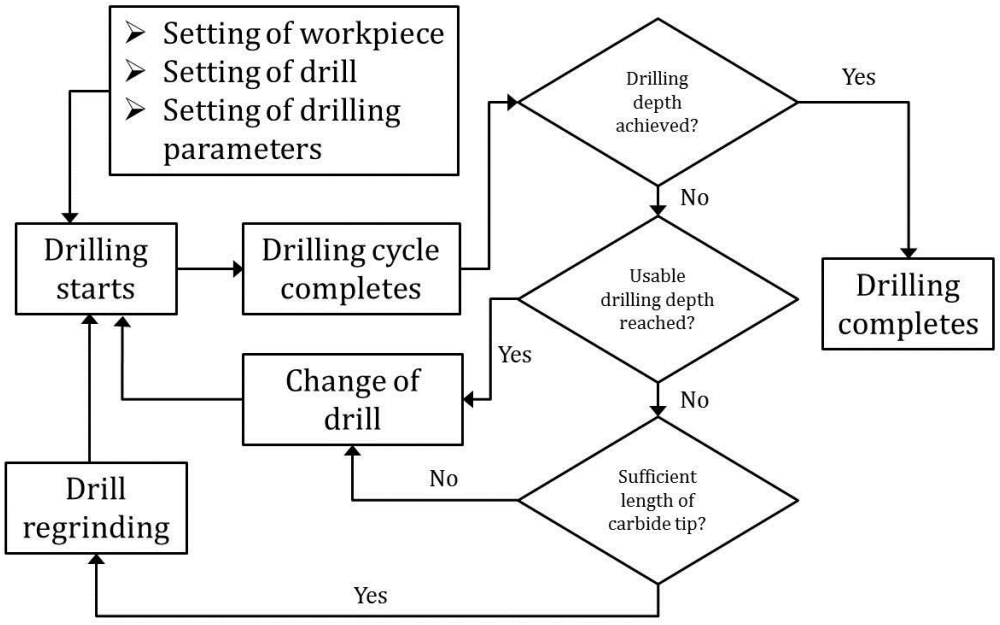

Figure 6.1 Deep hole drilling strategy

The drilling process starts once the workpiece, drill and machine parameters are set. Initially short drills are used as the long drills are prone to buckling.

The drilling process is divided into multiple cycles due to tool wear. Once the cycle completes, the drill has to satisfy two conditions.

Condition 1: Is effective drilling depth reached?

Condition 2: Is sufficient carbide tip is available for regrinding?

Based on the observation, the decision is made whether to change or regrind the drill. The information related to machine set-up and definition for various parameters is given in the next section.

6.2 Deep Hole Drilling Machine Setup

The deep hole drilling machine has intermediate supports to prevent the drill from whipping hence the supports are also called whip guides. The width of support base is $l_{s1} = l_{s2} = l_{s3} = l_s$. In addition, the chip box and pilot bush holder has combined length of l_{cb}. The effective drilling length (l_{eq}) for the drill of length L with n_s number of supports is,

$$l_{eq} = L - n_s l_s - l_{cb} \tag{6.1}$$

In this study, the support distances are measured from the initial position of the spindle when the drill is about to enter into the workpiece as shown in the Figure 6.2. The supports are numbered from the spindle to the drill bush in ascending order. The lengths l_1, l_2 and l_{fs} are the distances of first support, second support and the fixed chip-box support from the spindle respectively.

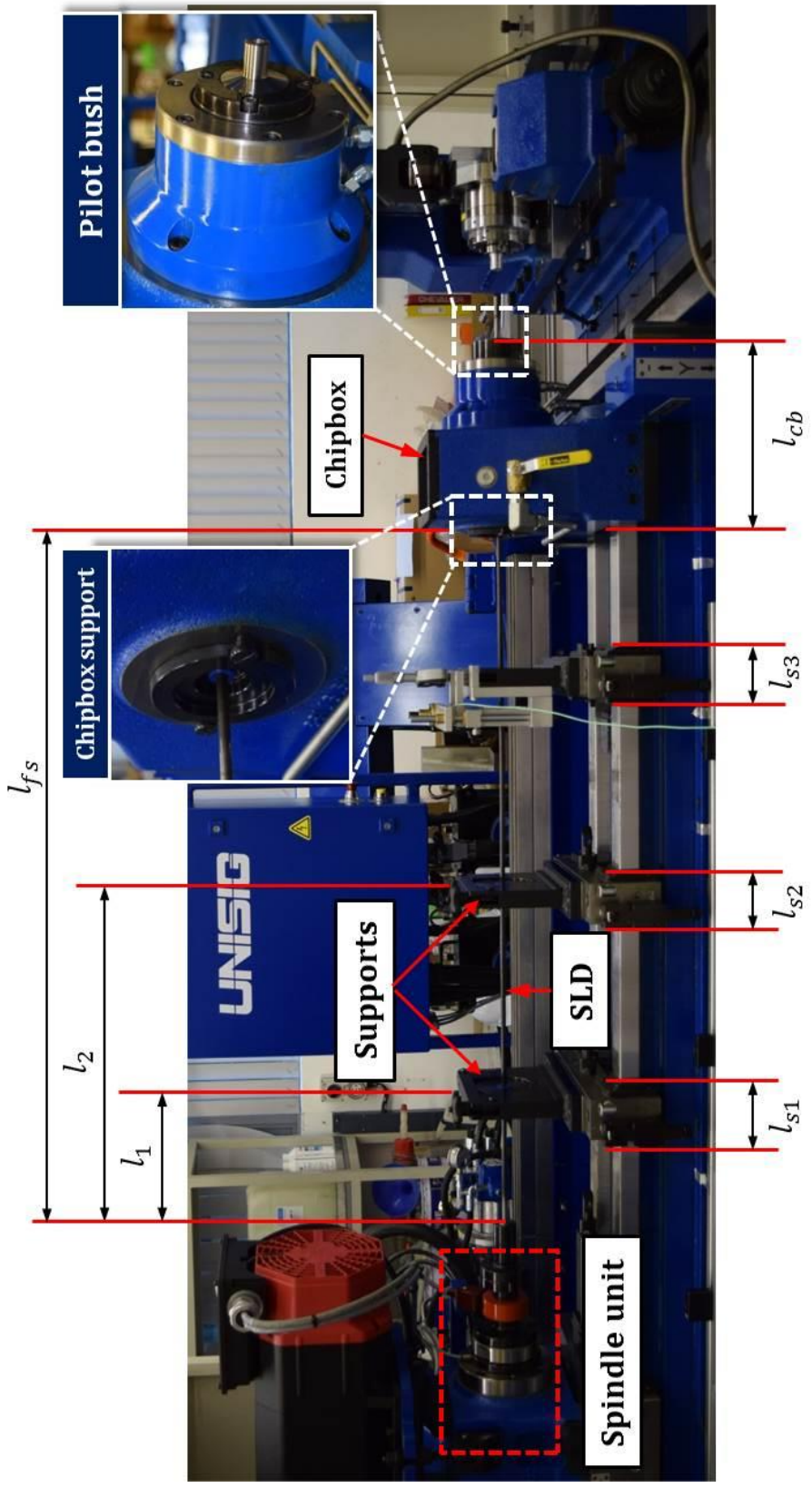

Figure 6.2 Deep hole drilling machine with multiple supports

The support has three main components as whip guide bush, circlip and bearing housing as shown in Figure 6.3.

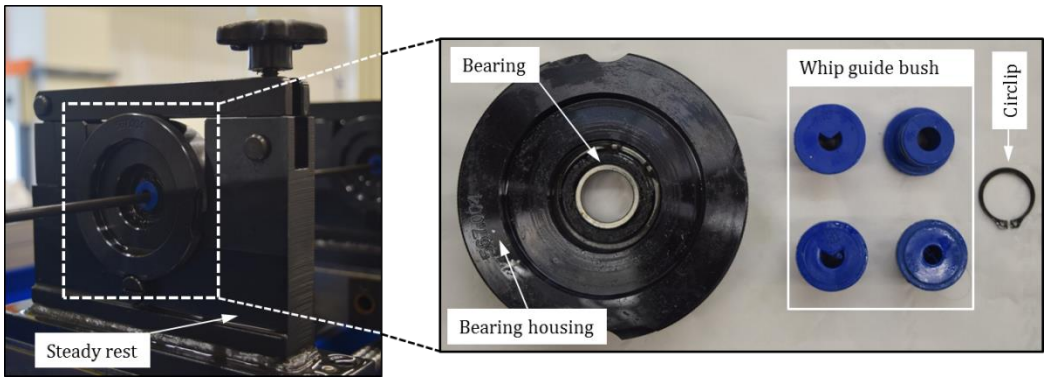

Figure 6.3 Components of drill support

The whip guide bush is made of polymers which suppress the vibrations and increases the hole accuracy. Due to its elastic properties, the whip bush stretches over the carbide tip and contracts on the drill shank e.g. $\emptyset 7.5\, mm$ whip bush is used for ∅8 mm SLD. However, the drill has to be frequently removed from the drilling machine for the regrinding due to faster tool wear while drilling Inconel-718. As a result, wear and tear occurs at the whip guide bush leading to misalignment at the support with respect the spindle axis. Improper setting of bearing in the housing may also cause the support misalignment. Deng et al.[31] studied the effect of drill bush and support misalignment on straightness which was limited to the single support without mentioning the cause of misalignment. However, in practice more than one supports are employed for the deep hole drilling process. Hence, a new model with multi-support misalignment is necessary to predict straightness deviation.

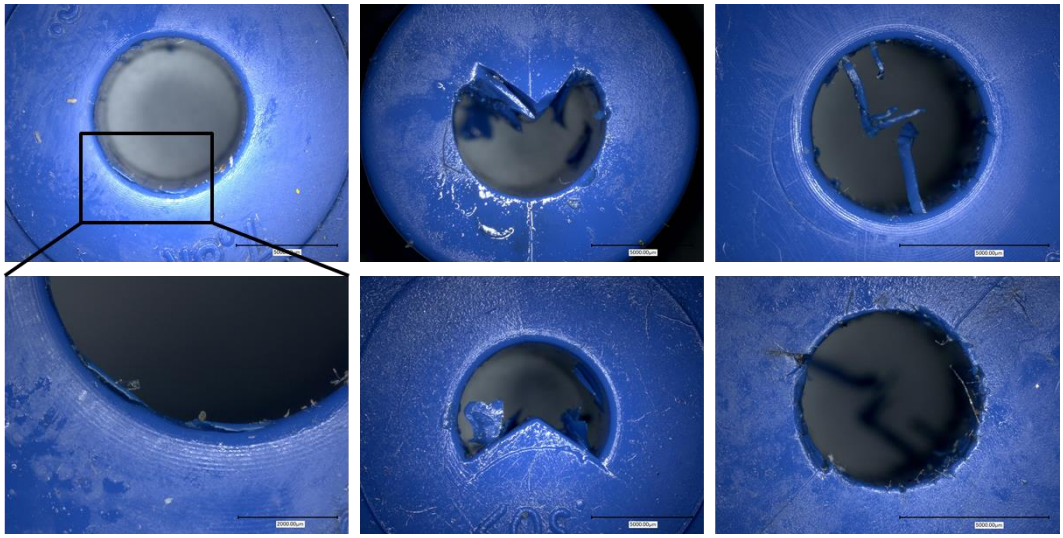

Figure 6.4 Damaged whip guide bushes

6.3 Predictive Modelling of Hole Straightness Deviation

6.3.1 Considerations for the modelling

6.3.1.1 Consideration 1

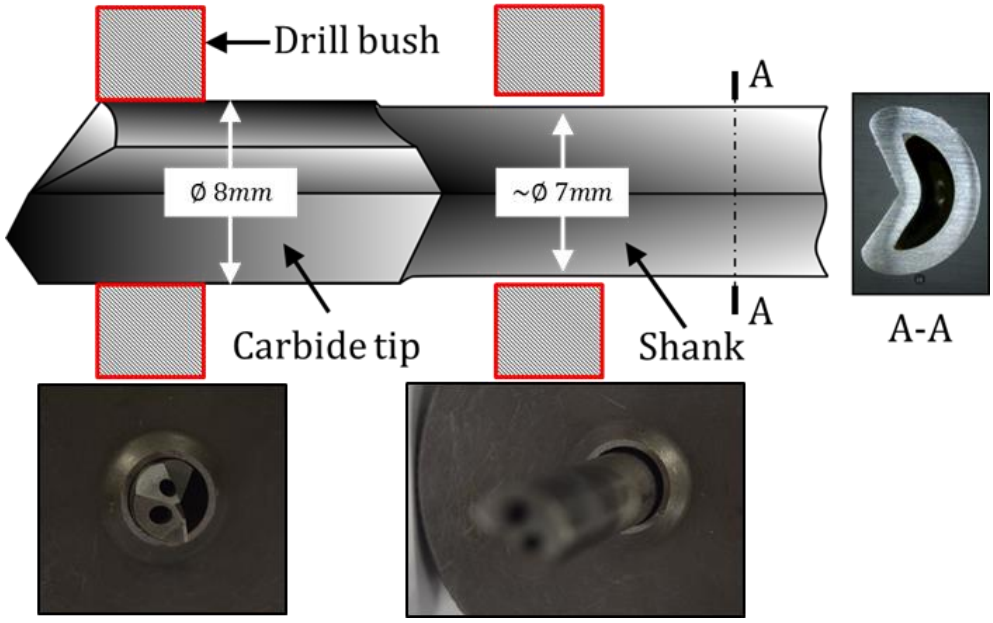

Figure 6.5 Difference in diameter of carbide tip and shank of SLD with respect to pilot bush diameter

The drill shank has a smaller diameter than that the drill bush diameter, as a result, once the carbide tip has passed the bush, the shank loses contact with the pilot bush. The immediate support is the support at chip box that has a greater influence on the deviation as compared to the pilot bush. To consider this effect in the model, the unsupported length is increased by l_{cb} once the drill tip passes the bush. However, this has to be considered only in the beginning of the drilling process simulation.

6.3.1.2 Consideration 2

During the drilling process, the distance between the first support and spindle decreases continuously as the drilling depth increases. The spindle reaches the first support after traveling length l_1 as shown in Figure 6.6(a). It starts to push the first support as depicted in Figure 6.6(b). The drilling process continues until all the supports reach the chip box as shown in the Figure 6.6(d) after drilling depth of l_{eq} which can be calculated using Eq.(6.1). For the modelling purpose, the spindle location conditions can be divided into three cases.

- Case I: Before reaching the first support
- Case II: After reaching the first support
- Case III: Before reaching the second support

Based on these considerations an analytical model is developed for two movable and a fixed chip-box support.

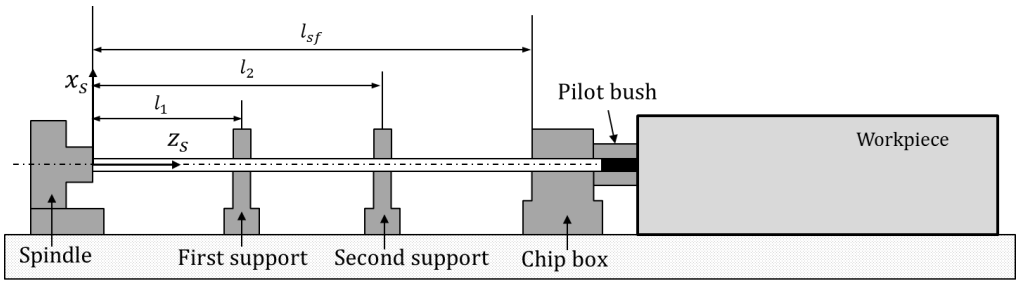

(a)Case I: Before reaching the first support

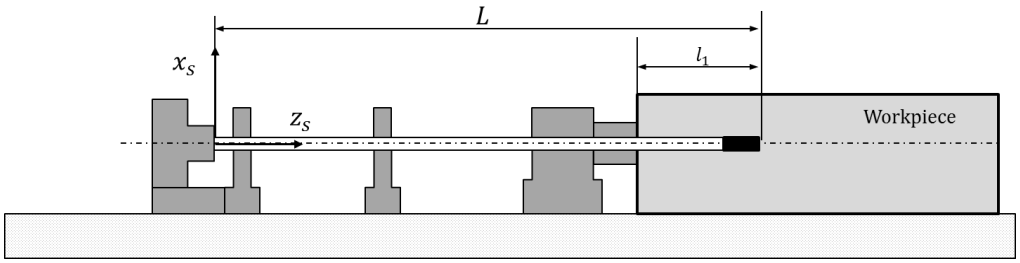

(b)Case II: After reaching the first support

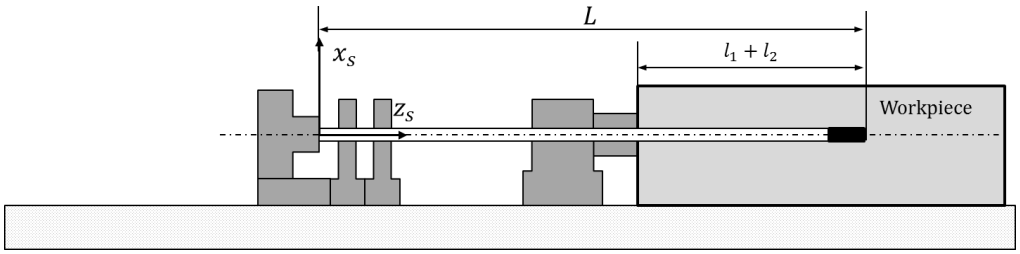

(c)Case III: Before reaching the chip-box support

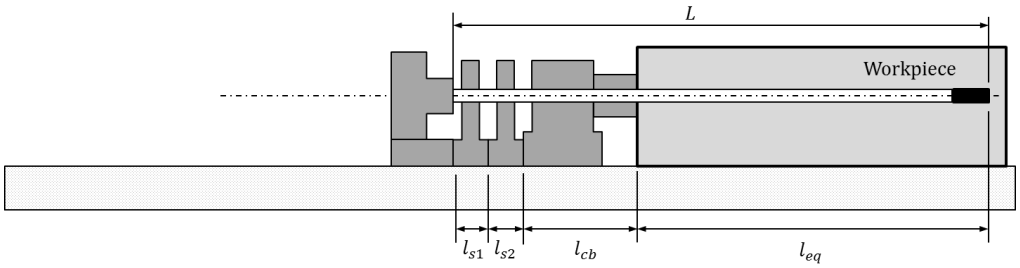

(d)Completion of the effective drilling length

Figure 6.6 Three modelling conditions based on spindle location (a)Case I (b) Case II, (c) Case III (d)Completion of the effective drilling depth.

6.3.2 Analytical model

A spindle coordinate system $(x_s y_s z_s)$ is defined at the center of the spindle for which the z_s is parallel to the spindle axis and x_s axis is perpendicular to the machine bed as shown in Figure 6.6(a). The drill shaft is modeled using Euler column theory [64] where the misalignments at the first, second, fixed chip-box supports and pilot bush are $\delta_1, \delta_2, \delta_3$ and δ_b respectively. The drilling thrust force (F_z) and the reaction force (R_x) is acting at the drill tip. The reaction forces at the first, second, fixed chip-box supports and pilot bush are R_1, R_2, R_{fs} and R_b respectively.

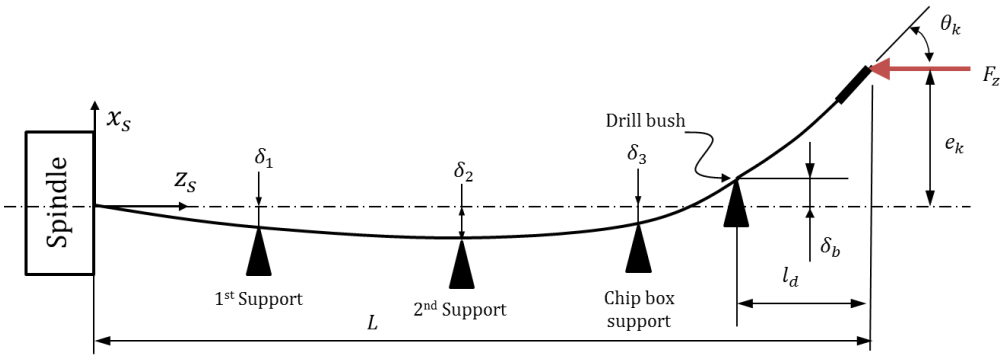

Figure 6.7 Drill tip deviation (e_k) at drilling depth (l_d)

The drill tip deviation at any given drilling depth after k^{th} cycle is e_k which can be calculated as,

$$e_k = e_{k-1} + \theta_{k-1} dz_s \tag{6.2}$$

Where, k is number of iterative drilling cycle for model and dz_s is the distance travelled in a single iteration. e_{k-1} and θ_{k-1} are the drill deviation and drill inclination at $(k-1)^{\text{th}}$ cycle respectively.

The moment at any position (z_s, x_s) is $M(z_s, x_s)$ which can be calculated separately for all three cases as follows. The second area moment (I_d) for cross section of drill shaft is calculated by using CAD software. The young modulus for the drill shaft material is E_d.

6.3.2.1 Case I: Before reaching the first support

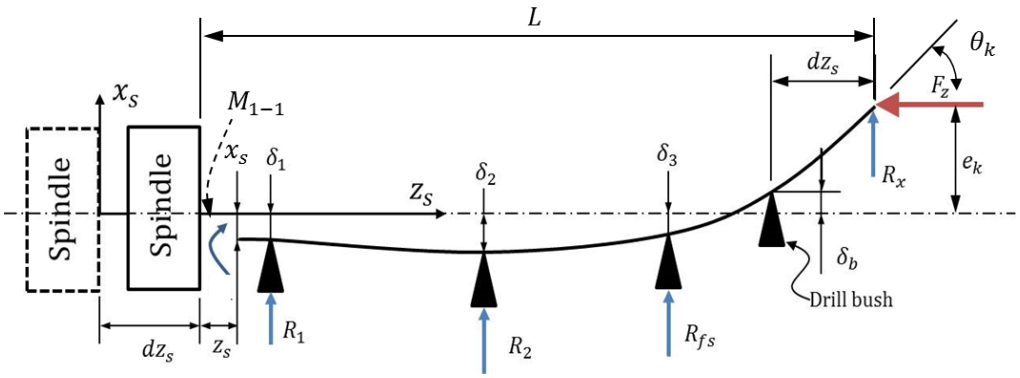

Figure 6.8 Moment for the section $0 < z_s < l_1$

The moment for the section $0 < z_s < l_1$ is,

$$M_{1-1} = E_d I_d \frac{d^2 x_{s1}}{dz_s^2} = F_z(e_k + \delta_3 - x_{s1}) + R_{fs}(l_{fs} - z_s) + R_2(l_2 - z_s) + R_1(l_1 - z_s) + R_x(L - z_s) \quad (6.3)$$

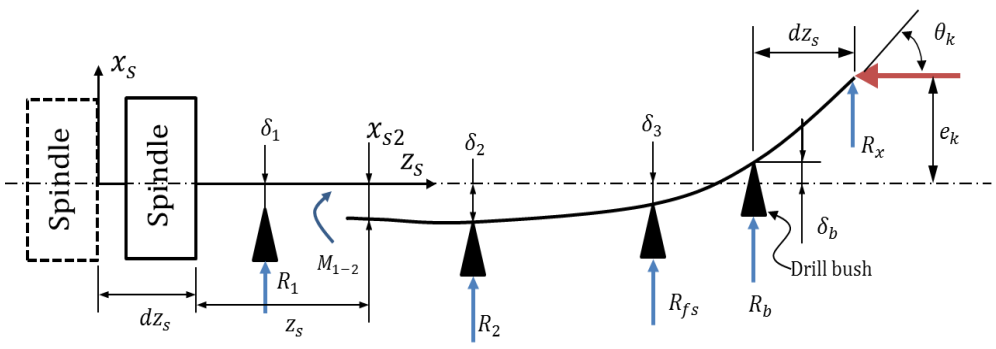

Figure 6.9 Moment for the section $l_1 < z_s < l_2$

The moment for the section $l_1 < z_s < l_2$ is,

$$M_{1-2} = E_d I_d \frac{d^2 x_{s2}}{dz_s^2} = F_z(e_k - x_{s2}) + R_{fs}\left(l_{fs} - z_s\right) + R_2(l_2 - z_s) + R_x(L - z_s) \tag{6.4}$$

The moment for the section $l_2 < z_s < l_{sf}$ is,

$$M_{1-3} = E_d I_d \frac{d^2 x_{s3}}{dz_s^2} = F_z(e_k - x_{s3}) + R_{fs}\left(l_{fs} - z_s\right) + R_x(L - z_s) \tag{6.5}$$

The moment for the section $l_{sf} < z_s < L$ is,

$$M_{1-4} = E_d I_d \frac{d^2 x_{s4}}{dz_s^2} = F_z(e_k - x_{s4}) + R_x(L - z_s) \tag{6.6}$$

As per consideration 1, for the first cycle of drilling the l_{fs}, δ_3 and R_{fs} will be replaced by $(l_{fs} + l_{cb})$, δ_b and R_b respectively during the calculations.

The Eq. (6.3)-(6.6) can be rewritten as equation with parameter $\xi = \sqrt{\frac{F_z}{E_d I_d}}$.

$$\frac{d^2 x_{s1}}{dz_s^2} + \xi^2 x_{s1} = \xi^2 \left\{(e_k + \delta_3 - x_{s1}) + \frac{R_{fs}}{F_z}\left(l_{fs} - z_s\right) + \frac{R_2}{F_z}(l_2 - z_s) + \frac{R_1}{F_z}(l_1 - z_s) + \frac{R_x}{F_z}(L - z_s)\right\} \tag{6.7}$$

$$\frac{d^2 x_{s2}}{dz_s^2} + \xi^2 x_{s2} = \xi^2 \left\{(e_k + \delta_3 - x_{s1}) + \frac{R_{fs}}{F_z}\left(l_{fs} - z_s\right) + \frac{R_2}{F_z}(l_2 - z_s) + \right. \tag{6.8}$$

$\frac{R_x}{F_z}(L - z_s)\Big\}$

$$\frac{d^2x_{s3}}{dz_s^2} + \xi^2 x_{s3} = \xi^2\left\{(e_k + \delta_3 - x_{s1}) + \frac{R_{fs}}{F_z}\left(l_{fs} - z_s\right) + \frac{R_x}{F_z}(L - z_s)\right\} \tag{6.9}$$

$$\frac{d^2x_{s4}}{dz_s^2} + \xi^2 x_{s4} = \xi^2\left\{(e_k + \delta_3 - x_{s1}) + \frac{R_x}{F_z}(L - z_s)\right\} \tag{6.10}$$

The general solutions for the Eqs.(6.7)-(6.10) are given by Eqs.(6.11)-(6.14).

$$x_{s1} = U_1 \cos\xi z_s + V_1 \sin\xi z_s + (e_k + \delta_3) + \frac{R_{fs}}{F_z}\left(l_{fs} - z_s\right) + \frac{R_2}{F_z}(l_2 - z_s) + \frac{R_1}{F_z}(l_1 - z_s) + \frac{R_x}{F_z}(L - z_s) \tag{6.11}$$

$$x_{s2} = U_2 \cos\xi z_s + V_2 \sin\xi z_s + (e_k + \delta_3) + \frac{R_{fs}}{F_z}\left(l_{fs} - z_s\right) + \frac{R_2}{F_z}(l_2 - z_s) + \frac{R_x}{F_z}(L - z_s) \tag{6.12}$$

$$x_{s3} = U_3 \cos\xi z_s + V_3 \sin\xi z_s + (e_k + \delta_3) + \frac{R_{fs}}{F_z}\left(l_{fs} - z_s\right) + \frac{R_x}{F_z}(L - z_s) \tag{6.13}$$

$$x_{s4} = U_4 \cos\xi z_s + V_4 \sin\xi z_s + (e_k + \delta_3) + \frac{R_x}{F_z}(L - z_s) \tag{6.14}$$

To solve Eqs.(6.11)-(6.14), following boundary conditions were applied.

$x_{s4}(L) = e_k + \delta_3$, $x_{s4}\left(l_{sf}\right) = \delta_3$,$x'_{s4}\left(l_{fs}\right) = x'_{s3}\left(l_{fs}\right)$, $x_{s3}(l_2) = -\delta_2$,

$x_{s3}(l_1) = -\delta_1$, $x_{s1}(0) = 0$, $x'_{s1}(0) = 0$, $x'_{s1}(l_l) = x'_{s2}(l_1)$, $x_{s1}(l_1) = -\delta_1$,

$x'_{s2}(l_2) = x'_{s3}(l_2)$, $x_{s3}(l_{sf}) = -\delta_3$ and $x_{s2}(l_2) = -\delta_2$.

The matrices obtained in the process of solving the equation can be expressed in the compact format as,

$$A_1 B_1 = C_1$$

The solution for the unknowns is given as,

$$B_1 = A_1^{-1} C_1$$

Where A_1 and C_1 is given by Eq.(6.18) and Eq.(6.19) respectively whereas,

$$B'_1 = [U_1 \quad V_1 \quad U_2 \quad V_2 \quad U_3 \quad V_3 \quad U_4 \quad V_4 \quad R_{fs} \quad R_1 \quad R_2 \quad R_x]$$

The governing equation for drill shaft for the interval $l_{sf} < z_s < L$ is ,

$$x'_{s4} = -U_4 \xi \sin \xi z_s + V_4 \cos \xi z_s - \frac{R_x}{F_z} \tag{6.15}$$

Therefore the inclination θ_k of the tool head can be calculated by using Eq.(6.16).

$$\theta_k = x'_{s4}(L) = -U_4 \xi \sin \xi L + V_4 \cos \xi L - \frac{R_x}{F_z} \tag{6.16}$$

The deviation (e_k) of the tool head at k^{th} cycles is given by Eq.(6.17).

$$e_k = e_{k-1} + \theta_{k-1} dz_s \tag{6.17}$$

$$A_1 = \begin{pmatrix}
0 & 0 & 0 & 0 & 0 & 0 & cos\xi L & sin\xi L & 0 & 0 & 0 & 0 & 0 \\
0 & 0 & 0 & 0 & 0 & 0 & cos\xi l_{fs} & sin\xi l_{fs} & 0 & 0 & 0 & 0 & \frac{(L-l_{fs})}{F_z} \\
0 & 0 & 0 & 0 & -\xi sin\xi l_{fs} & \xi cos\xi l_{fs} & \xi sin\xi l_{fs} & -\xi cos\lambda l_{fs} & -\frac{1}{F_z} & 0 & 0 & 0 & 0 \\
0 & 0 & 0 & 0 & cos\lambda l_2 & sin\lambda l_2 & 0 & 0 & \frac{(l_3-l_2)}{F_z} & 0 & 0 & \frac{(L-l_2)}{PF_z} & \frac{(L-l_1)}{F_z} \\
0 & 0 & cos\xi l_1 & sin\xi l_1 & 0 & 0 & 0 & 0 & \frac{(l_{fs}-l_1)}{F_z} & 0 & \frac{(l_2-l_1)}{F_z} & \frac{l_1}{F_z} & \frac{L}{F_z} \\
1 & 0 & 0 & 0 & 0 & 0 & 0 & 0 & \frac{l_{fs}}{F_z} & \frac{l_2}{F_z} & \frac{1}{F_z} & \frac{1}{F_z} & \frac{1}{F_z} \\
0 & \xi & 0 & 0 & 0 & 0 & 0 & 0 & \frac{1}{F_z} & \frac{1}{F_z} & 0 & 0 & 0 \\
-\xi sin\xi l_1 & \xi cos\xi l_1 & \xi sin\xi l_1 & -\xi cos\xi l_1 & 0 & 0 & 0 & 0 & \frac{(l_3-l_1)}{F_z} & 0 & \frac{(l_2-l_1)}{F_z} & \frac{(L-l_1)}{F_z} & \frac{(L-l_1)}{F_z} \\
\xi cos\xi l_1 & \xi sin\xi l_1 & 0 & 0 & 0 & 0 & 0 & 0 & 0 & 0 & \frac{1}{F_z} & 0 & 0 \\
0 & 0 & -\xi sin\xi l_2 & \xi cos\lambda l_2 & \xi sin\xi l_2 & -\xi cos\xi l_2 & 0 & 0 & 0 & 0 & 0 & \frac{(L-l_{fs})}{F_z} & \frac{(L-l_1)}{F_z} \\
0 & 0 & 0 & 0 & cos\xi l_{fs} & sin\xi l_{fs} & 0 & 0 & 0 & 0 & 0 & 0 & 0 \\
0 & 0 & cos\xi l_2 & sin\xi l_2 & 0 & 0 & 0 & 0 & \frac{(l_3-l_2)}{F_z} & 0 & 0 & \frac{(L-l_2)}{F_z} & \frac{(L-l_2)}{F_z}
\end{pmatrix} \tag{6.18}$$

$$C'_1 = [0 \quad -e_k \quad 0 \quad -\delta_2 - \delta_3 - e_k \quad -\delta_1 - \delta_3 - e_k \quad -\delta_3 - e_k \quad 0 \quad 0 \quad -\delta_1 - \delta_3 - e_k \quad 0 \quad -e_k \quad -\delta_2 - \delta_3 - e_k \,] \tag{6.19}$$

6.3.2.2 Case II: After reaching the first support

The spindle starts to push the first support, once it reaches the support. As a result, the distance between the second and third support decreases. The moments governing the shaft are similar to the Case-I however, the moment M_{1-1} is not required for this case.

The moments governing the drill shafts are –

$M_{2-2} = M_{1-2}$ for $l_1 < z_s < l_2$

$M_{2-3} = M_{1-3}$ for $l_2 < z_s < l_{sf}$ and

$M_{2-4} = M_{1-4}$ for $l_{sf} < z_s < L$

The general solution obtained for x_{s2}, x_{s3} and x_{s4} are solved with following boundary conditions.

$x_{s2}(0) = 0$, $x'_{s2}(0) = 0$, $x_{s4}(L) = e_k + \delta_3$, $x_{s4}(l_{sf}) = \delta_3$, $x'_{s4}(l_{fs}) = x'_{s3}(l_{fs})$, $x_{s3}(l_2) = -\delta_2$, $x'_{s2}(l_2) = x'_{s3}(l_2)$, $x_{s3}(l_{sf}) = \delta_3$, $x_{s2}(l_2) = -\delta_2$.

The equations are expressed in the matrix form as,

$$A_2 B_2 = C_2$$

$$B_2 = A_2^{-1} C_2$$

Where, A_2 and C_2 are calculated using Eq.(6.20) and Eq.(6.21) whereas B'_2 is,

$$B'_2 = [U_2 \quad V_2 \quad U_3 \quad V_3 \quad U_4 \quad V_4 \quad R_{fs} \quad R_1 \quad R_2 \quad R_x]$$

$$A_2 = \begin{pmatrix} 0 & 0 & 0 & 0 & cos\xi L & sin\xi L & 0 & 0 & 0 & 0 \\ 0 & 0 & 0 & 0 & cos\xi l_{fs} & sin\xi l_{fs} & 0 & 0 & 0 & \frac{(L-l_{fs})}{F_z} \\ 0 & 0 & -\xi sin\xi l_3 & \xi cos\xi l_3 & \xi sin\xi l_3 & -\xi cos\xi l_{fs} & -\frac{1}{F_z} & 0 & 0 & 0 \\ 0 & 0 & cos\xi l_2 & sin\xi l_2 & 0 & 0 & \frac{(l_{fs}-l_2)}{F_z} & 0 & -\frac{1}{F_z} & \frac{(L-l_2)}{F_z} \\ -\xi sin\xi l_2 & \xi cos\xi l_2 & \xi sin\xi l_2 & -\xi cos\xi l_2 & 0 & 0 & 0 & 0 & 0 & 0 \\ 0 & 0 & cos\xi l_{fs} & sin\xi l_{fs} & 0 & 0 & 0 & 0 & 0 & \frac{(L-l_{fs})}{F_z} \\ 1 & 0 & 0 & 0 & 0 & 0 & \frac{l_{fs}}{F_z} & \frac{l_2}{F_z} & \frac{L}{F_z} & \\ 0 & \xi & 0 & 0 & 0 & 0 & -\frac{1}{F_z} & -\frac{1}{F_z} & -\frac{1}{F_z} & \\ cos\xi l_2 & sin\xi l_2 & 0 & 0 & 0 & 0 & \frac{(l_{fs}-l_2)}{F_z} & 0 & \frac{(L-l_2)}{F_z} & \end{pmatrix} \tag{6.20}$$

$$C'_2 = (0 \quad -e_k \quad 0 \quad -\delta_2 - \delta_3 - e_k \quad 0 \quad -e_k \quad -e_k - \delta_3 \quad -e_k \quad -\delta_2 - \delta_3 - e_k) \tag{6.21}$$

6.3.2.3 Case III: After reaching the second support

Here, the moments governing the interval $l_2 < z_s < l_{sf}$ and $l_{sf} < z_s < L$ are same as the previous cases.

$M_{3-3} = M_{1-3}$ for $l_2 < z_s < l_{sf}$ and

$M_{3-4} = M_{1-4}$ for $l_{sf} < z_s < L$

The general solutions obtained for the equations are solved with the following boundary conditions.

$x_{s4}(L) = e_k + \delta_3, \quad x_{s4}(l_{sf}) = \delta_3, \quad x'_{s4}(l_{fs}) = x'_{s3}(l_{fs}), \quad x_{s3}(l_{sf}) = \delta_3,$

$x_{s3}(0) = 0, x'_{s3}(0) = 0$

The matrix obtained after substistuting the boundary conditions is expressed as,

$A_3 B_3 = C_3$ and B_3 can be calculated as $B_3 = A_3^{-1} C_3$

Where, $B'_3 = [U_3 \quad V_3 \quad U_4 \quad V_4 \quad R_{fs} \quad R_x]$;

$C'_3 = [-e_k \quad 0 \quad -\delta_3 - e_k \quad -\delta_3 - e_k \quad 0 \quad 0]$ and

$$A_3 = \begin{pmatrix} 1 & 0 & 1 & 1 & \frac{L}{F_z} & -\frac{l_{sf}}{F_z} \\ 0 & \xi & 0 & 0 & -\frac{1}{F_z} & \frac{1}{F_z} \\ cos\xi l_{sf} & sin\xi l_{sf} & 0 & 0 & \frac{(L-l_{sf})}{F_z} & 0 \\ 0 & 0 & cos\xi l_{sf} & sin\xi l_{sf} & \frac{(L-l_{sf})}{F_z} & 0 \\ 0 & 0 & cos\xi l_{sf} & sin\xi l_{sf} & 0 & 0 \\ -\xi sin\xi l_{sf} & \xi cos\xi l_{sf} & \xi sin\xi l_{sf} & -\xi cos\xi l_{sf} & 0 & \frac{1}{F_z} \end{pmatrix}$$

6.3.3 Working of the model

The tool tip deviation is calculated using the steps given in the Figure 6.10. The input parameters can be divided into three main categories- machine setting parameters, drill setting parameters and drilling parameters. The machine parameters are the chip box length (l_{cb}), support base length (l_s) and misalignments at supports. The drill parameters include drill length (L), drill geometry and the distance between the supports. The drilling parameters feed rate (f), coolant pressure are required for prediction thrust force using the model developed in Chapter 4.

The simulation starts once all the parameters are updated in the MATLAB program. The drill moves by length dz_s for an iteration and in this analysis, dz_s is given as the feed per revolution (f). Based on the dz_s value number of iterations per case are carried out. Once the simulation for the Case I is completed, the misalignment at the first support is neglected for the further cases. Similarly, once the simulation for the Case II is completed, the misalignment at the second support is neglected for the further simulation.

Once the equivalent length of drill is achieved the simulation stops. If the required depth is reached, the straightness deviation is plotted for the given parameters. However, if the required drilling depth is not reached then longer drill parameters are updated before running the simulation for the new parameters.

Based on the developed model effect of various parameters on the straightness deviation is studied.

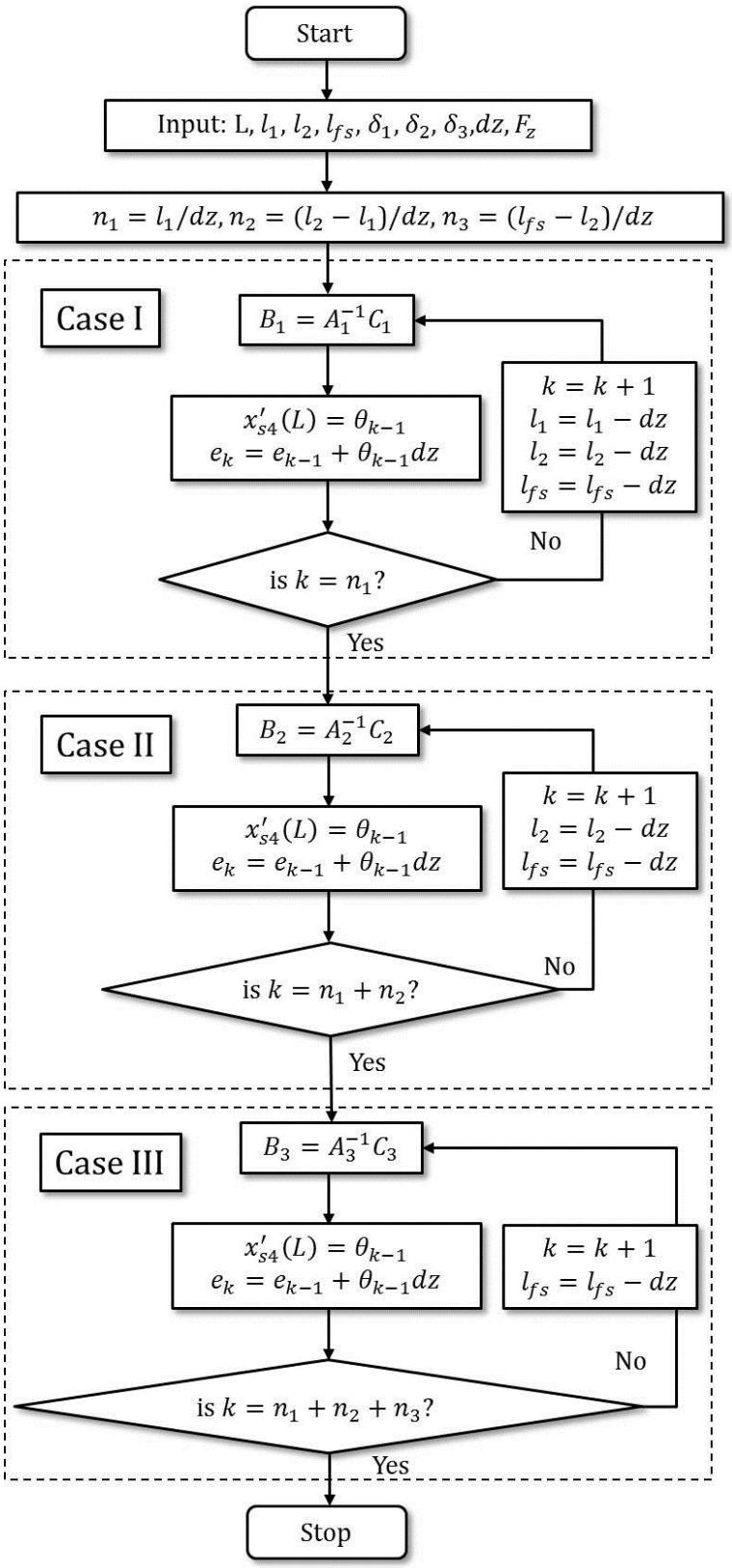

Figure 6.10 Flow chart for computing the drill head deviation

6.3.4 The effects of the misalignments

The misalignments at supports are inevitable due to wear and tear of whip guide bushes. The effects of misalignment at three supports are separately studied in this section. The simulations were run for the drill length of 1.5 m with thrust force of 370 N which was calculated using predictive force model at $f = 10\,\mu m/rev$. The drilling depth was set as 1 m and the support distances are set as 0.35 m, 0.76 m and 1.18 m for the first, second and the fixed supports respectively for all the simulations. The pilot bushing misalignment is neglected in this analysis.

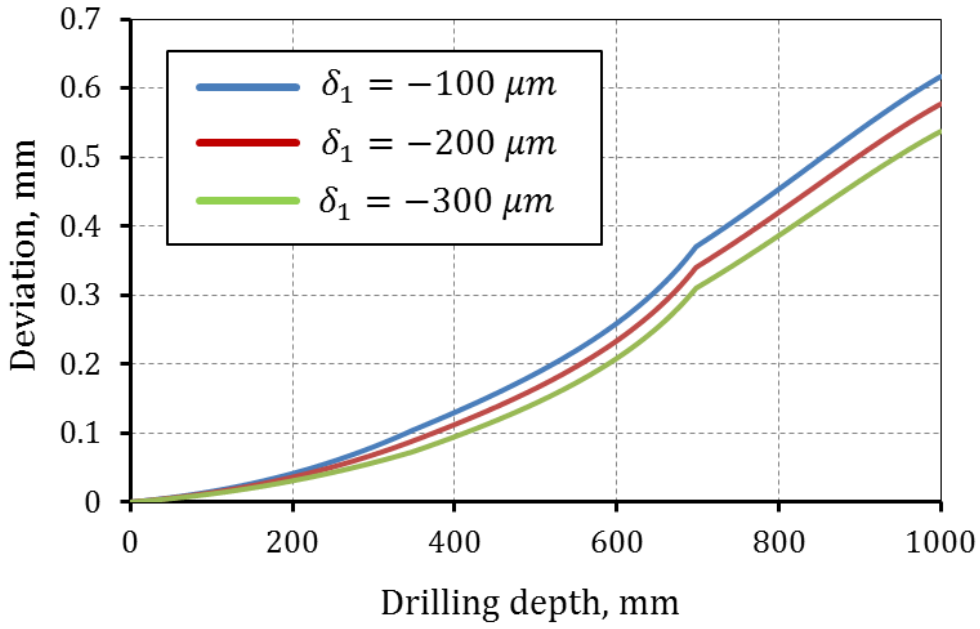

Figure 6.11 Effect of misalignment at first support (δ_1) on the straightness deviation ($\delta_2 = -100\mu m, \delta_3 = -100\mu m$)

The straightness deviation decreases as the misalignment at first support (δ_1) increases for same values of thrust force and support distances. However, the misalignment at first support has limited effect on the straightness deviation as shown in Figure 6.11 where the deviation only changes by 16%

per 100 μm increase in misalignment. The straightness deviation increases by 40 % for 100 μm increase in the misalignment at second support (δ_2) as shown Figure 6.12.

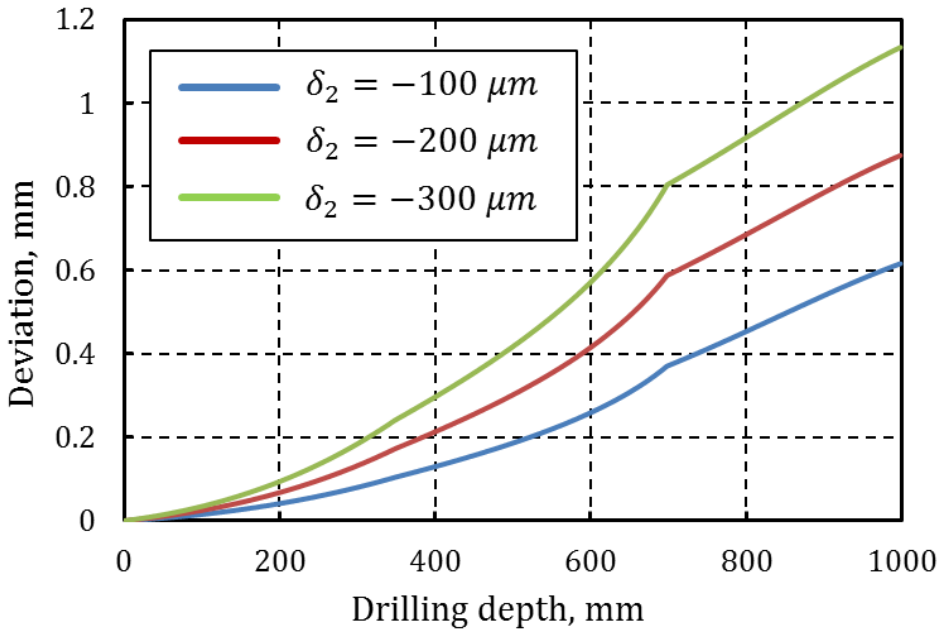

Figure 6.12 Effect of misalignment at the second support (δ_2) on the straightness deviation ($\delta_1 = -100\mu m, \delta_3 = -100\mu m$)

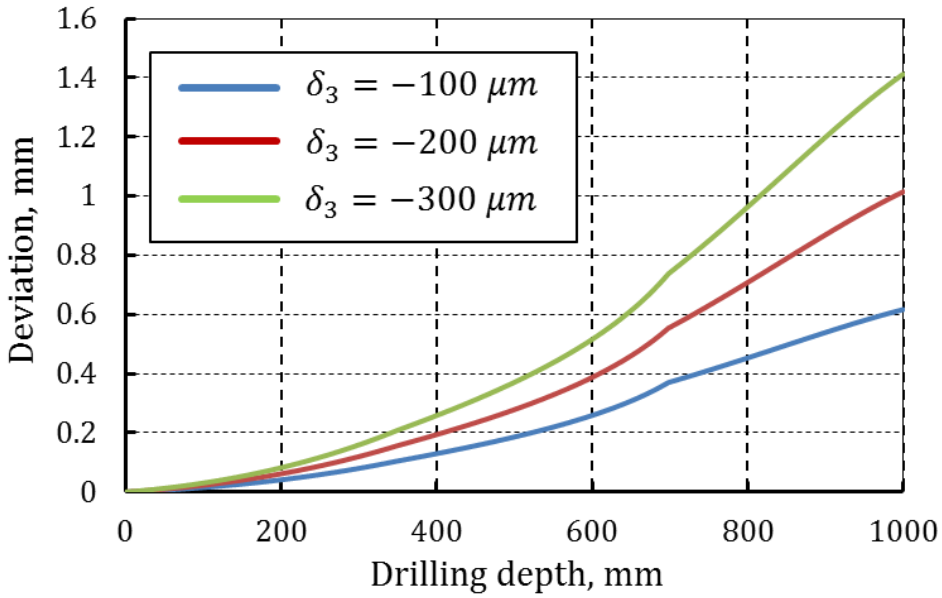

Figure 6.13 Effect of misalignment at the fixed support (δ_3) on the straightness deviation ($\delta_1 = -100\mu m, \delta_2 = -100\mu m$)

The straightness deviation is further amplified by the misalignment at the fixed support (δ_3) as shown in Figure 6.13 where 60% increase was observed for 100 μm increase of misalignment at fixed support.

6.3.5 The effects of the support distance

The simulations were run for the drill length of 1.5 m with thrust force of 370 N which was calculated using predictive force model at $f = 10\ \mu m/rev$. The misalignment at the three supports were fixed as $\delta_1 = -200\ \mu m, \delta_2 = -200 \mu m$ and $\delta_3 = -200\ \mu m$.

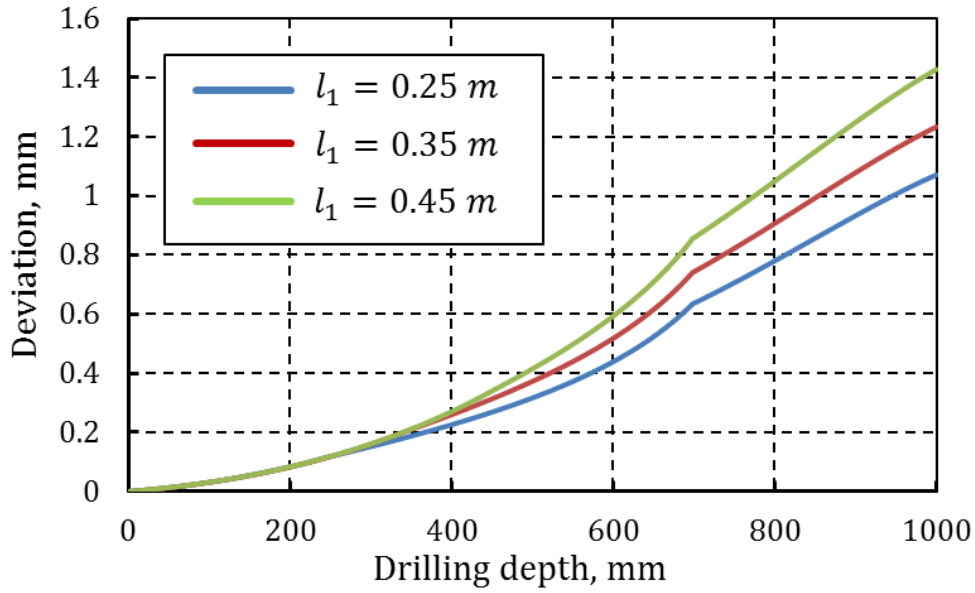

Figure 6.14 Effects of the first support distance (l_1) on the straightness deviation ($l_2 = 0.76m, l_{fs} = 1.18m$)

The straightness deviation increases as the first support distance increases as shown Figure 6.14. The deviation increases by 20% for 100 mm increase in the support distance. The effects of second support distance on the straightness deviation are more drastic as compared to the effects of the first

support as shown in Figure 6.15. The deviation increases exponentially for the $l_2 = 0.76\ m$.

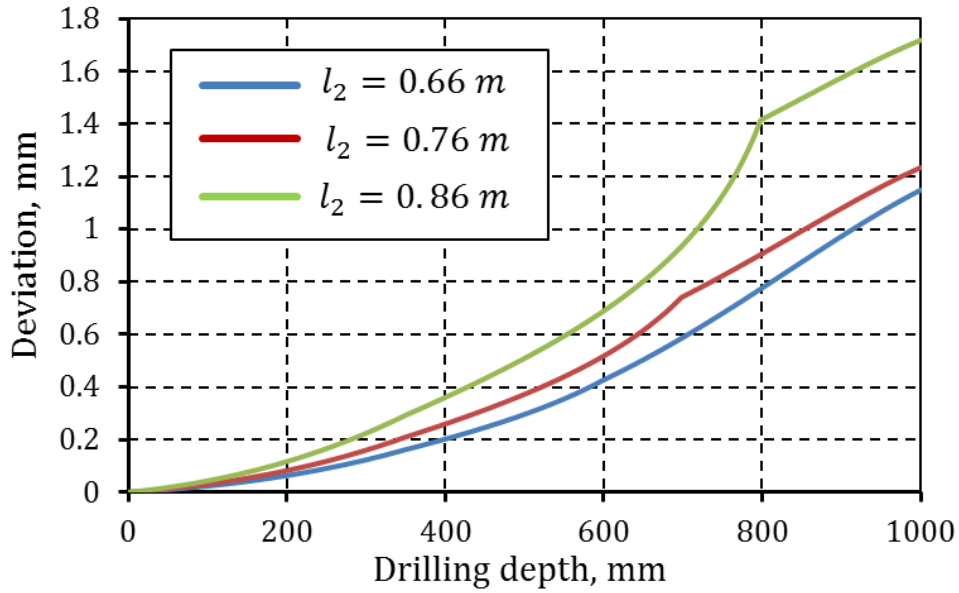

Figure 6.15 Effect of the second support distance (l_2) on the straightness deviation ($l_1 = 0.35m, l_{fs} = 1.18m$),

It should be noted that the distance between the first and second support decreases as the first support distance increases which lead to the increase in shaft stiffness. In general, the stiffer shafts are preferred to avoid the buckling of the drill at high feed rate drilling. However, the stiffer shaft with misalignments amplified the straightness deviation. A similar phenomenon was observed for the second support where the decrease in distance between second and third support increases the drill deviation.

6.3.6 The effects of the thrust force

The simulations were run for the drill length of 1.5 m with $l_1 = 0.35m, l_2 = 0.76m,\ l_{fs} = 1.18m, \delta_1 = -200\ \mu m, \delta_2 = -200\ \mu m, \delta_3 = -200\ \mu m$. The thrust force ($F_z$) can be increased by various factors such as increase in feed

rate, tool wear and chip clogging. Moreover, as discussed in Chapter 4, if the ratio (t_o/r_e) of uncut chip thickness and cutting edge radius below one then it may also increase the thrust force. It was observed that the drill deviation increases as the thrust force increases as shown in Figure 6.16.

In Figure 6.16, a sudden change in direction of drill tip was observed once the first support reaches the second support where the effect of misalignment at second support disappears as the length between the spindle and the second support is very short. However, in practice the change in the direction of the tool tip is not severe due to resistance by the hole wall. This effect should be incorporated in the future modelling of straightness deviation. The drill starts to buckle when F_z is more than 420 N for the given support distances and misalignments.

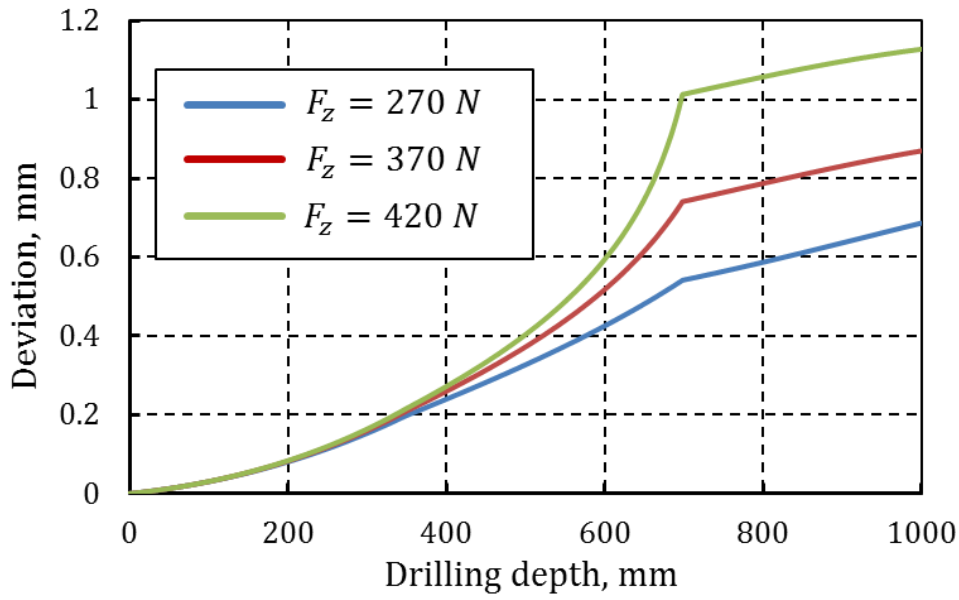

Figure 6.16 Effect of thrust force on drill deviation ($l_1 = 0.35m, l_1 = 0.76m, l_{fs} = 1.18m, \delta_1 = -200\mu m, \delta_2 = -200\mu m, \delta_3 = -200\mu m$)

6.4 Straightness Control

From the analysis, it is clear that the misalignment at the fixed support has greater influence on the straightness deviation. However, currently, there is no mechanism to actively control the misalignment. Hence, a novel setup was developed to control the misalignment at the fixed support using movable bearing housing. The setup is explained in the next section.

6.4.1 Working of the movable bearing housing

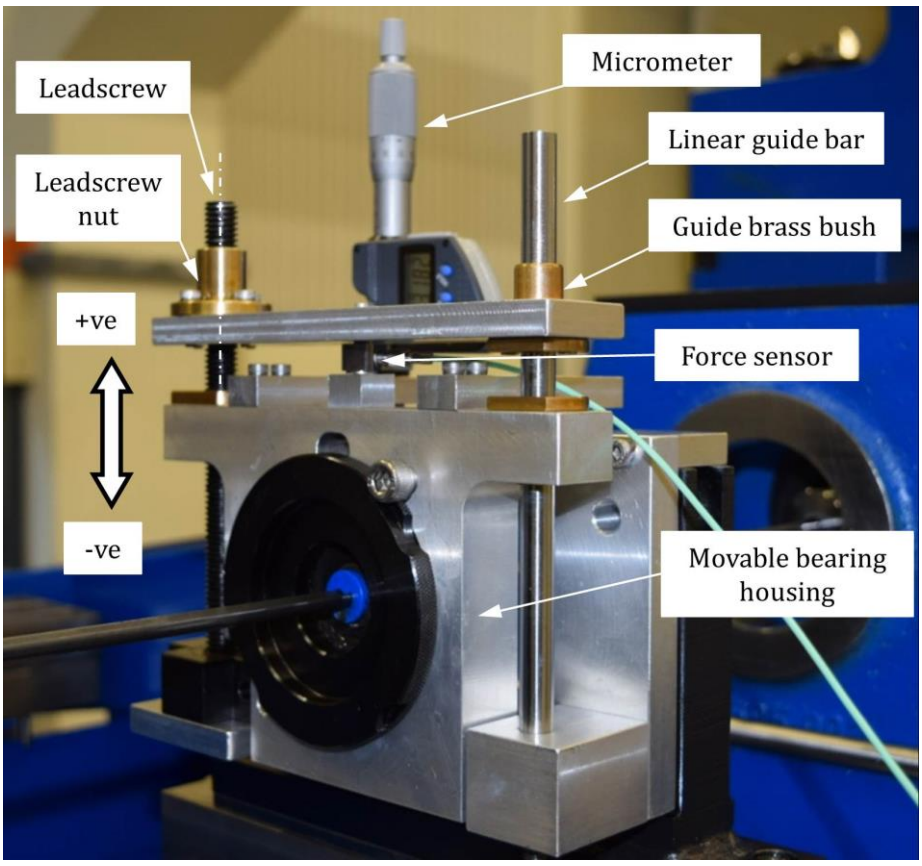

Figure 6.17 Movable bearing housing assembly

The movable bearing assembly can be used to control the misalignment in the vertical direction. The movement can be precisely controlled by rotating the lead-screw whereas the linear guide bar prevents the bearing assembly from tilting. The micrometer is attached to the assembly for precise misalignment

measurement. The developed module was mounted on an intermediate support near the fixed chip box support. The magnitude of the misalignment for the straightness control was determined using the straightness deviation model as follows.

6.4.2 Active control of the misalignment

The misalignment at the fix support can be used to compensate the effect of misalignments at other supports. The concept of active misalignment control is illustrated using following example.

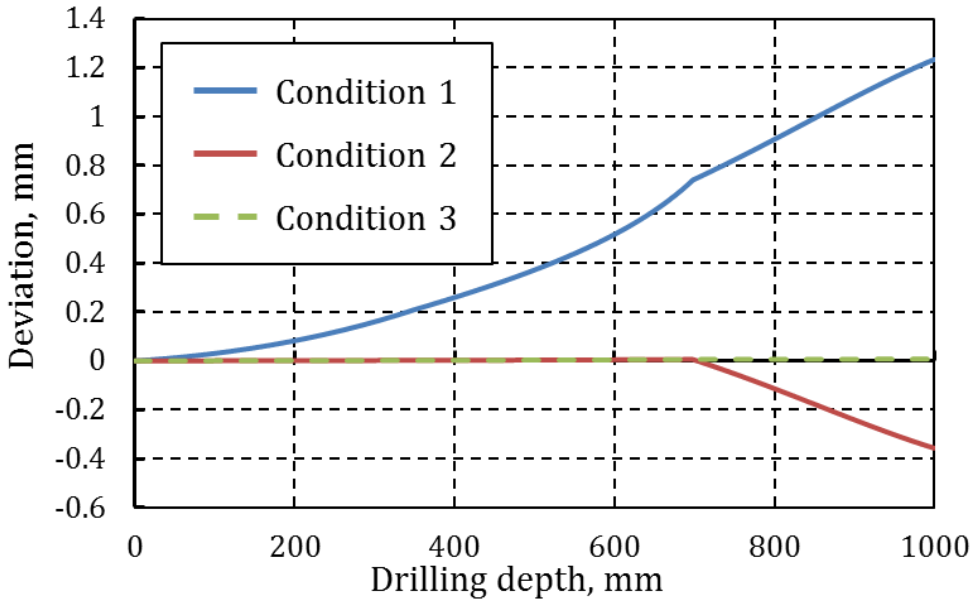

Figure 6.18 Effect of active misalignment control on the hole straightness deviation

A 1.5 m long drill is setup with support distances as 0.35 m, 0.76 m and 1.18 m for the first, second and the chip-box support respectively. The misalignments for Condition-1 are, $\delta_1 = -200\mu m$, $\delta_2 = -200\mu m$ and $\delta_3 = -200\mu m$. For Condition-2, misalignment at fixed support is changed to $\delta_3 = 200\mu m$. A notable difference can be seen in Figure 6.18 for the

predicted straightness deviation where the deviation is reduced form 1.2 mm for the Condition-1 to 0.4 mm in opposite direction for the Condition-2. The change in direction of deviation can be attributed to the change in tool tip inclination angle. The misalignment at second support becomes zero as the distance between the support and spindle is smaller when the first support reaches the second support The variation in direction of reaction forces depending the spindle location is shown in Figure 6.18 and Figure 6.19.

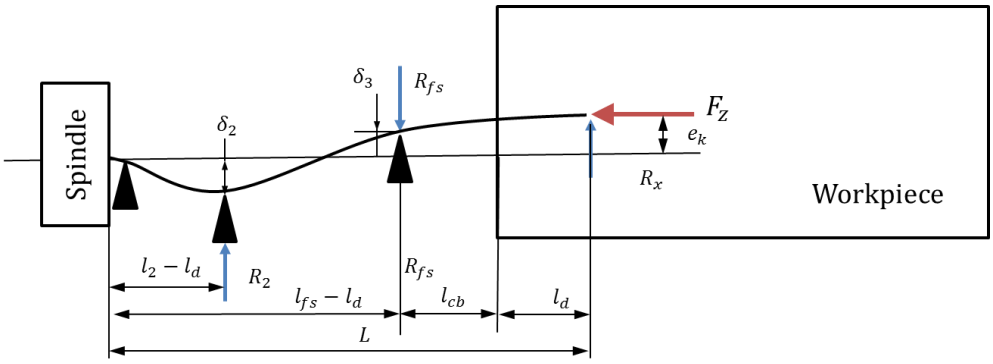

Figure 6.19 Reaction forces at second and fixed support when spindle reaches first support

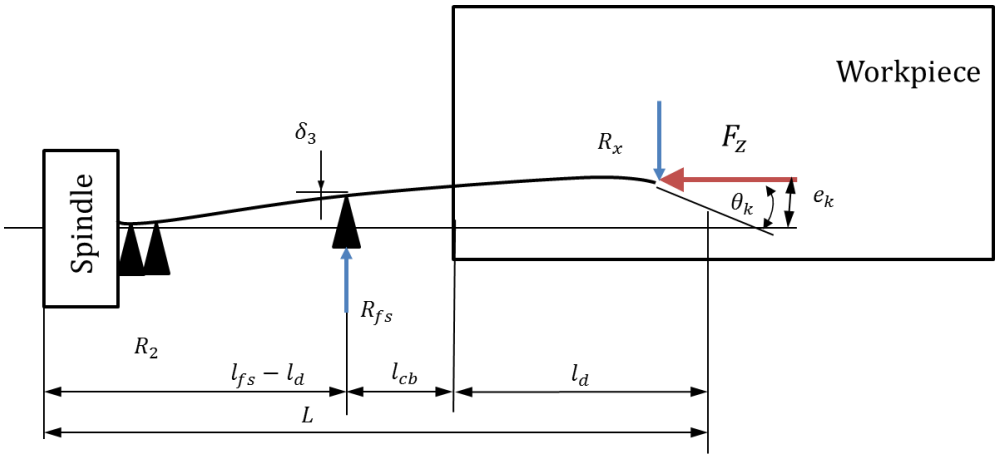

Figure 6.20 Reaction forces at fixed support and at drill tip when first support starts pushing second support

However, in practice, the effect is not sudden as it was predicted. This is due to the resistance by the hole wall which is not considered in this analysis.

Moreover, if δ_3 is adjusted to 0 when the first support reaches the second support as simulated in Condition-3, then the change in inclination can be avoided.

6.5 Experimental Validation

Two sets of experiments were conducted to check the robustness of predictive straightness deviation model and straightness control mechanism. The first set of experiments was used to validate the predictive straightness deviation model whereas the second set of experiments was carried out to substantiate the effectiveness of straightness control module.

6.5.1 Verification of the predictive model for straightness deviation

6.5.1.1 Machine and workpiece set-up

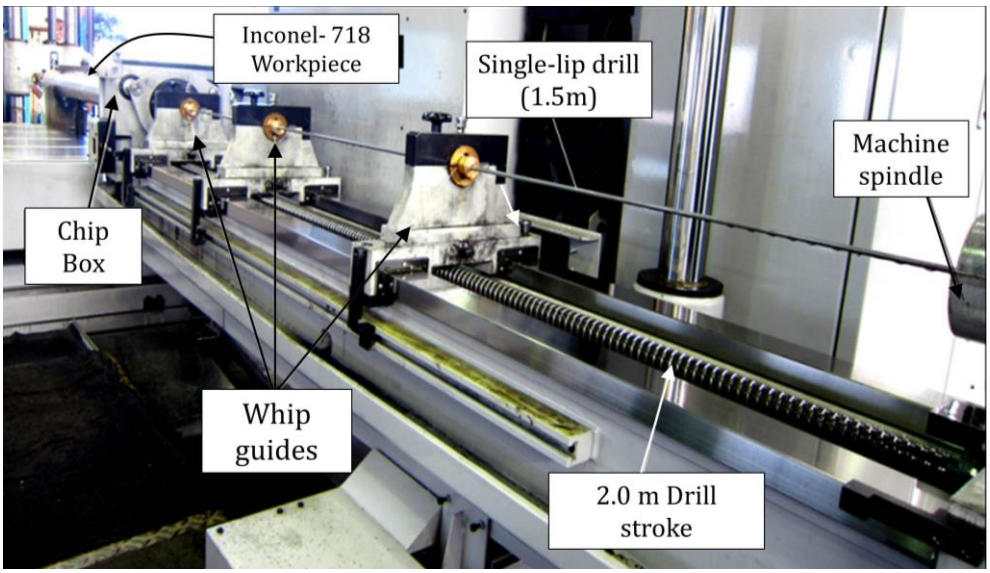

Figure 6.21 Machine set-up for the first set of deep hole drilling experiments

A cylindrical 1.8 m long age hardened Inconel-718 workpiece with diameter 150 mm was secured on the Miroku MHG-2000 J-NC column-type gundrilling machine bed with pair of heavy duty V-blocks and clamps as

shown in the Figure 6.21. The straightness along the length and flatness on the face of the workpiece was ensured using dial gauge micrometer with accuracy of 2 μm.

6.5.1.2 Drills and supports set-up

Table 6.1 Experimental parameters for the verifcation of the predictive straightness deviation model

	Hole 1	Hole 2
Drill length (L), m	1.5	1.5
l_1, m	0.35	0.35
l_2, m	0.76	0.76
l_{fs},m	1.18	1.18
δ_1, mm	-0.1	-0.1
δ_2, mm	-0.2	-0.2
δ_3, mm	-0.2	-0.35
l_{cb}, m	0.32	0.32
l_s, m	0.06	0.06
f, mm/min	8	8
RPM	800	800
Drill diameter, mm	8	8

Drills of 8 mm diameter were used for machining two 700 mm long blind holes with two intermediate supports and a support at chip-box entrance. The drill bush was selected based on the drill diameter to satisfy IT7 criteria. The drilling depth per cycle was kept 50 mm, after every cycle, the gundrills were reground. Total 28 cycles of drilling were conducted (14 cycles per hole). The other drilling parameters, misalignments, and support distances are summarized in Table 6.1. Emulsion fluids with 10-15% neat oil and extreme pressure additives were applied at 50-70 bar for cooling and lubrication. The chiller temperature for the coolant was kept at 27° C. The drilling thrust force was predicted by using the model developed in Chapter 4 and found to be 370N.

6.5.2 Straightness control experiments

6.5.2.1 Machine and workpiece set-up

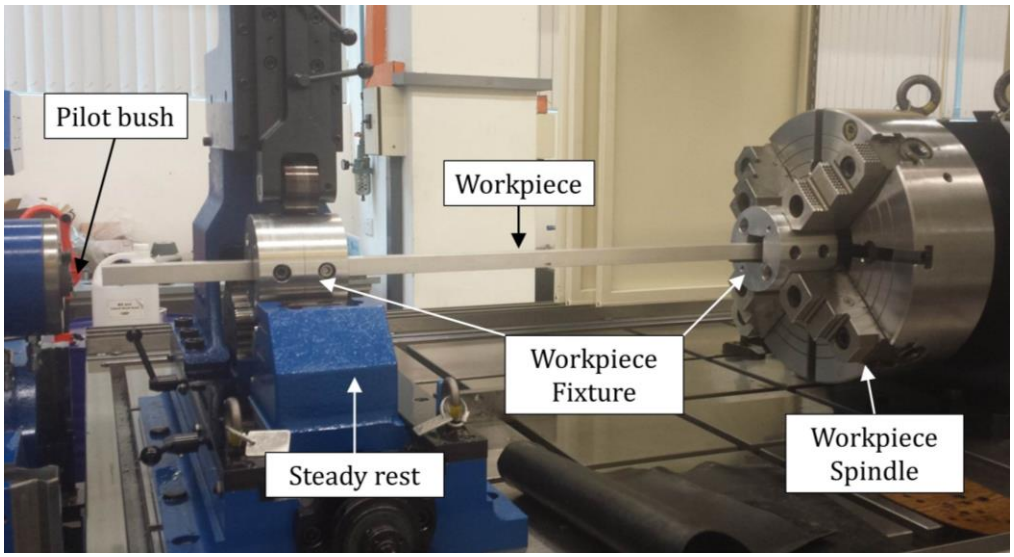

Figure 6.22 Machine set-up for straightness control experiments

One meter long square aluminium alloy 6061-T6 workpiece was secured using fixture and steady rest on the UNISIG deep hole drilling machine table as

shown in the Figure 6.22. The movable bearing housing was mounted near the fixed chip box support.

6.5.2.2 Drills and supports set-up

Table 6.2 Experimental parameters for the straightness control experiments

	Hole 3	Hole 4
Drill length (L), m	1.8	1.8
l_1, m	0.45	0.45
l_2, m	0.96	0.96
l_{fs},m	1.48	1.48
δ_1, mm	-0.1	-0.1
δ_2, mm	-0.2	-0.2
δ_3, mm	-0.2	0.2
l_{cb}, m	0.32	0.32
l_s, m	0.06	0.06
f, mm/min	8	8
RPM	800	800
Drill diameter, mm	8	8

A drill of 1.8 m length is used to machine two 700 mm long holes with support distance and misalignments as summarized in Table 6.2. The thrust

force was calculated using the predictive force model and found to be 270 N for the given feed rate. The straightness of hole was measured using ultrasonic thickness gauge at 50 mm interval along the drilling depth.

6.6 Results and Discussions

6.6.1 Results for Hole-1 and Hole-2

The predicted and experimental straightness deviation results for the Hole-1 and Hole-2 are shown in Figure 6.23. The hole deviation increase by 0.4 mm as the misalignment at the chip-box support increased by 150 μm. The predicted and experimental hole straightness results were found to be in good agreement.

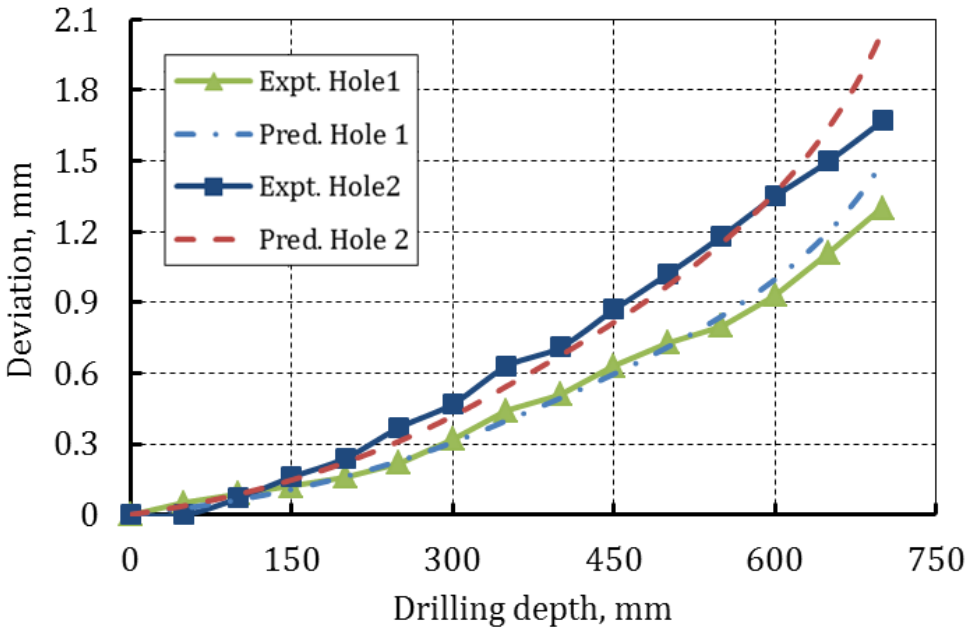

Figure 6.23 Predicted and experimental results for straightness deviation for Hole 1 and Hole 2

However, the model overpredicts the deviation as the distance between the second support and fix support decreases for drilling depth in the range of 600 mm to 700 mm. The decrease in distance between second and fixed support

increases the stiffness of the shaft leading to amplification of deviation. However, the experimental straightness deviation is gradual due the resistance by the hole wall.

6.6.2 Results for Hole-3 and Hole-4

The deviation in Hole-3 is predicted for the given parameters, which is in reasonable agreement with the experimental results as shown in Figure 6.24. The error in straightness prediction can be attributed to the hole wall deformation which is not considered in this analysis.

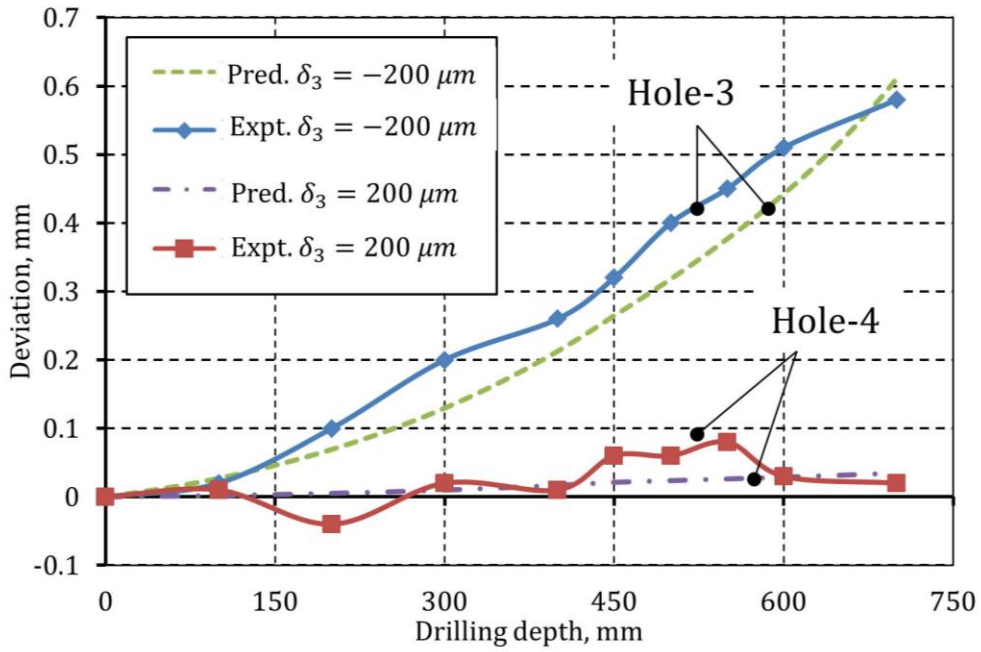

Figure 6.24 Straightness deviation for Hole 3 (without straightness control) and Hole 4 (with straightness control)

The misalignment required for the straight hole was determined using the predictive straightness deviation model. The misalignment at movable support was changed to $\delta = 200\ \mu m$. The experimental results follow the predicted deviation for Hole-4. The straightness deviation was reduced from 0.6 mm to 0.02 mm using the movable bearing housing module. The variation in the

experimental straightness deviation for Hole-4 was caused by the hole wall deformation as the alloy 6061 is softer as compared to the Inconel-718.

6.7 Concluding Remarks

In this chapter, a comprehensive predictive model for straightness deviation in deep hole drilling is developed which considers the effect of multiple support misalignments, the distance between supports and change in thrust force. It was found that –

- Fix support at chip-box has a greater influence on straightness deviation as compared to the misalignment at other supports.

- The distance between support nearer to the chip-box has more control on straightness deviation as compared to the other support distances. Moreover, unlike the conventional wisdom in deep hole drilling, it was found that the stiffer shafts with support misalignments amplify the straightness deviation.

- The straightness deviation increases as the thrust force increases. Depending on the unsupported length, the drill might buckle if the drilling parameters are selected improperly.

- The predicted results for hole straightness deviation reasonably match with the experimental results. However, the model needs to consider effects of hole wall deformation into account for better accuracy.

- A novel movable bearing housing set-up was developed and successfully used for the straightness control. The movable bearing

housing should be mounted at fixed chip-box support for effective straightness control.

Chapter 7: Conclusions and Future Works

This thesis work was motivated by the industry requirement of 1 mm per meter straightness deviation for deep hole drilling in high strength Inconel-718 to avoid expensive rework or scrapping of the material. Hence, a predictive approach for straightness deviation control was proposed and experimentally validated. The major findings of the work are summarized as follows.

7.1 Conclusions

7.1.1 Benchmarking of single-lip drill engagement

- A quantitative approach for evaluation of single-lip drill-workpiece engagement was proposed and experimentally validated for Inconel-718 in the beginning of the research. The benchmarking of the engagement provided the guidelines for diametrical tolerance and bottom hole geometry of the pilot hole. In the case of pilot bushes, guidelines were provided for selection of the tool geometry. As a result, the probability of the tool chipping during engagement was significantly reduced. Finally, a robust framework for smooth engagement was provided based on the geometrical model.

7.1.2 Predictive modelling of drilling forces

- A comprehensive predictive model for drilling forces was proposed based on the considerations of micro and macro geometry of the single-lip drill. The robustness of the model was validated for various drill geometries where the error between the predicted and the

experimental results was found to be less than 20%. Based on the force analysis, it was concluded that the uncut chip thickness to cutting edge radius ratio should be kept more than 1 to avoid excessive ploughing forces causing an increase in thrust force. The force model also predicted the distribution of radial and tangential forces on drill cutting edges which is required for bearing pad optimization and thin wall deformation studies.

7.1.3 Chip formation and chip breaking

- A detail classification of chip morphology in the single-lid drilling of Inconel-718 was provided based on a comprehensive experimental study. Moreover, chip formation mechanism for different chip morphologies was explained in detail. A novel experimental set-up with transparent tube and the high-speed camera was used to study elemental and snarled chip formation. It was observed that at lower feed rates the chip formation was dominated by up-curling due to ploughing phenomena.

- A details explanation for spiral chip formation was provided. It was observed that the chip breaking mechanism significantly differs for elemental, snarled chips and spiral chips. The elemental chips at lower feed rates were broken due to pressure exerted by coolant force however, the spiral chips were broken due to a combination of frictional force and coolant pressure.

- A quantification of the effect of chip morphology on the variation in thrust force was provided. A set of guidelines for tool geometry selection was provided to ensure smooth chip evacuation and stable drilling process based on the analysis.

7.1.4 Modelling of hole straightness deviation

- A comprehensive model for hole straightness deviation was proposed which considers multiple support misalignments and changing distances of the supports. The straightness model was experimentally validated for the accuracy and the error was found to be in the reasonable range.

- It was found that the misalignment on the support nearer to the tool tip has a greater influence on the straightness deviation as compared to the other support misalignments. Similarly, the support distance between the nearest support to the tool tip significantly affects the straightness deviation. As the length between supports decreases the effect of misalignment on straightness deviation is amplified due to increases in stiffness.

7.1.5 Straightness control

- Based on the analysis, a novel movable support assembly was proposed to actively control the straightness deviation. The use of movable support for straightness correction was successfully demonstrated.

- The objective of development of a robust predictive framework for the straightness control in deep hole drilling of Inconel-718 is successfully achieved.

7.2 Future works

7.2.1 Future experiments

The concept of active misalignment controlled was only tested on the Aluminum Alloy 6061 workpiece due to machine set-up constrains. In future, the same should be tested on the Inconel-718 workpiece.

7.2.2 Hole wall deformation

For thin walled high aspect ratio hole, it is important to consider the effect of hole wall deformation on straightness deviation. The stability of the self-piloting drill is mainly affected by the ability of the bearing pads to effectively balance the cutting edge forces. In future, the predictive force model can be used to predict burnishing depth and optimize the location of the bearing pads. It is also important to study the effect of burnishing on the surface integrity of the hole wall which is important for the applications in aerospace industry.

7.2.3 Novel chip breakers

Currently, the deep hole drilling process in Inconel-718 is being carried out at very low feed rates which significantly reduces the productivity. The major reason for using lower feed rates is to avoid chip clogging. The conventional chip breakers on the rake face are ineffective in the case of single-lip drilling of Inconel-718. Therefore, new designs for the chip breakers should be tested

for the effective chip breaking. One of the proposed design is shown in Figure 7.1

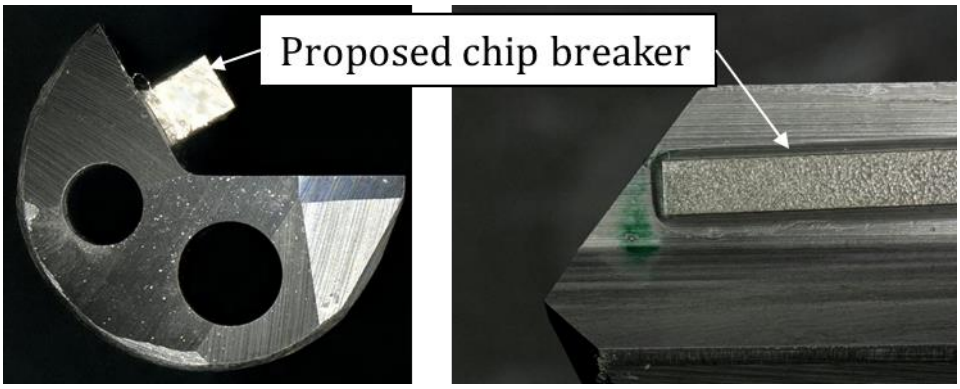

Figure 7.1 Proposed chip breaker design

7.2.4 Tool material

Currently, the carbide tip has very short tool life which requires frequent tool regrinding while drilling Inconel-718. Moreover, the cutting speed is limited to 20 m/min due to significant cobalt loss at the bearing pads. In future, harder cutting tool materials with lower cobalt percentage such as binderless cBN should be tested on Inconel-718 for its feasibility.

BIBLIOGRAPHY

1. Ulutan, D. and T. Ozel, *Machining induced surface integrity in titanium and nickel alloys: A review.* International Journal of Machine Tools and Manufacture, 2011. **51**(3): p. 250-280.

2. deBarbadillo, J.J. and S.K. Mannan, *Alloy 718 for Oilfield Applications.* Jom, 2012. **64**(2): p. 265-270.

3. EntrustManufacturingTechnologies. *UNISIG Deep hole drilling machines*. 2016; Available from: http://entrustmt.com/products/deep-hole-drilling-machines/.

4. Joshi, S.S. and S.N. Melkote, *An Explanation for the Size-Effect in Machining Using Strain Gradient Plasticity.* Journal of Manufacturing Science and Engineering, 2004. **126**(4): p. 679.

5. Astakhov, V.P., *Geometry of Single-point Turning Tools and Drills*. Springer Series in Advanced Manufacturing. 2010: Springer.

6. Sakuma, K., et al., *Self-Guiding Action of Deep-Hole-Drilling Tools.* Annals of the ClRP, 1981. **30**(1): p. 311-315.

7. Griffiths, B.J., *Modelling Complex Force Systems, Part 1: The Cutting and Pad Forces in Deep Drilling.* Journal of Engineering for Industry, 1993. **115**(2): p. 169-176.

8. Griffiths, B.J. and R.J. Grieve, *Modelling Complex Force Systems, Part 2: A Decomposition of the Pad Forces in Deep Drilling.* Journal of Engineering for Industry, 1993. **115**(2): p. 177-183.

9. Astakhov, V.P. and M.O.M. Osman, *An analytical evaluation of the cutting forces in self-piloting drilling using the model of shear zone with parallel boundaries. Part 1: Theory.* International Journal of Machine Tools and Manufacture, 1996. **36**(11): p. 1187-1200.

10. Astakhov, V.P. and M.O.M. Osman, *An analytical evaluation of the cutting forces in self-piloting drilling using the model of shear zone with parallel boundaries. Part 2: Application.* International Journal of Machine Tools and Manufacture, 1996. **36**(12): p. 1335-1345.

11. Jung, J. and F. Ke, *A gundrilling force system.* International Journal of Machine Tools and Manufacture, 2007. **47**(7–8): p. 1276-1284.

12. Chandrasekharan, V., S.G. Kapoor, and R.E. DeVor, *A Mechanistic Model to Predict the Cutting Force System for Arbitrary Drill Point Geometry.* Journal of Manufacturing Science and Engineering, 1998. **120**(3): p. 563-570.

13. Wang, Y., W. Jia, and J. Zhang, *The force system and performance of the welding carbide gun drill to cut AISI 1045 steel.* The International Journal of Advanced Manufacturing Technology, 2014. **74**(9-12): p. 1431-1443.

14. GuhringInc. *Deep Hole Drills Catalogue*. 2016; Available from: www.guhring.com.

15. SterlingInc. *Sterling Gun Drills Literature*. 2016; Available from: www.sterlinggundrills.com.

16. StarCutterCompany. *Gundrill Product Flyers*. 2013; Available from: www.starcutter.com.

17. Chin, J.-H., J.-S. Wu, and R.-S. Young, *The Computer Simulation and Experimental Analysis of Chip Monitoring for Deep Hole Drilling.* Journal of Engineering for Industry, 1993. **115**(2): p. 184.

18. Astakhov, V.P., V.V. Galitsky, and M.O.M. Osman, *A Novel Approach to the Design of Self-Piloting Drills With External Chip Removal, Part 1: Geometry of the Cutting Tip and Grinding Process.* Journal of Engineering for Industry, 1995. **117**(4): p. 453.

19. Mellinger, J.C., et al., *Modeling Chip-Evacuation Forces and Prediction of Chip-Clogging in Drilling.* Journal of Manufacturing Science and Engineering, 2002. **124**(3): p. 605.

20. Mellinger, J.C., et al., *Modeling Chip-Evacuation Forces in Drilling for Various Flute Geometries.* Journal of Manufacturing Science and Engineering, 2003. **125**(3): p. 405.

21. Potthast, C., et al., *Piezoelectric actuator design for ultrasonically assisted deep hole drilling.* Journal of Electroceramics, 2007. **20**(3-4): p. 187-192.

22. Heisel, U., et al., *Ultrasonic deep hole drilling in electrolytic copper ECu 57.* CIRP Annals - Manufacturing Technology, 2008. **57**(1): p. 53-56.

23. Wang, Y., et al., *The study on the chip formation and wear behavior for drilling forged steel S48CS1V with TiAlN-coated gun drill.* International Journal of Refractory Metals and Hard Materials, 2012. **30**(1): p. 200-207.

24. Biermann, D., M. Kirschner, and D. Eberhardt, *A novel method for chip formation analyses in deep hole drilling with small diameters.* Production Engineering, 2014. **8**(4): p. 491-497.

25. Klocke, F., G. Keitzel, and D. Veselovac, *Innovative Sensor Concept for Chip Transport Monitoring of Gun Drilling Processes.* Procedia CIRP, 2014. **14**: p. 460-465.

26. Katasuki, A., et al., *The influence of tool geometry on axial hole deviation in deep drilling: comparison of single- and multi-edge tools.* JSME International Journal, 1987. **30**: p. 1167–1174.

27. Katsuki, A., et al., *The influence of workpiece geometry on axial hole deviation in deep-hole drilling.* JSME International Journal, 1992. **35**: p. 160–167.

28. Astakhov, V.P., *The mechanisms of bell mouth formation in gundrilling when the drill rotates and the workpiece is stationary. Part I: the first stage of drill entrance.* International Journal of Machine Tools and Manufacture, 2002. **42**(10): p. 1135-1144.

29. Astakhov, V.P., *The mechanisms of bell mouth formation in gundrilling when the drill rotates and the workpiece is stationary. Part 2: the second stage of drill entrance.* International Journal of Machine Tools and Manufacture, 2002. **42**(10): p. 1145-1152.

30. Al-Ata, M. and M.T. Hayajneh, *An investigation of bell mouthing in precision hole machining with self-piloting tools.* The International Journal of Advanced Manufacturing Technology, 2008. **43**(1-2): p. 22-32.

31. Deng, C.-S., J.-C. Huang, and J.-H. Chin, *Effects of support misalignments in deep-hole drill shafts on hole straightness.* International Journal of Machine Tools and Manufacture, 2001. **41**(8): p. 1165-1188.

32. Chin, J.-H. and S.-D. Sheu, *Strengths and weaknesses of finite element modeling deep hole drilling as compared with beam and column equations.* The International Journal of Advanced Manufacturing Technology, 2006. **32**(3-4): p. 229-237.

33. Dudzinski, D., et al., *A review of developments towards dry and high speed machining of Inconel 718 alloy.* International Journal of Machine Tools and Manufacture, 2004. **44**(4): p. 439-456.

34. Rahman, M., W.K.H. Seah, and T.T. Teo, *The machinability of inconel 718.* Journal of Materials Processing Technology, 1997. **63**(1–3): p. 199-204.

35. Ezugwu, E.O. and S.H. Tang, *Surface abuse when machining cast iron (G-17) and nickel-base superalloy (Inconel 718) with ceramic tools.* Journal of Materials Processing Technology, 1995. **55**(2): p. 63-69.

36. Chen, Y.C. and Y.S. Liao, *Study on wear mechanisms in drilling of Inconel 718 superalloy.* Journal of Materials Processing Technology, 2003. **140**(1–3): p. 269-273.

37. Liao, Y.S., Y.C. Chen, and H.M. Lin, *Feasibility study of the ultrasonic vibration assisted drilling of Inconel superalloy.*

International Journal of Machine Tools and Manufacture, 2007. **47**(12–13): p. 1988-1996.

38. Sharman, A.R.C., A. Amarasinghe, and K. Ridgway, *Tool life and surface integrity aspects when drilling and hole making in Inconel 718.* Journal of Materials Processing Technology, 2008. **200**(1–3): p. 424-432.

39. Woon, K.S., S. Wan, and G.L. Tnay, *An Experimental and Simulation Study on Deep Hole Gundrilling of Inconel-718*, in *Proceedings of the 13th euspen International Conference*. 2013, euspen: Berlin. p. 277-280.

40. Woon, K.S., S. Kanno, and K. Liu, *The influence of drill geometric accuracy on steady tool wear development and catastrophic tool failure in high aspect ratio gundrilling of Inconel-718* Int. J. Abrasive Technology, 2013. **6**(1).

41. Imran, M., et al., *Comparison of tool wear mechanisms and surface integrity for dry and wet micro-drilling of nickel-base superalloys.* International Journal of Machine Tools and Manufacture, 2014. **76**(0): p. 49-60.

42. Bissacco, G., H.N. Hansen, and J. Slunsky, *Modelling the cutting edge radius size effect for force prediction in micro milling.* CIRP Annals - Manufacturing Technology, 2008. **57**(1): p. 113-116.

43. Johnson, G. and W.H. Cook. *A constitutive model and data for metals subjected to large strains, high strain rates and high temperatures*. in *Proceedings of the 7th International Symposium on Ballistics*. 1983.

44. Pereira, J.M. and B.A. Lerch, *Effects of heat treatment on the ballistic impact properties of Inconel 718 for jet engine fan containment applications.* International Journal of Impact Engineering, 2001. **25**(8): p. 715-733.

45. Uhlmann, E., M.G. von der Schulenburg, and R. Zettier, *Finite Element Modeling and Cutting Simulation of Inconel 718.* CIRP Annals - Manufacturing Technology, 2007. **56**(1): p. 61-64.

46. Mitrofanov, A.V., V.I. Babitsky, and V.V. Silberschmidt, *Thermomechanical finite element simulations of ultrasonically assisted turning.* Computational Materials Science, 2005. **32**(3-4): p. 463-471.

47. Lorentzon, J., N. Järvstråt, and B.L. Josefson, *Modelling chip formation of alloy 718.* Journal of Materials Processing Technology, 2009. **209**(10): p. 4645-4653.

48. Pottlacher, G., et al., *Thermophysical properties of solid and liquidInconel 718 Alloy**. Scandinavian Journal of Metallurgy, 2002. **31**(3): p. 161-168.

49. Basak, D., R.A. Overfelt, and D. Wang, *Measurement of Specific Heat Capacity and Electrical Resistivity of Industrial Alloys Using Pulse Heating Techniques.* International Journal of Thermophysics, 2003. **24**(6): p. 1721-1733.

50. Lee, S.H., S.W. Kim, and K.H. Kang, *Effect of Heat Treatment on the Specific Heat Capacity of Nickel-Based Alloys.* International Journal of Thermophysics, 2006. **27**(1): p. 282-292.

51. P.L.B., O., *The mechanics of machining : an analytical approach to assessing machinability*. Ellis Horwood series in mechanical engineering. 1989.

52. Adibi-Sedeh, A.H., V. Madhavan, and B. Bahr, *Extension of Oxley's Analysis of Machining to Use Different Material Models.* Journal of Manufacturing Science and Engineering, 2003. **125**(4): p. 656.

53. Lalwani, D.I., N.K. Mehta, and P.K. Jain, *Extension of Oxley's predictive machining theory for Johnson and Cook flow stress model.* Journal of Materials Processing Technology, 2009. **209**(12-13): p. 5305-5312.

54. Boothroyd, G., *Fundamentals of Metal Machining and Machine Tools, Third Edition*. 1988: Taylor & Francis.

55. Waldorf, D.J., R.E. DeVor, and S.G. Kapoor, *A Slip-Line Field for Ploughing During Orthogonal Cutting.* Journal of Manufacturing Science and Engineering, 1998. **120**(4): p. 693.

56. Zemzemi, F., et al., *Identification of friction and heat partition model at the tool-chip-workpiece interfaces in dry cutting of an inconel 718 alloy with cbn and coated carbide tools.* Advances in Manufacturing Science and Technology, 2014. **38**(1).

57. Biermann, D. and I. Iovkov, *Investigations on the formation of straightness deviation in MQL deep-hole drilling of thin-walled aluminium components.* Production Engineering, 2015. **9**(4): p. 527-535.

58. Biermann, D. and M. Kirschner, *Experimental investigations on single-lip deep hole drilling of superalloy Inconel 718 with small diameters.* Journal of Manufacturing Processes, 2015. **20**: p. 332-339.

59. Jawahir, I.S., *Chip-forms, Chip Breakability and Chip Control*, in *CIRP Encyclopedia of Production Engineering*. 2014. p. 178-194.

60. Kharkevich, A.G. and P.K. Venuvinod, *Extension of basic geometric analysis of 3-D chip forms in metal cutting to chips with obstacle-induced deformation.* International Journal of Machine Tools and Manufacture, 2002. **42**(2): p. 201-213.

61. Pawade, R.S. and S.S. Joshi, *Mechanism of Chip Formation in High-Speed Turning of Inconel 718.* Machining Science and Technology, 2011. **15**(1): p. 132-152.

62. Nakayama, K., M. Uenoyama, and K. Tamura, *Chip Curl in Metal-Cutting Process.* Journal of the Japan Society of Precision Engineering, 1961. **27**(321): p. 681-688.

63. Ke, F., J. Ni, and D.A. Stephenson, *Continuous chip formation in drilling.* International Journal of Machine Tools and Manufacture, 2005. **45**(15): p. 1652-1658.

64. Singh, D.K., *Strength of Materials*. Third ed. 2014: CRC Press.

LIST OF PUBLICATIONS

Journal Publications:

Akshay Chaudhari, Malarvizhi S., Keng Soon Woon, A. Senthil Kumar, Mustafizur Rahman (2015); The effects of pilot hole geometry on tool-work engagement efficacy in deep hole drilling, Journal of Manufacturing Processes, Volume 19, pp. 135–141.

K.S. Woon, A. Chaudhari, M. Rahman, S. Wan, A. Senthil Kumar (2014); The effects of tool edge radius on drill deflection and hole misalignment in deep hole drilling of Inconel-718; CIRP Annals-Manufacturing Technology, Vol.64:1, pp.125-128.

Conference Publications:

Malarvizhi S., A. Chaudhari, Keng Soon Woon, A. Senthil Kumar, Mustafizur Rahman (2016); Influence of Burnishing Axial Interference on Hole Surface Quality in Deep Hole Drilling of Inconel 718; 44th North American Manufacturing Research Conference, June 27-July 1, 2016, Blacksburg, Virginia, United States.

K.S. Woon, A. Chaudhari, M. Rahman, A. Senthil Kumar (2016); Deep hole drilling methodology for high yield strength Inconel 718 >1000 MPa, euspen 16th International Conference & Exhibition 2016, Nottingham UK.

K.S. Woon, A. Chaudhari, A. Senthil Kumar, M. Rahman (2014); The Effects of Tool Degradation on Hole Straightness in Deep Hole Drilling of Inconel-718; 6th CIRP International Conference on High Performance Cutting, Berkeley.

A. Chaudhari, K.S. Woon, A. Senthil Kumar, M. Rahman (2013), Tool wear and chip morphologies in gundrilling of Inconel 718, International conference on Processing and Fabrication of Advanced Materials XXII, Singapore (PFAM XXII 2013).